

MODELLING AND NOISE ANALYSIS OF CLOSED-LOOP CAPACITIVE
SIGMA-DELTA MEMS ACCELEROMETER

A THESIS SUBMITTED TO
THE GRADUATE SCHOOL OF NATURAL AND APPLIED SCIENCES
OF
MIDDLE EAST TECHNICAL UNIVERSITY

BY

BÍTER BOĞA

IN PARTIAL FULFILLMENT OF THE REQUIREMENTS
FOR
THE DEGREE OF MASTER OF SCIENCE
IN
ELECTRICAL AND ELECTRONICS ENGINEERING

JULY 2009

Approval of the thesis:

**MODELLING AND NOISE ANALYSIS OF CLOSED-LOOP CAPACITIVE
SIGMA-DELTA MEMS ACCELEROMETER**

submitted by **BİTER BOĞA** in partial fulfillment of the requirements for the degree of **Master of Science in Electrical and Electronics Engineering Department, Middle East Technical University** by,

Prof. Dr. Canan Özgen
Dean, Graduate School of **Natural and Applied Sciences** _____

Prof. Dr. İsmet Erkmén
Head of Department, **Electrical and Electronics Engineering** _____

Assoc. Prof. Dr. Haluk Kùlah
Supervisor, **Electrical and Electronics Eng. Dept., METU** _____

Examining Committee Members:

Prof. Dr. Tayfun Akın
Electrical and Electronics Engineering Dept., METU _____

Assoc. Prof. Dr. Haluk Kùlah
Electrical and Electronics Engineering Dept., METU _____

Dr. Barış Bayram
Electrical and Electronics Engineering Dept., METU _____

Dr. Said Emre Alper
METU-MEMS Research and Application Center _____

Dr. A. Pınar Koyaz
Guidance, Control, and Navigation Group, TÜBİTAK-SAGE _____

Date:

July 8, 2009

I hereby declare that all information in this document has been obtained and presented in accordance with academic rules and ethical conduct. I also declare that, as required by these rules and conduct, I have fully cited and referenced all material and results that are not original to this work.

Name, Last Name : Biter BOŽA

Signature :

ABSTRACT

MODELLING AND NOISE ANALYSIS OF CLOSED-LOOP CAPACITIVE SIGMA-DELTA MEMS ACCELEROMETER

Boğa, Biter

M.S., Department of Electrical and Electronics Engineering

Supervisor : Assoc. Prof. Dr. Haluk Kùlah

July 2009, 113 pages

This thesis presents a detailed SIMULINK model for a conventional capacitive Σ - Δ accelerometer system consisting of a MEMS accelerometer, closed-loop readout electronics, and signal processing units (e.g. decimation filters). By using this model, it is possible to estimate the performance of the full accelerometer system including individual noise components, operation range, open loop sensitivity, scale factor, etc. The developed model has been verified through test results using a capacitive MEMS accelerometer, full-custom designed readout electronics, and signal processing unit implemented on a FPGA.

Conventional accelerometer system with force-feedback is used in this thesis. The sensor is a typical capacitive lateral accelerometer. The readout electronics form a 2nd order electromechanical Σ - Δ modulator together with the accelerometer, and provide a single-bit PDM output, which is decimated and filtered with a signal processing unit, software implemented on a FPGA. The whole system is modeled in MATLAB-SIMULINK since it has both mechanical and electrical parts.

To verify the model, two accelerometer systems are implemented. Each accelerometer system is composed of a MEMS accelerometer, readout circuit, and decimation filters. These two different designs are implemented and simulation and test results are compared in terms of output noise, operational range, open loop sensitivity, and scale factor. The first design operates at 500 kHz sampling rate and has 0.48 V/g open-loop sensitivity, 58.7 $\mu\text{g}/\sqrt{\text{Hz}}$ resolution, $\pm 12\text{g}$ operation range, and $0.97 \cdot 10^{-6}$ g/(output units) scale factor, where these numbers are in close agreement with the estimated results found with simulations. Similarly, the second design operates at 500 kHz sampling rate and has 0.45 V/g open-loop sensitivity, 373.3 $\mu\text{g}/\sqrt{\text{Hz}}$ resolution, $\pm 31\text{g}$ operation range, and $2.933 \cdot 10^{-6}$ g/(output units) scale factor, where these numbers are also close to the estimated results found with simulations.

Within this thesis study, an accelerometer sensing element design algorithm is also proposed which is based on the theoretical background obtained in accelerometer system SIMULINK model. This algorithm takes the requirements of the desired accelerometer as input and outputs the dimensions of the minimum noise accelerometer satisfying these requirements. The algorithm is extended to design three different accelerometer structures. An accelerometer sensing element is designed using the proposed design algorithm and tested in order to see performance matching of the algorithm. The designed accelerometer has $\pm 33.02\text{g}$ operational range and $155\mu\text{g}/\sqrt{\text{Hz}}$ noise where these numbers matches with the values found by the algorithm.

Keywords: MEMS accelerometer, capacitive accelerometer modeling, closed-loop accelerometer, accelerometer noise analysis, accelerometer testing.

ÖZ

KAPASİTİF SİGMA-DELTA YAPILI MEMS İVMEÖLÇER MODELLEMESİ VE GÜRÜLTÜ ANALİZİ

Boğa, Biter

Yüksek Lisans, Elektrik ve Elektronik Mühendisliği Bölümü

Tez Yöneticisi : Doç. Dr. Haluk Külâh

Temmuz 2009, 113 sayfa

Bu tezde MEMS ivmeölçer duyargası, kapalı döngü okuma devresi ve sinyal işleme birimlerinden oluşan geleneksel kapasitif Σ - Δ yapılı ivmeölçer sisteminin SIMULINK ortamında geliştirilen detaylı modeli anlatılmaktadır. Bu model ile ivmeölçer sisteminin gürültüsü, çalışma aralığı, açık döngü hassasiyeti ve orantı katsayısı gibi performans parametreleri tahmin edilebilmektedir. Sığasal MEMS ivmeölçer, özel tasarım okuma devresi ve FPGA üzerinde oluşturulan sinyal işleme birimleri gerçekleştirilerek ivmeölçerin sistem seviyesinde bütünlenmesi yapılmıştır ve test edilmiştir. Test sonuçları, geliştirilen modelin doğruluğunu ispatlamak için kullanılmıştır.

Bu tez çalışmasında geleneksel kapalı döngü ivmeölçer kullanılmıştır. İvmeölçer duyargası tipik kapasitif yapılı ivmeölçerdir. Okuma devresi; ivmeölçer duyargası ile 2. dereceden elektromekanik Σ - Δ yapısını oluşturmaktadır ve darbe sıklığı module edilmiş yüksek frekanslı 1-bit çıktı oluşturmaktadır. Okuma devresi çıkışı FPGA üzerinde oluşturulan desimasyon filtresi ile filtrelenerek ivmeölçer çıktısını oluşturmaktadır. İvmeölçer sistemi hem mekanik hem de elektriksel kısımlar içerdiği için MATLAB-SIMULINK ortamında modellenmiştir.

Geliştirilen modelin doğruluğunu ispatlamak amacıyla iki ivmeölçer sistemi oluşturulmuştur. Her iki ivmeölçer sistemi de ivmeölçer duyargası, okuma devresi ve desimasyon filtresinden oluşmaktadır. Bu iki ivmeölçer sisteminin simülasyonları ve testleri yapılarak; gürültü, çalışma aralığı, açık döngü hassasiyeti ve orantı katsayısı gibi parametreleri açısından karşılaştırılmıştır. Birinci ivmeölçer sistemi 500 kHz örnekleme frekansında çalışmaktadır ve 0.48 V/g açık döngü hassasiyeti, 58.7 $\mu\text{g}/\sqrt{\text{Hz}}$ çözünürlük, $\pm 12\text{g}$ çalışma aralığı ve $0.97 \cdot 10^{-6}$ g/(çıkı birimi) orantı katsayısına sahiptir. Aynı şekilde ikinci ivmeölçer de 500 kHz örnekleme frekansında çalışmaktadır ve 0.45 V/g açık döngü hassasiyeti, 373.3 $\mu\text{g}/\sqrt{\text{Hz}}$ çözünürlük, $\pm 31\text{g}$ çalışma aralığı ve $2.933 \cdot 10^{-6}$ g/(çıkı birimi) orantı katsayısına sahiptir. Birinci ve ikinci ivmeölçer için bulunan bu değerler, simülasyon ile bulunan değerlere oldukça yakındır.

Bu tez çalışması kapsamında, ivmeölçer modellemesinde elde edilen teorik altyapı kullanılarak ivmeölçer duyargası tasarlayan bir algoritma geliştirilmiştir. Bu algoritma istenilen ivmeölçer parametrelerini alarak bu parametreleri sağlayan en düşük gürültülü ivmeölçer duyargasının boyutlarını çıktı olarak vermektedir. Bu algoritma üç farklı ivmeölçer duyargası yapısı için geliştirilmiştir. Algoritmanın doğru çalıştığını görmek amacıyla algoritma kullanılarak bir ivmeölçer duyargası tasarlanmıştır ve testleri yapılmıştır. Tasarlanan ivmeölçerlerin çalışma aralığının $\pm 33.02\text{g}$ ve gürültü değerinin $155\mu\text{g}/\sqrt{\text{Hz}}$ olduğu ve bu değerlerin algoritma ile bulunan değerlere yakın olduğu görülmüştür.

Anahtar Kelimeler: MEMS ivmeölçer, kapasitif ivmeölçer modellemesi, kapalı-döngü ivmeölçer, ivmeölçer gürültü analizi, ivmeölçer testleri.

To my family...

ACKNOWLEDGMENTS

Firstly, I would like to express my sincere gratitude and thanks to my supervisor Assoc. Prof. Dr. Haluk Klah for his support, friendly attitude, guidance and encouragement at each stage of this thesis study.

I would like to thank to TBİTAK-SAGE (*The Scientific and Technological Research Council of Turkey – Defense Industries Research and Development Institute*) for the support given throughout this study. I would like to present my appreciation to Dr. A. Pınar Koyaz and A. Galip Yıldırım for their support and guidance during my studies.

I would like to thank to TBİTAK 105A015 Project personnel for their support given during my studies.

I would like to present my thanks to İlker Ender Ocak and Reha Kepenek for their support, sharing their knowledge, and their help in implementation, packaging and testing of the accelerometer system.

I would also like to express my special thanks to Faruk İnaltekin for his help, encouragement, and friendship.

I would like to thank to TBİTAK for their scholarship.

Lastly, my sincerely thanks go to my parents, Adem Boęa and Fatma Boęa, my brothers Ercan and Mikdat, and my sisters Bıhadar, Selvi, and Esen for their support and unlimited love.

TABLE OF CONTENTS

ABSTRACT	IV
ÖZ.....	VI
ACKNOWLEDGMENTS	IX
TABLE OF CONTENTS.....	X
LIST OF TABLES.....	XIV
LIST OF FIGURES.....	XVI
CHAPTER 1	1
INTRODUCTION	1
1.1 Accelerometer Performance Parameters	2
1.2 Accelerometer Types.....	5
1.3 Previous Studies	8
1.4 Objectives and Organization of the Thesis.....	12
CHAPTER 2	14
CAPACITIVE MEMS ACCELEROMETER SYSTEM THEORY.....	14

2.1	Sensing Element: Capacitive Accelerometers	14
2.2	Capacitive Interface Electronic	17
2.2.1	Sigma-Delta Modulator	17
2.3	Signal Processing Units	21
2.4	Noise Sources of a Capacitive Sigma-Delta MEMS Accelerometer	25
2.4.1	Mechanical Noise	25
2.4.2	Electrical Noise	26
CHAPTER 3	30
CAPACITIVE SIGMA-DELTA MEMS ACCELEROMETER SYSTEM MATLAB-SIMULINK MODEL.....	30
3.1	Capacitive MEMS Accelerometer Model.....	31
3.1.1	Accelerometer Transfer Function.....	31
3.1.2	Accelerometer Displacement to Capacitance Change Block.....	39
3.2	Sigma-Delta Readout Circuit Model	40
3.3	Decimation Filter Model	44
3.4	Modeling the Noise Sources	46
3.5	Capacitive Sigma-Delta MEMS Accelerometer System Model and Designed User Interface.....	49
CHAPTER 4	53
ACCELEROMETER SYSTEM SIMULATION AND TEST RESULTS.....	53

4.1	Implemented Accelerometer Systems.....	53
4.1.1	Fabricated MEMS Accelerometers	54
4.1.2	Implemented Readout Electronics	58
4.1.3	Implemented Decimation Filter	60
4.2	Accelerometer Systems Simulation and Test Results	61
4.2.1	12-Position Acceleration	63
4.2.2	Clock Frequency Effect on the Output Noise	69
4.2.3	Decimation Order Effect on the Output Noise.....	73
4.2.4	Integration Capacitance Effect on the Output Noise.....	78
4.2.5	Operational Range	80
4.2.6	Conclusion	84
CHAPTER 5	87
	ACCELEROMETER SENSING ELEMENT DESIGN ALGORITHM.....	87
5.1	Overview of the Accelerometer Design Algorithm.....	87
5.2	1st Accelerometer Structure Design Algorithm	91
5.2.1	1 st Accelerometer Structure	91
5.2.2	Design Parameters and Constraints for the 1 st Structure	92
5.3	2nd Accelerometer Structure Design Algorithm	94
5.3.1	2 nd Accelerometer Structure.....	94
5.3.2	Design Parameters and Constraints for the 2 nd Structure	95
5.4	3rd Accelerometer Structure Design Algorithm	96
5.4.1	3 rd Accelerometer Structure	96
5.4.2	Design Parameters and Constraints for the 3 rd Structure.....	97
5.5	Accelerometer Design Algorithm Performance Matching	99

CHAPTER 6	103
CONCLUSION AND FUTURE WORK	103
6.1 Future Directions	105
REFERENCES	107

LIST OF TABLES

Table 1: Application areas of accelerometers depending on bandwidth, resolution, and operational range	2
Table 2: Capacitive accelerometer system noise sources	47
Table 3: DWP-1 accelerometer dimensions.....	56
Table 4: DWP-2 accelerometer dimensions.....	57
Table 5: Accelerometer system parameters used in model for simulations of DWP-1	62
Table 6: Accelerometer system parameters used in model for simulations of DWP-2	62
Table 7: Effect of clock frequency on DWP-1 accelerometer output noise	71
Table 8: Effect of clock frequency on DWP-2 accelerometer output noise	72
Table 9: Effect of decimation order on DWP-1 accelerometer output noise and comparison of scale factor values of simulation and test results	75
Table 10: DWP-2 accelerometer output noise and scale factor values of simulation and test results at 500kHz clock frequency.....	77
Table 11: DWP-2 accelerometer output noise and scale factor values of simulation and test results at 1MHz clock frequency	77
Table 12: Comparison of simulation and test results of DWP-1 accelerometer	85

Table 13: Comparison of simulation and test results of DWP-2 accelerometer	85
Table 14. Constraints used to design 1 st accelerometer structure	93
Table 15. Constraints used to design 2 nd accelerometer structure	96
Table 16: Constraints used to design 2 nd accelerometer structure	98
Table 17: Designed accelerometer dimensions and performance parameters	100

LIST OF FIGURES

Figure 1: SPICE model of a silicon micromachined accelerometer with control electronics, Berkeley Sensors and Actuators Center and Nonlinear Systems Design Group [17].	8
Figure 2: Simulink model of a force-balanced MEMS accelerometer implemented by Harbin Institute of Technology, China [18].	9
Figure 3: Simulink block diagram of a force-balanced capacitive accelerometer implemented by I.I.T. Roorkee, India [19].	10
Figure 4: Matlab/Simulink model of an analogue capacitive micro-accelerometer generated by University of Craiova, Romania [20].	11
Figure 5: General structure of capacitive MEMS accelerometers.	15
Figure 6: Illustration of capacitive MEMS accelerometer dimensions.	15
Figure 7: Capacitance change depending on the applied acceleration.	16
Figure 8: Block diagram of an electromechanical Sigma-Delta modulator [25].	18
Figure 9: (a) Nyquist converter quantization noise spectrum, (b) oversampled converter quantization noise [27].	19
Figure 10: Linearized model of first order sigma delta modulator.	20
Figure 11: Oversampled first order sigma-delta quantization noise spectrum.	21
Figure 12: Structure of a Sinc^M filter.	22

Figure 13: Addition block of Sinc filter.....	23
Figure 14: Subtraction block of Sinc filter.....	23
Figure 15: First-order Sinc filter response [30].....	24
Figure 16: Block diagram of the full accelerometer [32].....	30
Figure 17: Mass-spring-damper system.....	31
Figure 18: Illustration of capacitive MEMS accelerometer dimensions.	33
Figure 19: Couette flow between proof mass and substrate and top plate.....	35
Figure 20: Illustration of squeeze film damping between the fingers.	36
Figure 21: Relation between the factor ‘c’ and ‘ h/L_{fin} ’.	36
Figure 22: Folded beam spring illustration.	37
Figure 23: Capacitive MEMS accelerometer Matlab-Simulink model.	40
Figure 24: Electromechanical sigma-delta readout circuit [35].	41
Figure 25: Structure of the readout circuit [35].....	41
Figure 26: Electromechanical sigma-delta readout Matlab-Simulink model.	44
Figure 27: Sinc ³ filter model.	45
Figure 28: Sinc ² filter model.	45
Figure 29: Cascaded decimation filter Matlab-Simulink model.	46
Figure 30: Noise sources added to the accelerometer system model.	48

Figure 31: Capacitive sigma-delta MEMS accelerometer MATLAB- SIMULINK model.....	51
Figure 32: Accelerometer model user interface.	52
Figure 33: Fabrication process of DWP accelerometers [46].	55
Figure 34: Layout of DWP-1 accelerometer.	56
Figure 35: Layout of DWP-2 accelerometer.	58
Figure 36: CMOS readout electronics.	59
Figure 37: Fabricated MEMS accelerometer and readout circuit bonded together..	60
Figure 38: Accelerometer 12-position acceleration test placement.....	64
Figure 39: Illustration of 12-position acceleration.	64
Figure 40: 12-position acceleration test set-up.....	65
Figure 41: 12-position acceleration test result of DWP-1 accelerometer.	66
Figure 42: 12-position acceleration simulation result of DWP-1 accelerometer.	67
Figure 43: 12-position acceleration test result of DWP-2 accelerometer.	68
Figure 44: 12-position acceleration simulation result of DWP-2 accelerometer.	69
Figure 45: Clock frequency versus output noise graph obtained from simulation and test of DWP-1 accelerometer.	71
Figure 46: Clock frequency versus output noise graph obtained from simulation and test of DWP-2 accelerometer.	73
Figure 47: DWP-1 accelerometer noise change with increasing decimation order.	76

Figure 48: DWP-2 accelerometer noise change with increasing decimation order.	78
Figure 49: Centrifuge test set-up.	80
Figure 50: Centrifuge test result of DWP-1 accelerometer.	81
Figure 51: Operational range simulation of DWP-1 accelerometer.	82
Figure 52: Centrifuge test result of DWP-2 accelerometer.	83
Figure 53: Operational range simulation of DWP-2 accelerometer.	84
Figure 54: Accelerometer sensing element design algorithm user interface.	90
Figure 55: 1 st accelerometer structure used in design algorithm.	92
Figure 56: 2 nd accelerometer structure used in design algorithm.	94
Figure 57: 3 rd accelerometer structure used in design algorithm.	97
Figure 58: Accelerometer design algorithm trial design for 3 rd structure.	100
Figure 59: Operational range test of the designed accelerometer.	102
Figure 60: Designed accelerometer Allan variance plot and -1/2 slope region.	102

CHAPTER 1

INTRODUCTION

Micro Electro Mechanical Systems (MEMS) have an extensive use in different areas of technology. Inertial sensors (accelerometers and gyroscopes) are one of the most widely used devices fabricated using MEMS technology. MEMS accelerometers play an important role in different application areas such as automotive, inertial navigation, guidance, industry, space applications etc. because of low cost, small size, low power, and high reliability [1]. The performance requirements of the accelerometers are different for each of the mentioned application area. Table 1 shows the required measurement bandwidth, resolution and operational range of accelerometers for these areas [2-5]. Among these application areas, the use of navigation purpose MEMS accelerometers which need high operational range and high resolution is increasing quickly. Capacitive accelerometers with force-feedback structure are generally used because of low temperature dependency, low power consumption, linear operation, low noise floor, and low drift to obtain navigational grade accelerometers. However, it is very difficult to achieve the requirements of navigation purpose accelerometers and a detailed system level mathematical model is a need at this point in order to estimate system level performance of an accelerometer before its fabrication. Therefore, the study presented in this thesis aims to propose a detailed system level model for capacitive force-feedback accelerometers which can be used as a guide at the design stage of the accelerometer by giving approximate performance of the accelerometer.

There are many studies on modeling MEMS accelerometers in the literature. However, most of these models consider specific parts of the system (e.g.

accelerometer or electromechanical Σ - Δ modulator) and they do not take into account noise components and secondary effects of the individual parts. Besides, they do not generally provide verification with test results. This thesis presents such a detailed model with verification through test results.

Table 1: Application areas of accelerometers depending on bandwidth, resolution, and operational range.

Application	Bandwidth	Resolution	Operational Range
Automotive (Airbag release)	0-0.5 kHz	< 500 mg	± 100 g
Stability and control	0-0.5 kHz	< 10 mg	± 2 g
Inertial navigation	0-100 Hz	< 300 μ g	± 20 g
Space measurements	0-10 Hz	< 1 μ g	± 1 g
Medical applications	0-100 Hz	< 10 mg	± 100 g
Vibration monitoring	1-100 kHz	< 100 mg	± 10 g
Head mounted displays	0-100 Hz	< 1 mg	± 10 g

Accelerometers are classified depending on various performance parameters which are explained in Section 1.1. Section 1.2 gives the types of accelerometers categorized due to their acceleration sensing scheme. Then the previous studies in the literature on accelerometer system modeling are explained in Section 1.3. Finally, Section 1.4 provides objective and organization of the thesis.

1.1 Accelerometer Performance Parameters

There are several performance parameters for rating accelerometers which can be listed as bias instability, resolution, sensitivity, range, nonlinearity, bandwidth, cross axis sensitivity, and bias drift [6, 7]. These parameters are described below in detail.

- **Bias Instability:** Bias instability is the instability of the accelerometer output for a constant acceleration input. Bias instability is one of the most important performance parameters to characterize an accelerometer. Bias instability is some kind of a noise whose source is not known and model can not be derived. Bias instability of an accelerometer can be found from Allan variance graph by identifying the stability of '0' slope region. This parameter shows the sensitivity of the accelerometer to the changing conditions and aging. Temperature and environmental variations can cause bias instability and a good packaging which can isolate the accelerometer from the changing conditions can be a solution to decrease bias instability.
- **Resolution:** Resolution is the minimum sensible acceleration by the accelerometer and it is one of the most important performance parameter for rating accelerometers. Resolution is calculated theoretically by dividing output noise spectral density by sensitivity of the accelerometer and multiplying the result with the operation bandwidth. Resolution is a parameter in terms of $g/\sqrt{\text{Hz}}$ and depends on noise floor of the accelerometer. Experimentally, resolution of an accelerometer can be found by plotting its Allan variance graph. The stability of the region having '-1/2' slope, i.e. random walk, is the resolution of the accelerometer. The accelerometer cannot sense accelerations smaller than the resolution value.
- **Sensitivity:** Sensitivity is the change in the accelerometer output for unit change in the acceleration input. This change is in terms of V/g for analog output accelerometers and output units/g for digital output accelerometers. The limiting factor for sensitivity is the operational range of the accelerometer. In the limits of required operational range, the sensitivity

value should be kept at its possible maximum value in order to obtain a high performance accelerometer.

- **Range:** Range is the maximum acceleration that an accelerometer can sense meaningfully. Range is expressed in terms of 'g' units and it means that the accelerometer can not give meaningful output for the input accelerations greater than the range. Range of an accelerometer increases as its sensitivity decreases.
- **Nonlinearity:** Nonlinearity of an accelerometer is the deviation of the linear input-output relation. Nonlinearity is a parameter which depends on accelerometer geometry. Nonlinearity of an accelerometer is named as scale factor instability in accelerometer terminology which corresponds to the change of the scale factor in between the accelerometer operational range. Differential sensing scheme with error cancellation can be used to reduce nonlinearity.
- **Bandwidth:** Bandwidth is the frequency range that input acceleration signal applied to the accelerometer can vary. Bandwidth of the accelerometer can be decreased by reducing damping. Damping of the accelerometer can be reduced by vacuum packaging; however it generates stability problems.
- **Cross-Axis Sensitivity:** Cross-axis sensitivity is the sensitivity of the accelerometer to the off-axis acceleration. If an accelerometer is placed deviated from its sensing axis, accelerometer output change when an off-

axis acceleration is applied. Cross-axis sensitivity should be kept as small as possible by precise placement of the accelerometer.

- **Bias Drift:** Bias drift is the maximum deviation of the accelerometer output with time for a fixed input acceleration signal. Bias drift is determined by looking the peak to peak deviation of the accelerometer output under constant acceleration.

In order to design accelerometer with different specification for the given application areas, many different sensing schemes can be used. Each sensing scheme has its own advantages and disadvantages. The acceleration sensing methods are described in the following section.

1.2 Accelerometer Types

Piezoresistive accelerometer: In this technique, as the proof mass moves with the applied acceleration, the beams which are made of piezoresistive material deform and so their resistance changes [8]. A Wheatstone bridge is generally utilized to measure this resistance change which is proportional to the applied acceleration [9]. Piezoresistive accelerometers can sense accelerations down to zero Hertz. However, this type of accelerometers has large sensitivity to temperature changes.

Piezoelectric accelerometer: In this type of accelerometers, piezoelectric materials such as quartz, PVDF, BaTiO₃ etc. are utilized which produce electrical polarization according to the stress when acceleration is applied. This electrical polarization causes a charge to be generated which is either given as charge output or converted to voltage and then given as output of the accelerometer [9]. These accelerometers

have difficulty in low-frequency measurements because of the DC charge produced. Also these devices are not compatible with CMOS fabrication [10].

Thermal accelerometer: Thermal accelerometers use the principle that the temperature flux between a heater and a sink plate is inversely proportional to the applied acceleration. Thus, the temperature change giving information about the applied acceleration is measured by an array of thermopiles. These accelerometers have small sensitivity and small bandwidth [11].

Electromagnetic accelerometer: Mutual inductance of two closely spaced coils is employed in these accelerometers. Here, one coil is put on the proof mass and the other is on a fixed frame separated by an air gap. The proof mass displacement due to external acceleration changes the mutual inductance of these two coils. These accelerometers have simple structure and good linearity; however, they have very small sensitivity and small SNR (Signal-to-noise ratio) [10].

Optical accelerometer: Optical accelerometers have a light source in order to measure applied acceleration by means of photodiodes, shutter modulation, and fiber optic interferometry [12, 13]. These accelerometers have very high Electro Magnetic Interference (EMI) immunity and good linearity; however they do not provide high resolution and because of the light source, they cannot be used in a small package.

Resonant beam accelerometer: Resonant beam accelerometers transfer the force generated on the proof mass due to external acceleration to the resonant structures. When a tensile stress occurs on these resonant structures, the resonant frequency increases and vice versa when a compressive stress occurs on these resonant structures, the resonant frequency decreases. This change in resonant frequency gives information about the external acceleration. This type of accelerometers has some disadvantages like complex fabrication process and low scale factor [14, 15].

Capacitive accelerometer: Capacitive accelerometers use capacitors formed between the proof mass and the fixed conductive electrodes. The proof mass displacement due to external acceleration introduces capacitance change (either the gap or area changes) between proof mass and electrodes which is directly related to input acceleration [16].

Among these various sensing schemes of accelerometers, capacitive sensing is generally preferred since it provides low temperature dependency, high voltage sensitivity, low noise floor, and low drift. Operation range of a capacitive accelerometer can be increased significantly by operating it in closed-loop mode. Therefore, capacitive accelerometers are studied in this thesis since it is aimed to obtain navigation purpose accelerometer which requires low noise, high operational range and low bandwidth.

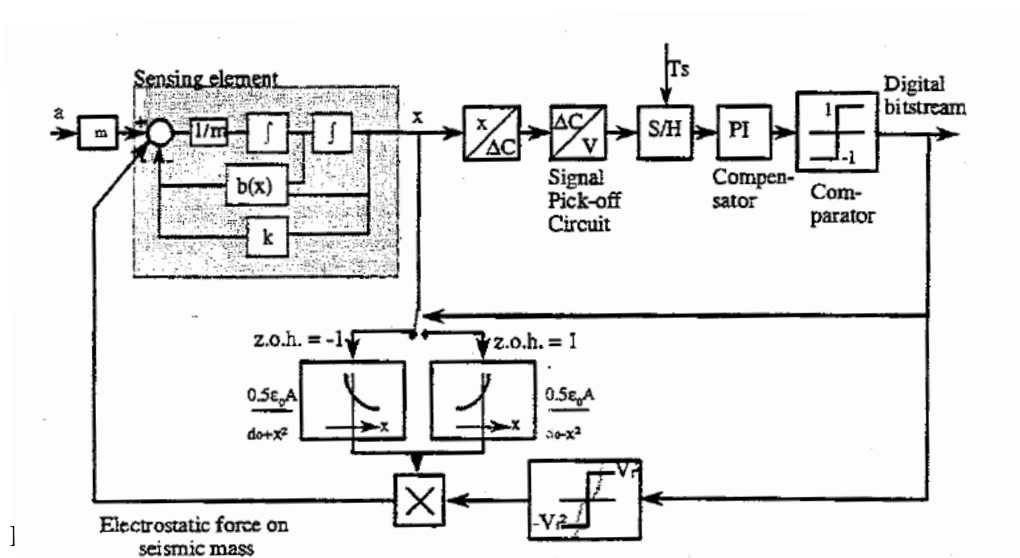
Capacitive accelerometers require capacitive bridge structured readout electronics to sense the capacitance change and to operate in force-feedback for increased operation range and linearity. Combined with the readout electronics, the accelerometer system becomes complicated because of having both mechanical and electrical components defining the overall performance. In this study, capacitive accelerometer with its interface electronics and signal processing units is modeled to estimate system level performance of an accelerometer system and this model is analyzed and compared with test results.

The next section gives some examples on capacitive accelerometer modeling in literature and the structures used in these studies, their modeling approach and insufficient parts of these models are given.

1.3 Previous Studies

There are various studies on modeling capacitive accelerometer in the literature. Most of these studies give model of the individual building blocks of an accelerometer system. There is a very small number of works modeling the accelerometer system including the sensing element and control electronics together. In this section of the thesis, some of these studies will be given.

Figure 1 shows SPICE model of a silicon micromachined accelerometer system with its control electronics implemented by Coventry University and University of California [17]. Capacitive accelerometer sensing element and the interface electronics are represented in the SPICE model.



electronics, Berkeley Sensors and Actuators Center and Nonlinear Systems Design Group [17].

The model given in Figure 1 includes sensing element, the control electronics, and the electrostatic feedback forces. This model basically aims to investigate the dynamic performance of the sensing element itself because it includes sensing element at system level, but interface electronics at component level [17]. This model can help to develop alternative interface electronics and control strategies, but since it does not take into account the noise sources generated by the mechanical and electrical parts and the signal processing, it does not give idea about the system level performance of the accelerometer.

Another study on accelerometer modeling is performed by Harbin Institute of Technology, China [18]. In this study, system level modeling of a silicon force-balanced capacitive MEMS accelerometer is implemented as shown in Figure 2. This model is also implemented in VHDL-AMS environment and the simulation results are compared with Simulink simulation results.

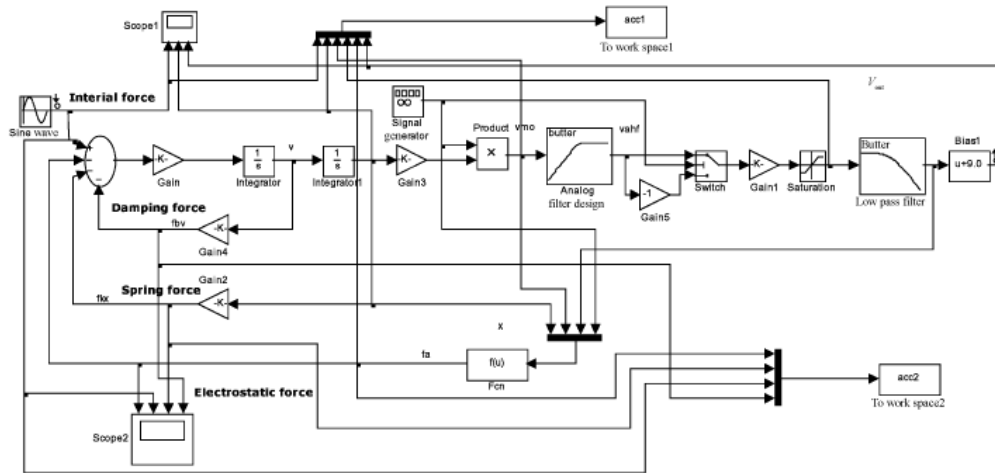


Figure 2: Simulink model of a force-balanced MEMS accelerometer implemented by Harbin Institute of Technology, China [18].

This study gives comparison of system level simulations done in SIMULINK and VHDL-AMS environment for an accelerometer. However, it does not give verification with experimental results and it does not include noise components.

In the study carried out by Department of Earthquake Engineering, I.I.T. Roorkee, India, system level simulation of servo accelerometer in Simulink is given [19]. In this study, the sensing element is modeled at system level and the control and interface electronics are modeled at component level using MATLAB SIMMECHANICS tool as shown in Figure 3: Simulink block diagram of a force-balanced capacitive accelerometer implemented by I.I.T. Roorkee, India [19]. The model implemented in this study is used to estimate the dynamical behavior of the accelerometer before implementing the sensor in the hardware. However this model is not verified with test results.

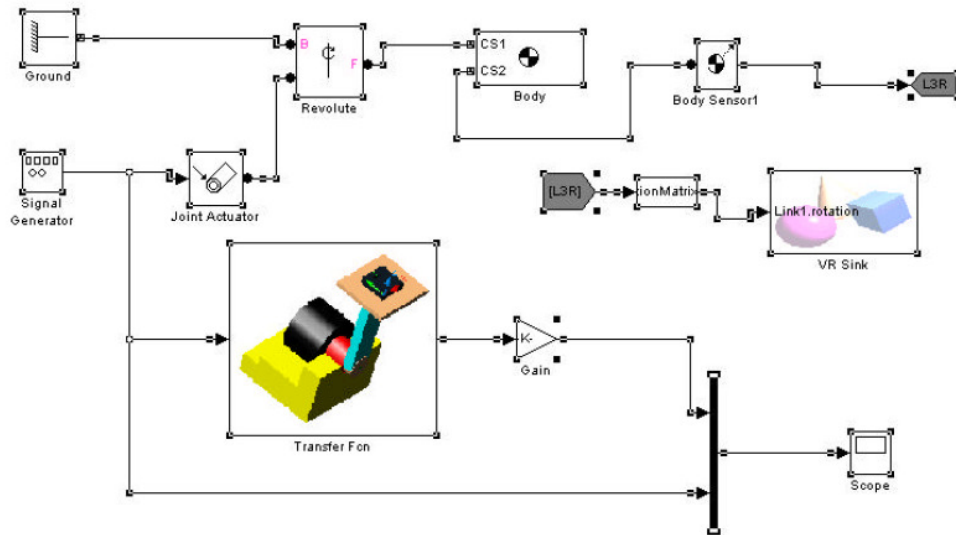


Figure 3: Simulink block diagram of a force-balanced capacitive accelerometer implemented by I.I.T. Roorkee, India [19].

One of the studies on accelerometer modeling is handled by Teodor Lucian Grigorie, University of Craiova, Romania [20] which presents the Matlab/Simulink modeling and numerical simulation of an analog capacitive micro-accelerometer [20]. Using this model, it is proved that the closed loop operation of the accelerometer is better in dynamical performance than the open loop operation of the accelerometer. This study basically focuses on dynamical performance analysis of an accelerometer system by making simulations with the model given in Figure 4. This model is a complete system model including sensing element, interface electronics and signal processing following the interface electronics, but does not include the noise models.

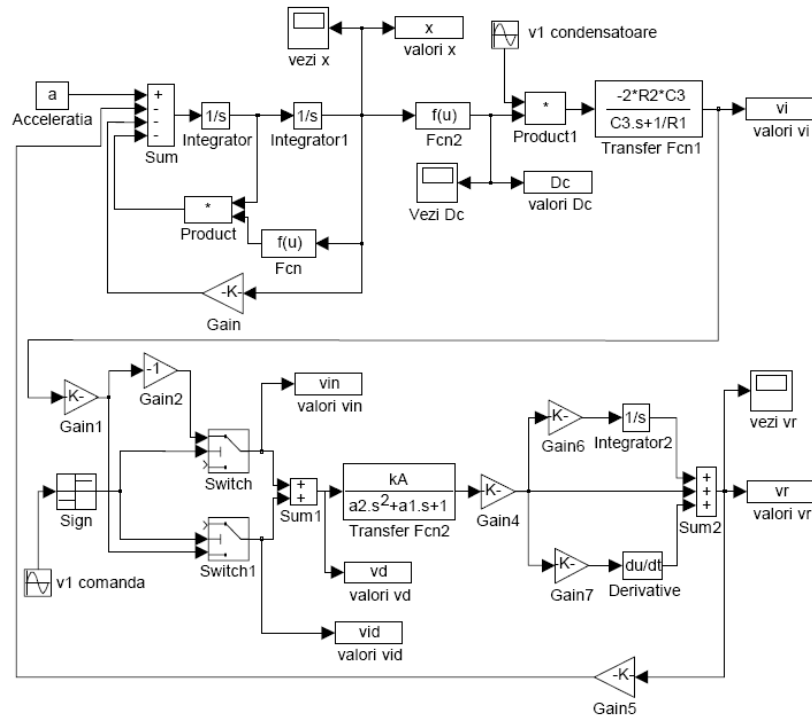


Figure 4: Matlab/Simulink model of an analogue capacitive micro-accelerometer generated by University of Craiova, Romania [20].

All of these previous studies neither use noise models to estimate the performance of an accelerometer more realistic nor give verification of the proposed model with test results. In this thesis study, a detailed model for conventional capacitive Σ - Δ accelerometer systems with experimental verification is presented. The model proposed in this thesis is a detailed system level one including sensing element, interface electronics, and signal processing unit. The individual noise sources from mechanical and electrical parts are also added to model. This model is then verified through test results. In the next section, the objectives and organization of the thesis is given.

1.4 Objectives and Organization of the Thesis

The purpose of this thesis study is to propose a detailed MATLAB-Simulink model for an electromechanical Σ - Δ capacitive accelerometer system which can be used to estimate the system level performance. The following summarizes the objectives and organization this thesis.

- *Detailed modeling of a capacitive Σ - Δ accelerometer system.*

Matlab-Simulink model of a capacitive sigma-delta MEMS accelerometer system is proposed including MEMS accelerometer, closed-loop readout electronics, signal processing units, and noise sources. The aim is to obtain a reliable model which can be used to estimate the performance of an accelerometer before its implementation.

- *Verification of the proposed model through test results*

The proposed accelerometer model is verified using the implemented accelerometer system. System level test results of this accelerometer are

compared with simulations in terms of noise performance, scale factor, operational range, and open loop sensitivity.

- *Writing an accelerometer sensing element design algorithm based-on the developed model.*

After the verification, an accelerometer sensing element design algorithm is written using the developed model. This algorithm tries to find the minimum noise accelerometer sensing element dimensions within some specifications and requirements. An accelerometer sensing element is fabricated using the dimensions obtained from this algorithm. The performance tests of this accelerometer is performed and compared with the values found with the algorithm.

Chapter 2 of this thesis gives the theory of the capacitive accelerometer systems where their building blocks, structures, functions, and performance criteria are discussed.

Chapter 3 presents the accelerometer model proposed within this study. The model is described step by step in detail to describe how the model is generated.

Chapter 4 gives the verification of the proposed model through test results and noise analyses of implemented accelerometer system. This chapter gives detailed functionality tests and noise analyses of the accelerometer system.

Chapter 5 defines an algorithm written to design the accelerometer sensing element within defined die size, performance criteria, and process limitations.

Finally, Chapter 6 gives the conclusion of the thesis and defines possible future works on this topic.

CHAPTER 2

CAPACITIVE MEMS ACCELEROMETER SYSTEM THEORY

Capacitive accelerometer systems are composed of three main blocks which are sensing element (capacitive accelerometer), interface electronics, and signal processing units. This Chapter gives the theory of these three main blocks with their working principles and critical parameters.

2.1 Sensing Element: Capacitive Accelerometers

Capacitive type sensing is one of the most popular approaches for acceleration sensing, due to its low temperature dependency, high voltage sensitivity, low noise floor, low drift, and large operation range in closed-loop mode. In this section, the theory of capacitive MEMS accelerometers will be explained.

A capacitive MEMS accelerometer is a mechanical structure which converts applied acceleration into capacitance change. It contains a proof mass free to move due to applied acceleration, spring shaped connections to substrate, and fingers forming capacitor with the fingers of fixed electrodes which changes due applied acceleration. Therefore the dimensions and structure of the accelerometer affecting this capacitor value are basic parameters defining the performance of the sensing element. Figure 5 shows the general structure of the capacitive MEMS accelerometer. The basic elements of accelerometer are proof mass, fingers and springs.

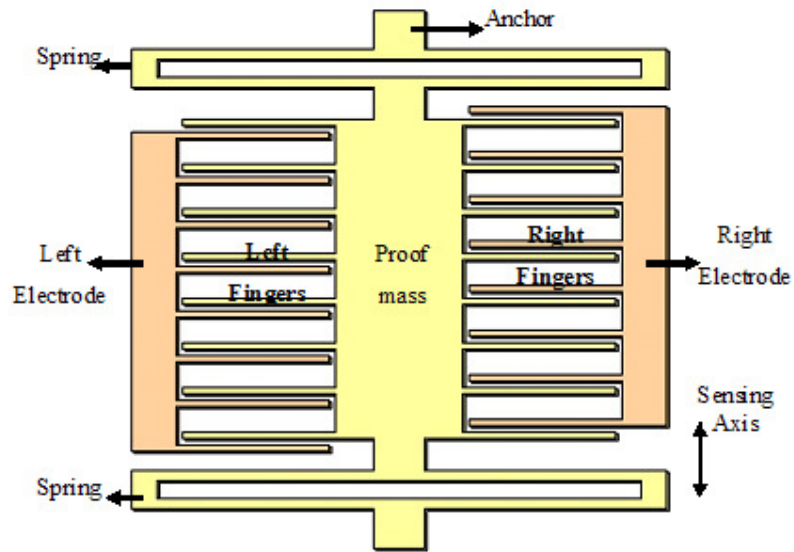


Figure 5: General structure of capacitive MEMS accelerometers.

Figure 6 gives illustration of capacitive MEMS accelerometer dimensions used for capacitance calculation. When acceleration is applied in the sensing axis, proof mass will move in the opposite direction of the applied acceleration which will introduce a capacitance increase in one side and capacitance decrease in the other side of the accelerometer as illustrated in Figure 7. This capacitance change is proportional to applied acceleration and sensed by a sigma-delta type data converter which is described in Section 2.2.

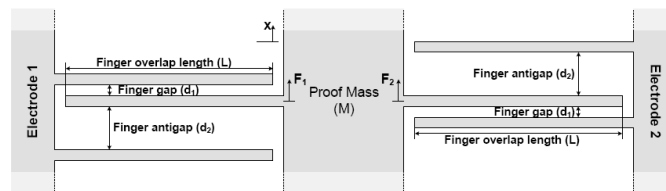


Figure 6: Illustration of capacitive MEMS accelerometer dimensions.

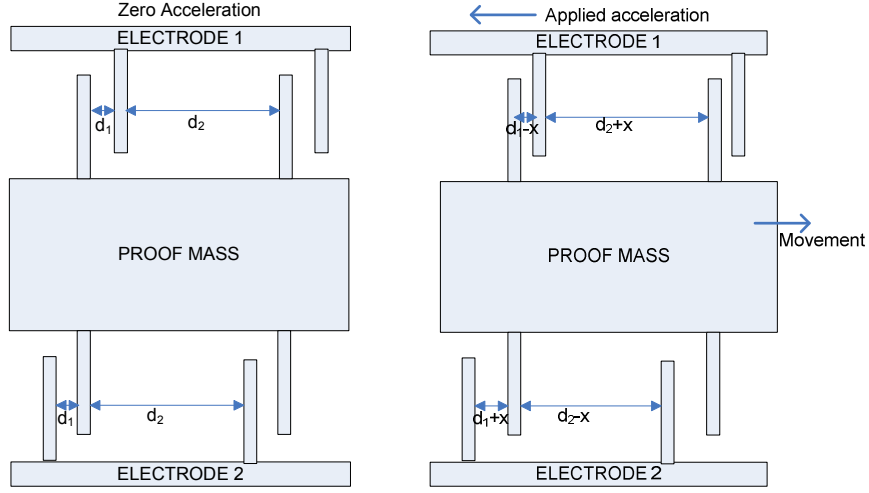


Figure 7: Capacitance change depending on the applied acceleration.

$$C_{rest} = \frac{N\epsilon_0 h L_{finoverlap}}{d_1} + \frac{(N-1)\epsilon_0 h L_{finoverlap}}{d_2} \quad (1)$$

$$C_{1,2} = \frac{N\epsilon_0 h L_{finoverlap}}{d_1 \mp x} + \frac{(N-1)\epsilon_0 h L_{finoverlap}}{d_2 \pm x} \quad (2)$$

where, N is the number of fingers per side, h is the structural thickness, $L_{finoverlap}$ is the fingers overlapping length, d_1 and d_2 are finger spacings and ϵ_0 is the permittivity of air. Equation (1) gives rest capacitance of an accelerometer system and Equation (2) gives the relation between the capacitance and proof mass displacement due to applied acceleration.

The next section will describe the capacitive interface electronics to sense and read the capacitance change of the accelerometer occurred due to external acceleration.

2.2 Capacitive Interface Electronic

There are three generally used capacitive interface structures in the literature [21]. These structures can be listed as ac-bridge with voltage amplifier [22], transimpedance amplifier [23], and switched-capacitor circuit with charge integrator [24]. Among these three structures, switched-capacitor circuit with charge integrator is generally preferred as the interface circuit of capacitive accelerometers because it does not need a separate demodulator and it provides high performance accelerometer with its parasitic capacitance independent output. In this thesis study, switched-capacitor with charge integrator using full bridge topology is used as the interface circuit and it is realized with a sigma-delta modulator. Sigma-delta modulator provides low noise and small bandwidth matching the requirements of the navigation purpose accelerometers studied in this thesis.

2.2.1 Sigma-Delta Modulator

Sigma-delta type modulators are analog to digital converters generally preferred for high resolution and low bandwidth applications. High resolution and low bandwidth is obtained by oversampling and noise shaping techniques used in sigma-delta modulators. This property of sigma-delta modulators make them a good candidate to be used as the interface electronics of navigation purpose capacitive accelerometer which require low bandwidth ($<2\text{kHz}$) and high resolution.

Sigma-delta modulator converts the capacitance change introduced by the capacitive accelerometer into digital 1-bit signal and provides feedback to the accelerometer to make the proof mass stay at its null position. When combined with the MEMS accelerometer, an electromechanical sigma-delta structure is obtained as shown in Figure 8.

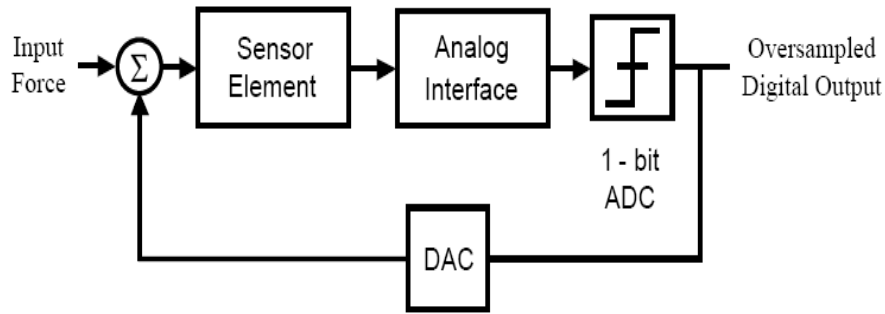


Figure 8: Block diagram of an electromechanical Sigma-Delta modulator [25].

The capacitance change of both left and right side of the accelerometer is converted into voltage at the analog interface block which is usually a charge integrator. Then these analog voltages are used to produce 1-bit oversampled digital output by 1-bit ADC which is usually a comparator. The 1-bit output is either 1 or 0 depending on the direction of the applied acceleration. This output is used for both obtaining acceleration data and generating feedback voltage. Feedback to the accelerometer is applied via a switch which either gives a positive or a negative voltage to the proof mass depending on the output bit in order to keep the proof mass at its null position. While applying feedback, electrodes in the right and left side are kept at constant opposite potentials to be able to generate feedback force in either direction.

2.2.1.1 Oversampling and Noise Shaping in Sigma-Delta Modulators

In sigma-delta modulators, sampling is done at a high sampling frequency to increase the resolution and decrease the inband noise of accelerometer systems [26]. In closed loop electromechanical system, the displacement of the proof mass is kept very small by feedback in order to minimize nonlinearity. The more the displacement is kept small, the more the system will be linear. To keep displacement small, sampling frequency is chosen high which is described as

oversampling. Oversampling means that the sampling frequency is much greater than the Nyquist frequency (two times the input signal bandwidth) [27, 29]. By this way, while the quantization power stays constant, it can be spread over a wider frequency range which means the quantization noise at the frequency of interest is smaller than Nyquist converter quantization noise. When sampling is done at Nyquist frequency the quantization noise is large at the frequency of interest as shown in Figure 9 (a) and when oversampling is done the quantization noise is small at the frequency of interest as shown in Figure 9(b) [27].

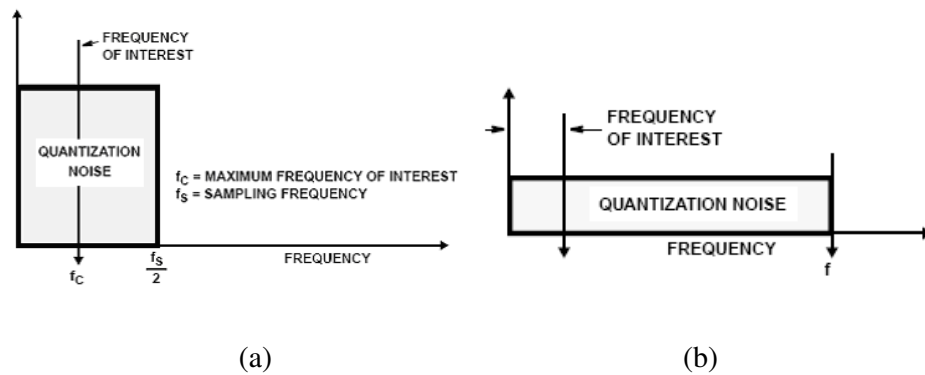


Figure 9: (a) Nyquist converter quantization noise spectrum, (b) oversampled converter quantization noise [27].

In order to see the effect of the sigma-delta converter on oversampling, the linearized model of a first order sigma delta modulator is used since it will be easy to analyze. In this linearized model, the analog interface of the sigma-delta readout circuit which is the charge integrator is modelled with a transfer function of $1/s$ and the comparator is modeled with a noise source of $N(s)$. This linearized model of the first order sigma delta converter is given in Figure 10 [27, 35].

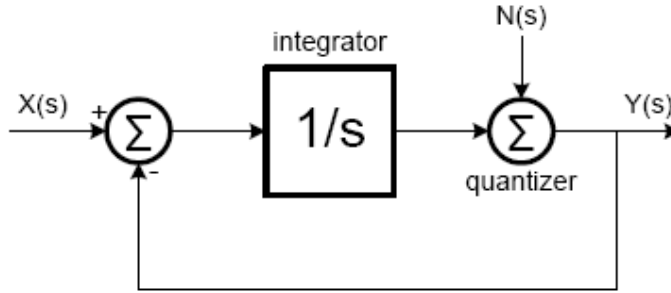


Figure 10: Linearized model of first order sigma delta modulator.

If we assume $N(s)=0$ in the linearized model given in Figure 10 and calculate $Y(s)/X(s)$, it can be seen that the input signal is low-pass filtered [28] as given in Equation (3).

$$Y(s) = [X(s) - Y(s)] \begin{bmatrix} 1 \\ s \end{bmatrix}$$

$$\frac{Y(s)}{X(s)} = \frac{1/s}{1 + 1/s} = \frac{1}{s + 1} \quad (3)$$

If we assume there is no input applied to the linearized model given in Figure 10 and calculate $Y(s)/N(s)$, it can be seen that the noise is shifted to high frequencies as given in Equation (4)[27, 28].

$$Y(s) = -Y(s) \begin{bmatrix} 1 \\ s \end{bmatrix} + N(s)$$

$$\frac{Y(s)}{N(s)} = \frac{1}{1 + 1/s} = \frac{s}{s + 1} \quad (4)$$

The signal and noise spectrum of an oversampling first order sigma-delta converter is shown in Figure 11 [27]. As it can be seen from the figure the quantization noise is shifted to high frequency and the noise in the band of interest considerably decreased. The noise in the band of interest can be decreased more by increasing the order of the sigma-delta modulator [29].

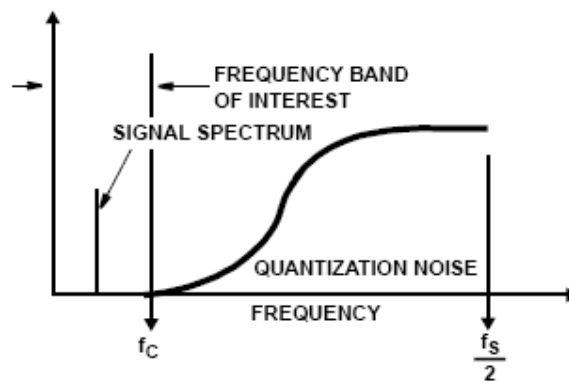


Figure 11: Oversampled first order sigma-delta quantization noise spectrum.

To conclude, sigma-delta modulator is a good candidate to be used as the interface electronics of navigation purpose capacitive accelerometer because it provides high resolution and low bandwidth matching the requirements of the accelerometer.

2.3 Signal Processing Units

The oversampled 1-bit digital output of the sigma-delta readout circuit should be processed because it contains noise components at high frequencies and data rate is

very high. Decimation filters are used to eliminate the noise shifted to high frequencies, to get rid of redundant output data, and to decrease the data rate.

In order to realize decimation filters generally Sinc filters are utilized because of their low-pass nature and easy implementation [29]. Sinc filters are low-pass filters composed of addition and subtraction blocks. Structure of a Sinc^M filter is shown in Figure 12 [29]. Addition blocks adds the input and previous addition result, subtraction blocks subtract previous input from coming input. The 1-bit input of the decimation filter is passed through the first addition block, then the output of the first addition block is passed through the second addition block and so on upto M^{th} addition block. One from the N outputs of the M^{th} addition block is sent to the first subtraction block, then the output of the first subtraction block is sent to the second subtraction block and so on upto M^{th} subtraction block.

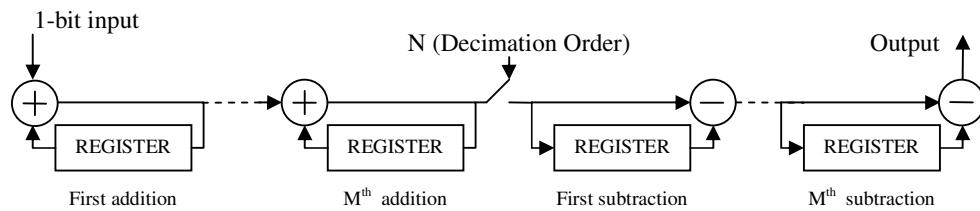


Figure 12: Structure of a Sinc^M filter.

Here, M is defined as the degree of the decimation filter and N is defined as the decimation order of the filter. It is necessary to define the transfer functions of addition and subtraction blocks given in Figure 13 and Figure 14 respectively. The addition block transfer function can be obtained in Z-domain with Equation (5).



Figure 13: Addition block of Sinc filter.

$$\begin{aligned}
 y(n) &= x(n) + y(n-1) \\
 Y(z) &= X(z) + Y(z)z^{-1} \\
 \frac{Y(z)}{X(z)} &= \frac{1}{1-z^{-1}}
 \end{aligned}
 \tag{5}$$

The subtraction block function can be obtained in Z-domain with Equation (6).



Figure 14: Subtraction block of Sinc filter.

$$\begin{aligned}
 y(n) &= x(n) - x(n-1) \\
 Y(z) &= X(z) - X(z)z^{-1} \\
 \frac{Y(z)}{X(z)} &= 1 - z^{-1}
 \end{aligned}
 \tag{6}$$

The important part of Sinc filter design is to specify the M (degree of decimation filter) and N (decimation order) values. M is determined by the degree of the closed loop electromechanical sigma-delta system and N is specified with the required bandwidth of the system. In order to obtain a low noise output from Sinc filter, its degree should be at least 1 greater than the degree of the closed loop electromechanical sigma-delta system [29]. As the degree of the Sinc filter increases, the noise at high frequencies is filtered more since the magnitude of the ripple of the filter at high frequencies decreases.

The output of the Sinc filter is a number which can be expressed as a k -bit digital number. The number of bits ' k ' can be calculated by the formula given in Equation (7).

$$k = M \log_2(N) + b \quad (7)$$

where, M is the decimation filter degree, N is the decimation order, b is the number of bits in the input word and k is the number of bits in the output word[29].

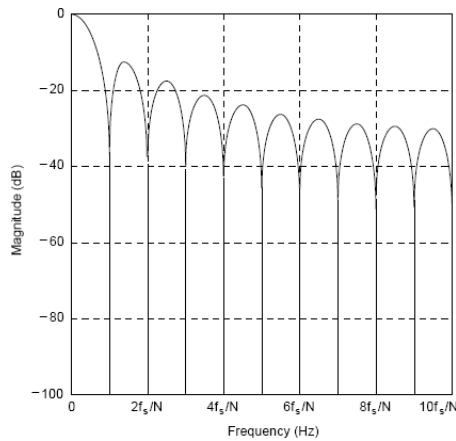


Figure 15: First-order Sinc filter response [30].

Figure 15 gives the filter response of a first order Sinc filter where f_s is the sampling frequency and N is the decimation order [30]. As it can be seen from figure, Sinc filter is a low-pass filter with ripples at high frequencies. These ripples at high frequencies can be decreased by increasing the filter order [29, 30]. However increasing filter order generates a complicated filter structure and increase the response time of the filter.

2.4 Noise Sources of a Capacitive Sigma-Delta MEMS Accelerometer

Capacitive accelerometer systems have mechanical and electrical parts together as explained in Section 2.3 and Section 2.4. Each of these parts introduces individual noises to the system which affects the overall system performance. Resolution of a capacitive accelerometer system is mainly dependent on these noise sources which can be grouped as mechanical and electrical noise sources.

2.4.1 Mechanical Noise

The capacitive accelerometer has a mechanical structure composed of fixed electrodes, proof mass, and springs. This mechanical structure has mechanical noise named as Brownian noise which is generated by thermal motion of gas molecules inside this mechanical structure. Brownian noise basically depends on temperature, damping factor of the accelerometer, and proof mass.

Brownian noise of a capacitive accelerometer can be calculated using Equation (8) [39]. Sampling frequency (500 kHz) of the accelerometer system used in this study is much greater than the accelerometer bandwidth (about 2 kHz), so the frequency terms in the Brownian noise derivation [39] is neglected.

$$F_n^2 = 4k_b T b$$

$$a_n^2 = \frac{4k_b T b}{9.81^2 m^2} \quad (8)$$

where, k_b is Boltzman constant, T is temperature in Kelvin, b is the damping of the accelerometer, m is the proof mass, F_n is brownian noise in terms of force and a_n is the brownian noise in terms of gravitational acceleration.

Brownian noise can be lowered by reducing the damping factor or using large proof mass. One way to decrease the damping factor is vacuum packaging, however vacuum packaging will generate stability problems.

2.4.2 Electrical Noise

Combining the accelerometer with its interface electronics introduces electrical noises to the system. The electrical noises generated by interface electronics are thermal noises and quantization noise due to analog to digital conversion process. In closed loop operation, mass residual motion noise occurs due to the oscillation of the proof mass with the applied feedback force. Electrical noises can be listed as amplifier noise, kT/C noise, quantization noise, and mass residual motion noise. In the following sections these noises will be described.

2.4.2.1 Amplifier Noise

Amplifier noise comes from the sigma-delta readout circuit including the thermal and flicker noise of the amplifier in the readout circuit. In the readout circuit, correlated double sampling (CDS) technique can be used to cancel the amplifier flicker noise. With CDS technique, in feedback phase, noise and offset is sampled

on CDS capacitors, then in the next sensing phase, flicker noise and offset is removed [40]. Therefore, the dominant noise source of the amplifier noise is thermal noise when CDS technique is used. Amplifier noise depends on temperature, integration capacitance used in the charge integrator of the readout circuit and sampling frequency as given in Equation (9).

$$V_{out_thermal} = \sqrt{\frac{16}{3} \frac{C_s + C_p}{C_{int}} \frac{k_b T}{C_{out}} \frac{1}{f_s}} \quad (9)$$

where, C_s is the sensing capacitance value of the accelerometer, C_p is the parasitic capacitance, C_{int} is the integration capacitance, k_b is Boltzmann constant, T is temperature in Kelvin, C_{out} is the output capacitance, f_s is the sampling frequency and $V_{out_thermal}$ is output referred thermal noise of the amplifier in $V/\sqrt{\text{Hz}}$. It is obvious from Equation (9) that amplifier noise can be decreased by increasing the sampling frequency.

2.4.2.2 kT/C Noise

kT/C noise is the thermal noise coming from the switches used in the readout circuit. It is an electrical noise source and mostly depends on the integration capacitance value and sampling frequency as given in Equation (10) [42].

$$V_{out_kT/C} = \sqrt{\frac{4k_b T}{f_s C_{int}}} \quad (10)$$

where, k_b is Boltzmann constant, T is temperature in Kelvin, f_s is sampling frequency, C_{int} is the integration capacitance and $V_{out_kT/C}$ is output referred thermal

noise generated by the switches. This output referred noise coming from the switch capacitors is calculated using the equation given in Equation (10).

2.4.2.3 Quantization Noise

Quantization noise is effective under closed loop operation. This noise source is generated when analog to digital conversion is done in the readout circuit. Quantization noise dominantly depends on oversampling ratio because oversampled sigma-delta modulator shifts quantization noise high frequencies and as the oversampling ratio increases, the inband quantization noise decreases as described in Section 2.2.1 . Quantization noise can be calculated by the formula [43] given in Equation (11).

$$Quantization_noise = e_{rms} \frac{\Pi^n}{M^{n+0.5} \sqrt{2n+1}} \quad (11)$$

where, $e_{rms} = \frac{\Delta}{\sqrt{12}}$, M is oversampling ratio and N is the order of sigma-delta. In

this thesis study, the analog to digital converter of the readout circuit is a 1-bit quantizer and it introduces a quantization noise which can be modelled with the formula given in Equation (11). Quantization noise can be lowered by increasing oversampling ratio or increasing the decimation order of the decimation filter which results in decrease in the cut-off frequency of the decimation filter.

2.4.2.4 Mass Residual Motion Noise

Mass residual motion is effective under closed loop operation of the electromechanical sigma-delta system. In closed loop operation, the pulse train

output of the sigma-delta readout circuit is given as feedback to the proof mass which results in the oscillation of the proof mass around the equilibrium position. This oscillation exists even at zero input. This periodic motion of the proof mass is taken into account as a noise source to the system which is called as mass residual motion noise. This noise source is dominant with accelerometers having small proof mass and large operational range [44]. Mass residual motion can be calculated with Equation (12).

$$N_{rm} = 4 \frac{f_{BW}}{f_s} \left(\frac{K}{M} \right) \frac{a_{fb}}{(2\pi f_s / 4)^2} \quad (12)$$

where, f_{BW} is input signal bandwidth, f_s is sampling frequency, K is spring constant of the accelerometer, M is the proof mass, a_{fb} is the feedback in terms of acceleration and N_{rm} is the mass residual motion noise in terms of acceleration.

Mass residual motion noise can be decreased by increasing the sampling frequency of the system since it is inversely proportional to the square of sampling frequency.

In this chapter, the theory of capacitive accelerometer systems is given and as it is explained, the capacitive accelerometer system has a complicated structure which makes it difficult to analyse. In order to analyse accelerometer at system level before its design, a simulation tool should be constructed. In the next chapter, the MATLAB-SIMULINK model constructed for conventional capacitive accelerometer system [31] is presented which can be used to estimate system level performance of the accelerometer before fabrication.

CHAPTER 3

CAPACITIVE SIGMA-DELTA MEMS ACCELEROMETER SYSTEM MATLAB-SIMULINK MODEL

In this chapter, the MATLAB-SIMULINK model of a capacitive sigma-delta MEMS accelerometer generated within this thesis study will be given. The model is composed of four main blocks which are capacitive MEMS accelerometer (mechanical part), sigma-delta readout, decimation filter, and noise sources [32]. The block diagram of the full accelerometer system is shown in Figure 16. Based on this block diagram the accelerometer system model is proposed as described in the following sections.

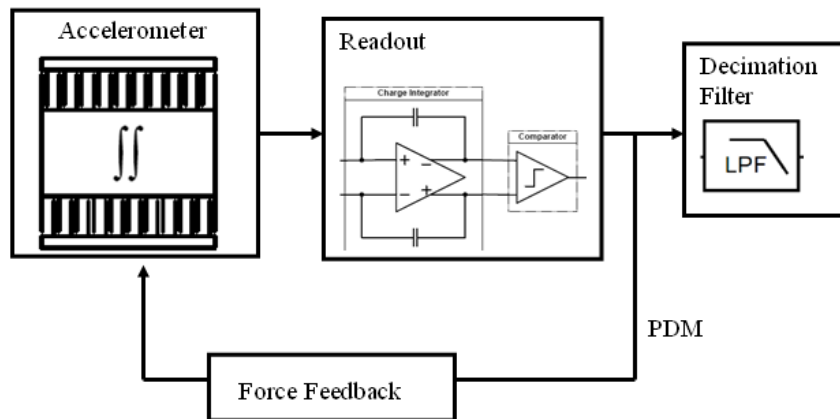


Figure 16: Block diagram of the full accelerometer [32].

3.1 Capacitive MEMS Accelerometer Model

Capacitive MEMS accelerometers work in capacitive sensing scheme and have capacitive fingers to convert applied acceleration into capacitance change as described in Section 2.1. Capacitive MEMS accelerometer is modeled with a transfer function converting applied acceleration into displacement and a displacement to capacitance change converter block. In the next sections these two blocks will be described in detail.

3.1.1 Accelerometer Transfer Function

The most common structure used to model capacitive MEMS accelerometer is mass-spring-damper system. Proof mass of the accelerometer corresponds to mass, spring shaped structure of the accelerometer corresponds to spring and damping inside the accelerometer behaves as damper. The structure mass-spring-damper system [33] which is used to model capacitive MEMS accelerometer is given in Figure 17.

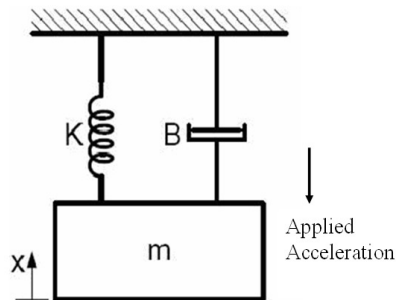


Figure 17: Mass-spring-damper system.

In Figure 17, M is the mass, K is the spring, and B is the damping of the system. When an external acceleration is applied to the system, mass will deviate from its equilibrium position. The force balance equation is given in Equation (13) where x is the displacement of the mass and a_{ext} is the applied external acceleration. The transfer function obtained from the force-balance equation is given in Equation (14).

$$ma_{ext} = mx'' + Bx' + Kx \quad (13)$$

$$\frac{X(s)}{a_{ext}(s)} = \frac{1}{s^2 + \frac{B}{m}s + \frac{K}{m}} \quad (14)$$

As it can be seen from Equation (14), the transfer function is a second order transfer function. Similarly, the transfer function of the fixed electrodes can be expressed with Equation (15).

$$\frac{X(s)}{a_{ext}(s)} = \frac{1}{s^2 + \frac{B}{m_{electrode}}s + \frac{K_{electrode}}{m_{electrode}}} \quad (15)$$

where $m_{electrode}$ is the electrode mass and $k_{electrode}$ is the electrode spring constant. Spring constant of the fixed electrodes are considerably higher than the proof mass of the accelerometer. Hence, the movement of the fixed electrodes is very small compared to proof mass movement that can be ignored.

Here, it is necessary to find the mass, spring constant and damping values of an accelerometer to obtain the transfer function between displacement of proof mass

and external acceleration. After obtaining the transfer function, displacement to capacitance change part of the accelerometer should be modelled. In the next sections, computation of mass, spring constant, damping and displacement to capacitance change is described.

3.1.1.1 Mass

In order to calculate mass of a capacitive MEMS accelerometer, proof mass and mass of fingers connected to the proof mass should be taken into account. Figure 18 gives the dimensions of a typical capacitive MEMS accelerometer.

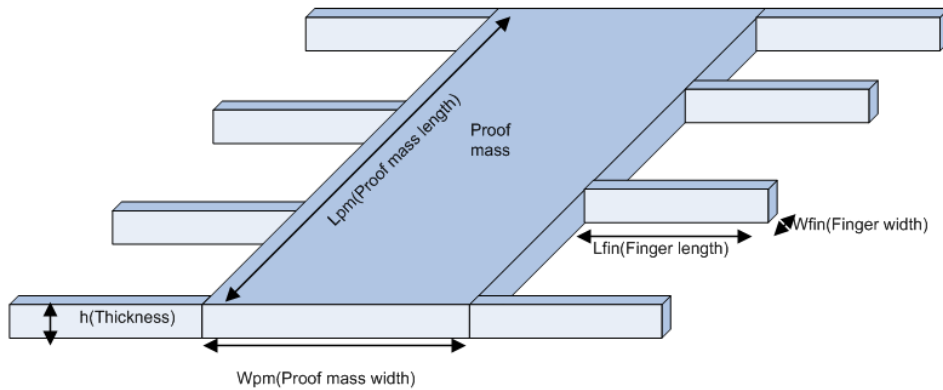


Figure 18: Illustration of capacitive MEMS accelerometer dimensions.

Using the dimensions given in Figure 18 mass of an accelerometer can be calculated with Equation (16).

$$m = W_{pm} L_{pm} h d + 2N W_{fin} L_{fin} h d \quad (16)$$

where, $d=2330 \text{ kg/m}^3$ (silicon density) and N is the number of fingers per side. If there exists etching holes on the proof mass the formula given can be improved as given in Equation (17).

$$m = W_{pm}L_{pm}hd + 2NW_{fin}L_{fin}hd - N_{etch}\pi r^2hd \quad (17)$$

where, N_{etch} is number of etching holes and r is the radius of etching holes.

3.1.1.2 Damping

Capacitive MEMS accelerometer damping comes from viscous flow of gas molecules around the accelerometer. Under acceleration, proof mass moves resulting in the gas molecules flow below and above itself and squeeze between capacitive fingers [35, 37]. Gas molecules flow and squeezing between the fingers are taken into account as damping factor. Damping of a capacitive accelerometer coming from Couette flow and Squeeze film damping are described below in detail.

- **Couette flow:** Couette flow is observed as gas flow between the proof mass and top plate and between the proof mass and substrate when acceleration is exerted as shown in Figure 19.

As it can be seen from Figure 19, when proof mass moves due to applied acceleration, there occurs a Couette flow above and below it. This flow shows an effect of damping which can be calculated by the formula given in Equation (18) [35, 37].

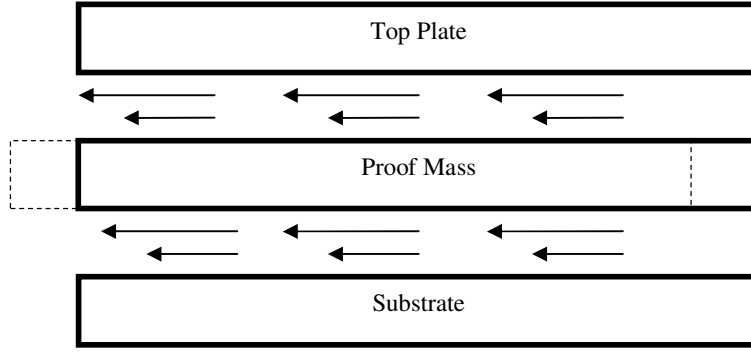


Figure 19: Couette flow between proof mass and substrate and top plate.

$$B_{couette} = \frac{\mu}{d_f} A + \frac{\mu}{\delta} A \quad (18)$$

where, μ is the viscosity of the environment, d_f is the distance between the proof mass and substrate, δ is the distance between proof mass and top plate, and A is the overlapping area of proof mass with the top plate and substrate.

Squeeze Film Damping: Squeeze film damping comes from the gas molecules squeezing between the proof mass fingers and electrodes fingers. When proof mass and proof mass fingers moves due to the applied acceleration, gas molecules in between the fingers squeezes which results as a damping factor [38]. Squeeze film damping is illustrated in Figure 20. Squeeze film damping can be calculated from the equation given in Equation (19).

$$B_{squeeze} = c\mu h^3 L_{fin} \left[\frac{2N}{d_1^3} + \frac{2(N-1)}{d_2^3} \right] \quad (19)$$

where, N is the number of fingers per side, d_1 is the small distance between fingers, d_2 is the large distance between fingers, h is the thickness, L_{fin} is the finger length, and c is a factor depending on thickness (h) and finger length (L_{fin}). The factor ‘ c ’ can be found using the graph given in Figure 21 [45].

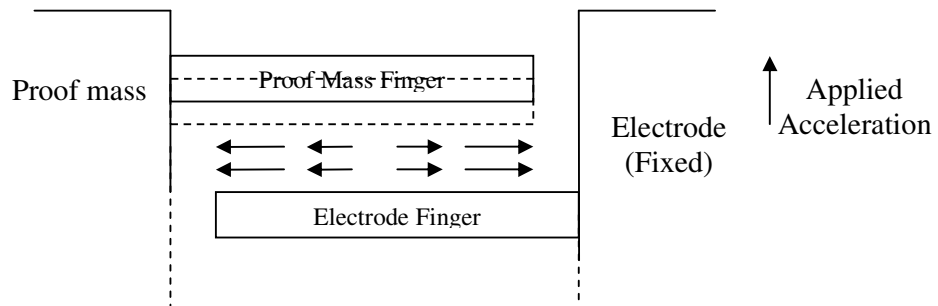


Figure 20: Illustration of squeeze film damping between the fingers.

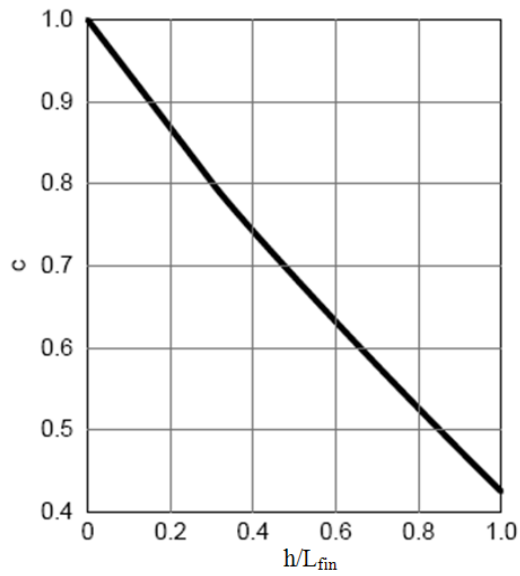


Figure 21: Relation between the factor ‘ c ’ and ‘ h/L_{fin} ’.

When Couette flow and squeeze film damping are both considered, total damping of the accelerometer can be calculated as follows:

$$B_{total} = B_{couette} + B_{squeeze} \quad (20)$$

For a typical accelerometer studied in this thesis study, if Couette and squeeze film damping are calculated separately, it will be seen that Couette damping (7.45×10^{-6}) is too small compared to squeeze film damping (2.71×10^{-3}). Therefore, Couette damping can be ignored in damping calculations.

3.1.1.3 Spring Constant

Capacitive MEMS accelerometers contain spring shaped parts that connect the proof mass to the substrate. Folded beam structure is the generally used spring structure for capacitive accelerometers. Folded beam structure is shown in Figure 22. Spring constant of folded beam structure depends on structural thickness and folded beam dimensions [35, 37].

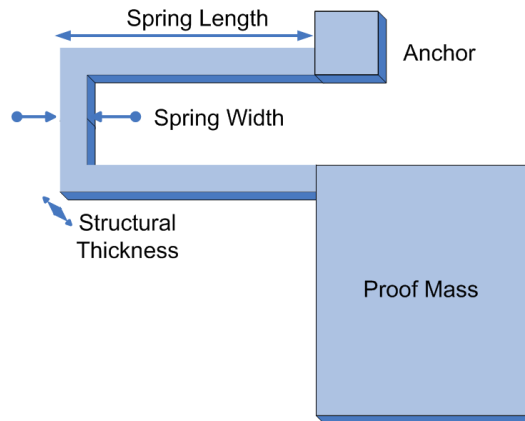


Figure 22: Folded beam spring illustration.

The spring constant obtained from this folded beam structure can be calculated with Equation (21) [34].

$$k = \left[\frac{EhW_{spr}^3}{L_{spr}^3} \right] \quad (21)$$

where, E is the Young's modulus, h is the structural thickness, W_{spr} is the spring width, and L_{spr} is the spring length.

The spring structure can be designed as doubly folded manner in order to increase the spring constant. Also, spring constant can be increased by increasing the number of spring shaped structures of the accelerometer. In these cases, to calculate the spring constant a topological spring constant coefficient is used as a multiplier as shown in Equation (22).

$$k = c_{topological} \frac{EhW_{spr}^3}{L_{spr}^3} \quad (22)$$

where, $c_{topological}$ is the topological spring constant depending on the number of beams used and beam design whether folded or doubly folded.

In sections 3.1.1.1, 3.1.1.2, 3.1.1.3; mass, spring, and damping calculations are explained. After calculating mass, spring, and damping values; the second order transfer function of the accelerometer giving the input output relation between the displacement and applied acceleration is constructed. The next step should be the conversion of this displacement into capacitance change. In the next section the block converting the displacement into capacitance change will be explained.

3.1.2 Accelerometer Displacement to Capacitance Change Block

Capacitive MEMS accelerometers convert acceleration into capacitance change. In Section 3.1.1, acceleration to proof mass displacement transfer function is obtained and in this section, displacement to capacitance change block of the Matlab-SIMULINK model will be described.

Illustration of capacitive MEMS accelerometer dimensions, rest capacitance value of the accelerometer, and capacitance change due to displacement of proof mass under acceleration are described in Section 2.1. As it is mentioned in Section 2.1, the capacitance value of the accelerometer for displacement of 'x' under acceleration can be calculated with Equation (23).

$$C_{1,2} = \frac{N\epsilon_0 h L_{finoverlap}}{d_1 \mp x} + \frac{(N-1)\epsilon_0 h L_{finoverlap}}{d_2 \pm x} \quad (23)$$

where, N is the number of fingers per side, h is the structural thickness, $L_{finoverlap}$ is the fingers overlapping length, d_1 and d_2 are finger spacings, x is the proof mass displacement, and ϵ_0 is the permittivity of air. Using Equation (23) two function blocks to calculate left and right side capacitances of the accelerometer are utilized in the Matlab-Simulink model. Then, the difference of the left and right side capacitances is taken.

To sum up, capacitive MEMS accelerometer is modelled with a second order transfer function followed by displacement to capacitance change function blocks. The capacitive accelerometer model outputting capacitance change is given in Figure 23.

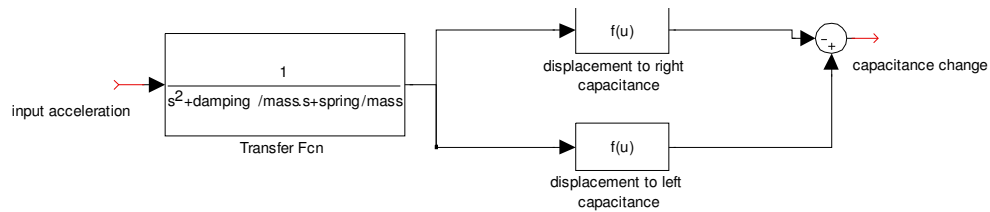


Figure 23: Capacitive MEMS accelerometer Matlab-Simulink model.

Capacitive MEMS accelerometer model is followed by the model constructed for the sigma-delta type readout circuit. Next section gives the Simulink model proposed for the sigma-delta readout circuit.

3.2 Sigma-Delta Readout Circuit Model

The theory of the sigma-delta modulation is explained in Section 2.2.1. As it is mentioned in Section 2.2.1, sigma-delta type readout circuit is suitable for navigation purpose accelerometer since it provides low noise and small bandwidth. Sigma-delta type readout circuit converts capacitance change output of both sides of the accelerometer into voltage and compares them to provide an oversampled single-bit output and force-feedback to the accelerometer. Combined with the capacitive MEMS accelerometer the readout circuit forms an electromechanical sigma-delta system as shown in Figure 24.

The structure of the readout circuit used in this thesis study is shown in Figure 25. [35]. The readout circuit has two phases; sensing phase and feedback phase which are controlled by the switches. At each clock cycle a sensing and a feedback phase is completed by the readout circuit.

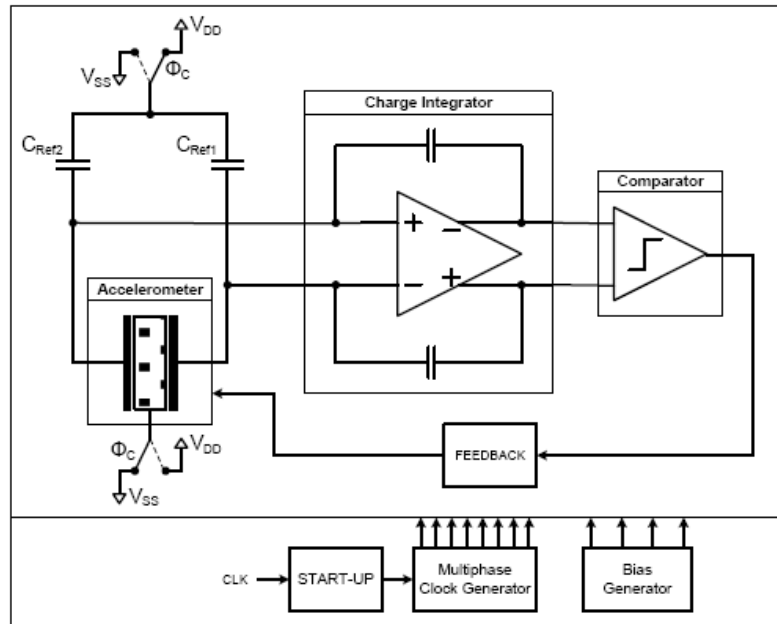


Figure 24: Electromechanical sigma-delta readout circuit [35].

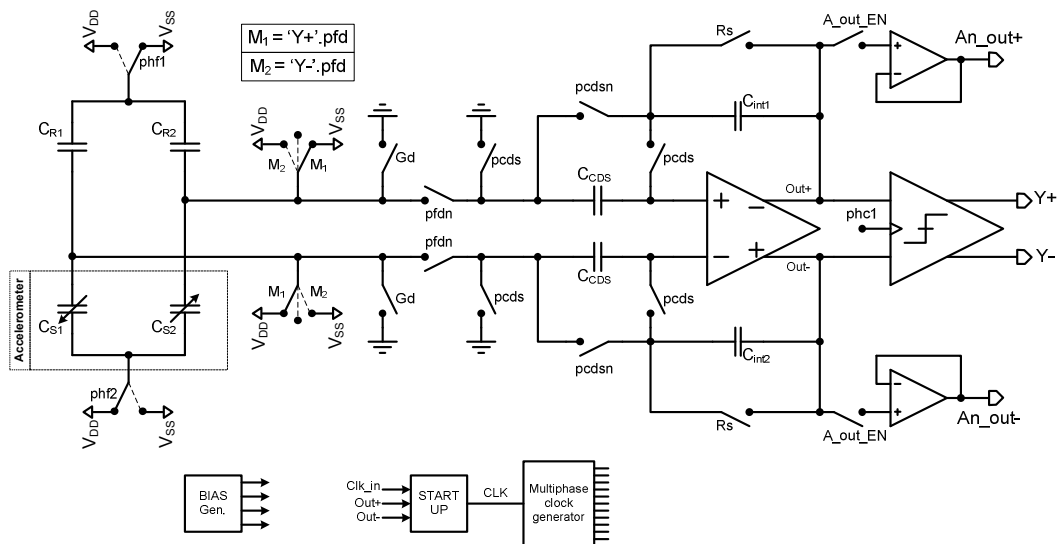


Figure 25: Structure of the readout circuit [35].

At sensing phase the charge difference generated by the capacitance change is transferred to the charge integrator and voltages at the output of the charge integrator is compared by a comparator. After the comparator output is generated, the circuit gets into feedback phase by disconnecting the charge integrator from the accelerometer. Therefore, while modelling the readout circuit, two main blocks are taken into account; the sensing part and the feedback part.

The sensing part of the readout circuit model includes charge integrator and comparator blocks. The charge integrator part of the readout circuit is modelled with a gain block which converts capacitance change of the accelerometer into voltage. The gain value of the gain block depends on the value of the integration capacitance. To send the voltage value to the comparator at each clock cycle a zero-order-hold block is used in the model. The comparator is used to compare the capacitance change of the right side and left side of the accelerometer which will give information about the direction of the applied acceleration and hence the direction of the feedback force. The output of the comparator is the oversampled 1-bit output of the readout circuit.

The feedback part of the readout circuit model is based on the feedback force applied to the accelerometer. Feedback is generated by applying a DC voltage to the proof mass of the accelerometer using the switches constructed in the readout circuit. While one of the electrodes is set to +2.5V and the other electrode is set to -2.5V, the proof mass is set to either +2.5V or -2.5V depending on the comparator output. Hence the potential difference between the proof mass and one of the electrodes is 5V and the other electrode is 0V resulting in an electrostatic force between the proof mass and one of the electrodes in the opposite direction of the applied acceleration. The feedback force depends on the sensitivity of the accelerometer. Sensitivity of the accelerometer can be calculated by taking the derivative of the capacitance formula given in Equation (23). Equation (24) gives the sensitivity of an accelerometer.

$$\frac{\partial C_{1,2}}{\partial x} = \frac{N\epsilon_0 h L_{finoverlap}}{(d_1 \mp x)^2} - \frac{(N-1)\epsilon_0 h L_{finoverlap}}{(d_2 \pm x)^2} \quad (24)$$

where, N is the number of fingers per side, h is the structural thickness, $L_{finoverlap}$ is the fingers overlapping length, d_1 and d_2 are finger spacings, x is the proof mass displacement, and ϵ_0 is the permittivity of air. The feedback force can be calculated with the equation given in Equation (25).

$$F = \frac{1}{2} \frac{\partial C}{\partial x} V^2 \quad (25)$$

where, V is the potential difference between the proof mass and the electrode. This feedback force tries to keep the proof mass at its null position. The comparator output is used to control a switch to apply the obtained force from either +2.5V or -2.5V proof mass voltage. The feedback force is applied at 60% duty cycle of the clock, so a pulse generator is used in the model to apply feedback at 60% of the clock. The feedback force is converted into acceleration by dividing the force by mass and feedback acceleration is given as an input acceleration to the accelerometer. This feedback acceleration will complete the closed loop system.

The model proposed in Matlab-Simulink for the readout circuit is shown in Figure 26.

The comparator output of the sigma-delta readout circuit is an oversampled 1-bit data which needs to be filtered to reduce the data rate and to convert 1-bit data into meaningful digital data. Therefore, there is a need for a filter to process the output of the comparator which is described in detail in the next section.

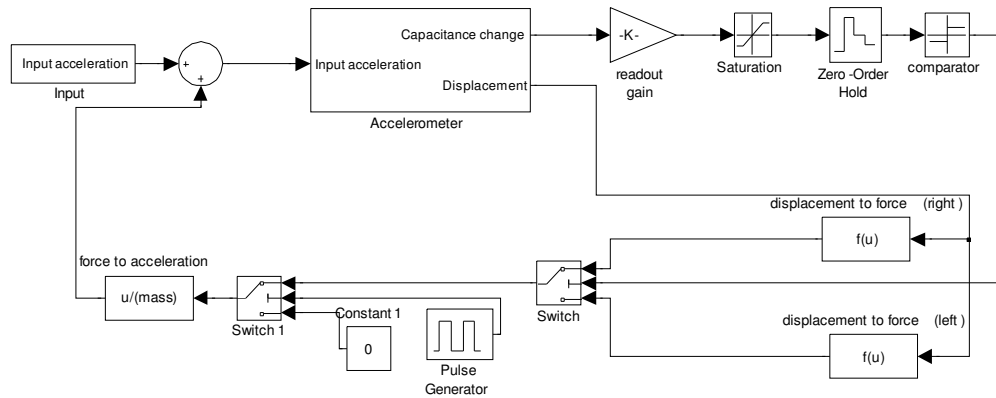


Figure 26: Electromechanical sigma-delta readout Matlab-Simulink model.

3.3 Decimation Filter Model

In this thesis study, Sinc filters are used as decimation filter to get rid of the redundant data and filter out the high frequency noise of the readout circuit single-bit output as described in Section 2.3. The decimation filter designed in this study is a 2 stage cascaded decimation filter. The order of the electromechanical sigma-delta system used in this study is 2, so the order of the Sinc filter must be at least 3. Therefore, a 3rd order Sinc filter is used in the first stage of the filter and in the second stage a 2nd order Sinc filter is used in order to filter the noise more. As it is mentioned in Section 2.3, Sinc filters are composed of addition and subtraction blocks whose transfer functions are given in Equation (5) and Equation (6). The Simulink model of the cascaded decimation filter is proposed using these transfer functions. The model of 3rd order Sinc filter is shown in Figure 27. The input bitsream is a 1-bit 500 kHz digital data coming from the comparator output of the readout circuit. N_1 is taken as 40 and therefore the output of the 3rd order decimation filter is a number which can be expressed as 16-bit digital value (calculated with

Equation (7)). Output of the 3rd order decimation filter is send to the cascaded 2nd order decimation filter. The model of 2nd order Sinc filter is shown in Figure 28.

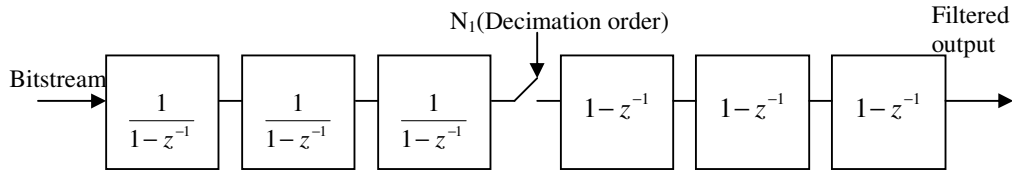


Figure 27: Sinc³ filter model.

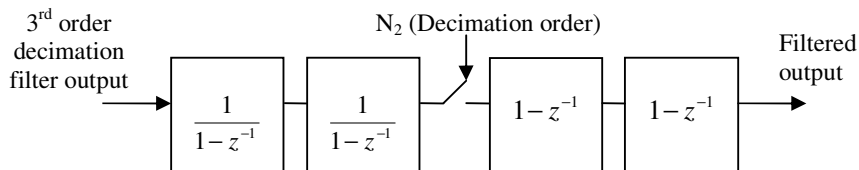


Figure 28: Sinc² filter model.

Here, N_2 is taken as 16; therefore the output of the 2nd order decimation filter is a number which can be expressed as a 24-bit digital value (calculated with Equation (7)). The output of the decimation filter is then calibrated to obtain an output in terms of acceleration.

The cascaded decimation filter is modelled in Matlab-Simulink as shown in Figure 29. The switches of decimation filter are realized with zero-order-hold blocks, sampling frequencies of which are set depending on the decimation orders. The output of the decimation filter is then calibrated by software to convert the output of the filter into acceleration units.

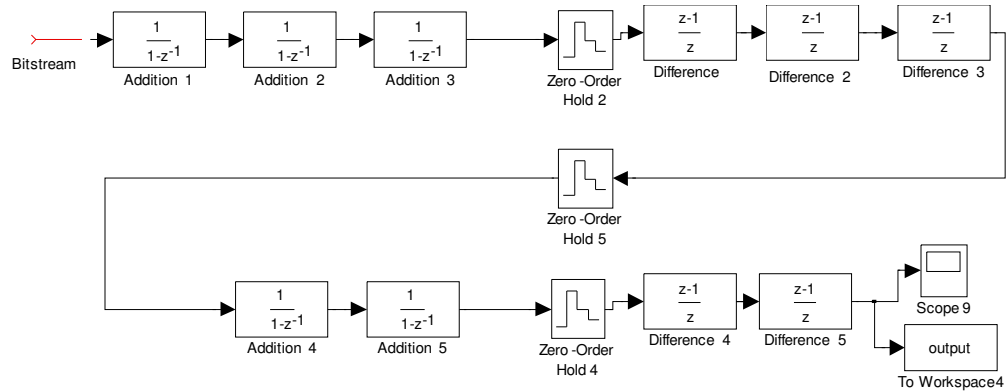


Figure 29: Cascaded decimation filter Matlab-Simulink model.

In this section the model proposed for decimation filter is described in detail. In the next section, the noise sources added to the accelerometer system model will be described.

3.4 Modeling the Noise Sources

There are mechanical and electrical noise sources of capacitive accelerometers which are listed and described in Section 2.4. The basic noise sources of a capacitive MEMS accelerometer system are Brownian noise, amplifier noise, kT/C noise, quantization noise, and mass residual motion noise [36] as mentioned in Section 2.4. Each individual noise is calculated with the formula given in Table 2 and added to the related parts of the model as shown in Figure 30.

Brownian Noise: Brownian noise is due to the thermal motion of the proof mass, and it can be represented as a white noise since f_s is much greater than the accelerometer bandwidth. This noise is added to the model as an input noise source in terms of acceleration (Figure 30).

Table 2: Capacitive accelerometer system noise sources.

Brownian Noise	$a_n^2 = \frac{4k_b T b}{9.81^2 m^2}$
Amplifier Noise	$V_{out_thermal} = \sqrt{\frac{16 C_s + C_p}{3} \frac{k_b T}{C_{int} C_{out} f_s}}$
kT/C Noise	$V_{out_kT/C} = \sqrt{\frac{4k_b T}{f_s C_{int}}}$
Quantization Noise	$Quantization_noise = e_{rms} \frac{\Pi^n}{M^{n+0.5} \sqrt{2n+1}}$
Mass Residual Motion Noise	$N_{rm} = 4 \frac{f_{BW}}{f_s} \left(\frac{K}{M} \right) \frac{a_{fb}}{(2\pi f_s / 4)^2}$

Amplifier Noise: Amplifier noise is related with the thermal and flicker noise of the main amplifier utilized in the front-end readout. In general, flicker noise is cancelled out by using correlated double sampling (CDS), and therefore this noise source is represented as a band-limited white noise at the output of readout gain block (Figure 30).

kT/C Noise: kT/C noise is a thermal noise due to the switched-capacitor nature of the readout electronics, and mostly depends on the integration capacitance and the sampling frequency. This noise source is represented at the output of the gain block as a white noise (Figure 30).

Quantization Noise: Quantization noise is effective under closed loop operation, and it is one of the dominant noise sources in the system. This noise source is generated during the analog-to-digital conversion and dominantly depends on the oversampling ratio. The quantization error is assumed to be input independent, uniformly distributed, and independent identically distributed and therefore modeled as a white noise source [29] (Figure 30).

Mass Residual Motion Noise: Mass residual motion is one of the most dominant noise sources especially at low oversampling ratios. In closed loop operation, the pulse train output of the Σ - Δ readout is given as feedback to the proof mass, and this results in the oscillation of it around its equilibrium position. This oscillation exists even at zero input acceleration, and it is taken into account as a noise source and added to the model as shown in Figure 30.

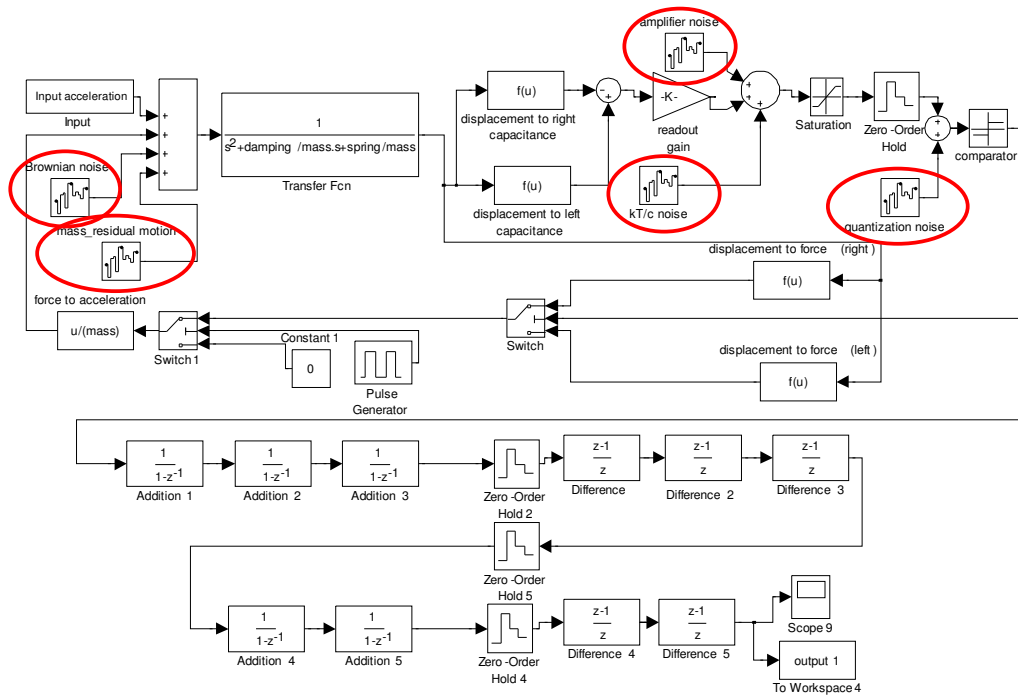


Figure 30: Noise sources added to the accelerometer system model.

In this section, accelerometer noise sources, how they are modeled, and how they are added to the system model are described. In the following section, the system level model of the accelerometer system and user interface designed for the model will be explained.

3.5 Capacitive Sigma-Delta MEMS Accelerometer System Model and Designed User Interface

In the previous sections, the accelerometer system model is described part by part. In this section, whole accelerometer system model is given. System level model of the accelerometer is proposed in MATLAB-SIMULINK environment by combining the models explained in previous sections. The model is designed such that it can be adapted to different accelerometer, readout and decimation filter designs. The accelerometer system design can be changed with the user interface generated within this thesis study. The user interface allows changing the design parameters such as capacitive MEMS accelerometer all dimensions, readout circuit gain, environment temperature, decimation order etc.

The proposed model is used to estimate system level performance of different accelerometer system designs. The effect of design parameters on overall performance can be observed with this model which allows the user to change critical design parameters.

The critical design parameters of the MEMS accelerometer are proof mass width, proof mass length, structural thickness, number of fingers, finger width finger length, distance between fingers, spring width, spring length, topological spring constant and overlapping finger length. Each of these dimensions has different effects on system performance and this model give the chance of analyzing these effects. All of these critical parameters are set as variables that can be changed by the user.

There are also some critical parameters of the readout circuit such as the readout gain, sampling frequency and integration capacitance which affects the system performance. These parameters are also set changeable so that the user can see the effect of readout parameters on the overall system performance.

Lastly, the design parameters of decimation filter affecting the accelerometer system output are defined changeable. Decimation order of the decimation filter which is the most important parameter of the signal processing part is made changeable.

Besides these accelerometer system critical design parameters, also the temperature and input acceleration applied to the model can be changed with the user interface. The input acceleration can be a step or a sine or a square acceleration depending on the user choice.

After the user's entering all changeable design parameters, simulations are performed. The user interface outputs some performance parameters of the designed accelerometer system according to the performed simulation. These parameters can be listed as the designed accelerometer proof mass, spring constant, damping, range, noise values and bias and scale factor values calculated with the input-output relation are given as output of the model. User interface also gives input-output graphs of the performed simulation

The whole accelerometer system model and designed user interface are shown in Figure 31 and Figure 32 respectively.

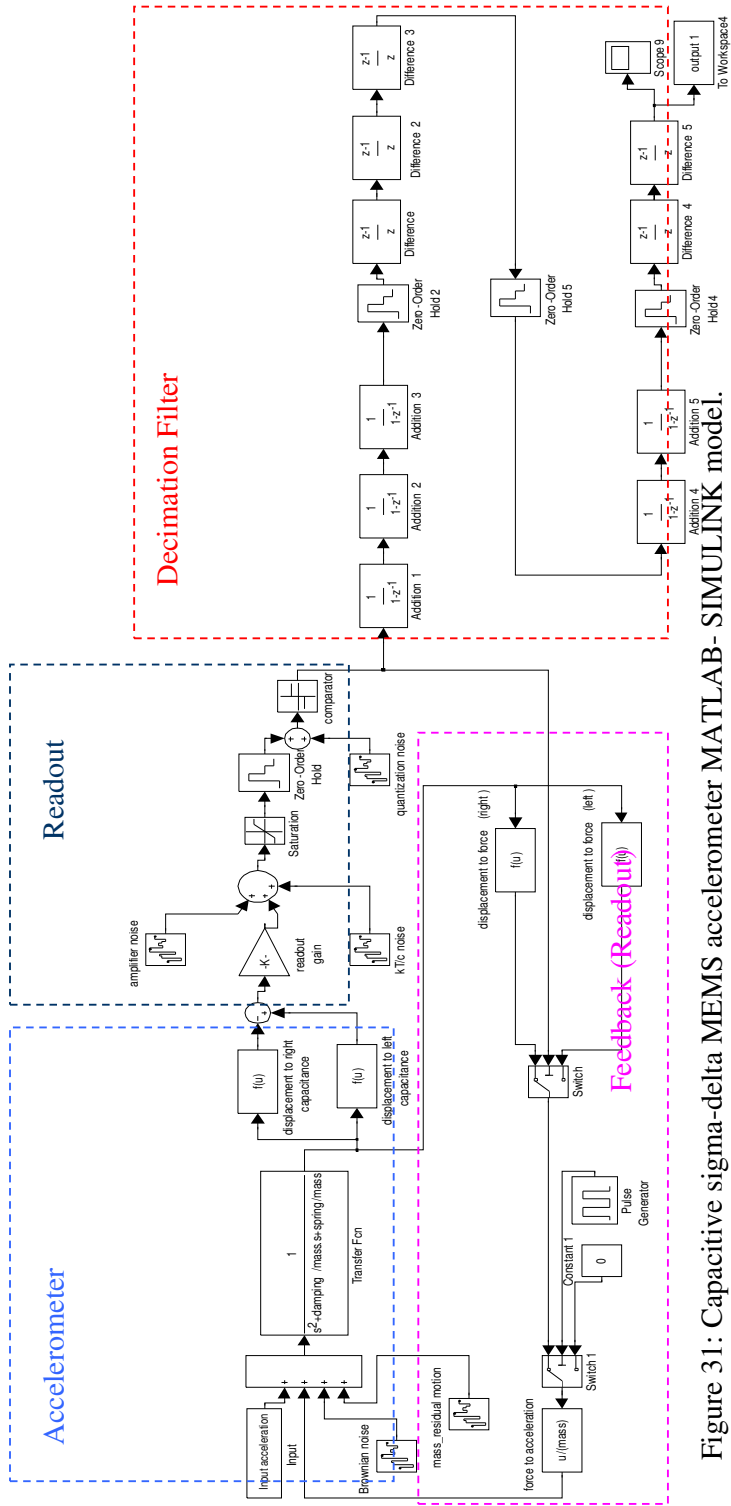


Figure 31: Capacitive sigma-delta MEMS accelerometer MATLAB- SIMULINK model.

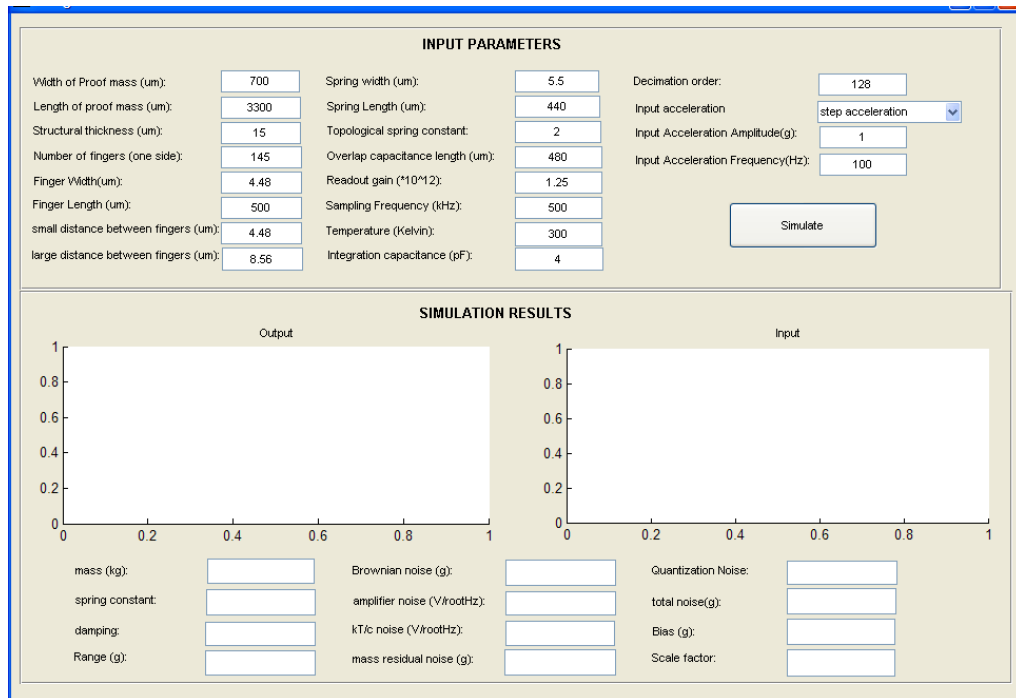


Figure 32: Accelerometer model user interface.

In this chapter, the proposed system level model of a capacitive sigma-delta MEMS accelerometer system is presented. All the parts of the accelerometer system and how they are modeled are explained in detail. Also, the user interface allowing the user to change critical system parameters of the system is represented and explained. In the next chapter, the simulations done with this model and their comparison with test results are given.

CHAPTER 4

ACCELEROMETER SYSTEM SIMULATION AND TEST RESULTS

CHAPTER 3 gives the detailed MATLAB-SIMULINK model for a capacitive sigma-delta MEMS accelerometer system. In this chapter, this model's functionality will be verified with simulations and test results. For this reason, two accelerometer systems composed of MEMS accelerometer, sigma-delta readout electronics, and decimation filter are implemented, tested, and compared with the simulation results of these accelerometer system models.

Basically, simulations and tests are compared in terms of noise parameters and overall system performance. In order to make these comparisons, a series of simulations and tests are performed which can be listed as 12-position acceleration, clock frequency effect on output noise, integration capacitance effect on output noise, decimation order effect on output noise, and operational range simulations and tests. In the first section of this chapter, the accelerometer systems implemented within this thesis study are explained in detail and in the next section; simulations and test results of these accelerometers are given.

4.1 Implemented Accelerometer Systems

Two accelerometer systems consisting capacitive MEMS accelerometer, CMOS readout electronics and decimation filter are used in this thesis study for verification of the accelerometer system model. Our group (METU-MEMS) has already been implementing capacitive MEMS accelerometers and CMOS readout circuits; in this

study system level integration of the accelerometer and system level tests of the accelerometer are done.

The two accelerometer systems used in this study differ in the structure of the MEMS accelerometer part which affects the performance of the systems. The model proposed in MATLAB-SIMULINK is verified through test results of these accelerometer systems. The capacitive MEMS accelerometers are implemented with Dissolved Wafer Process (DWP), the readout electronics is implemented using XFab 0.6 μm CMOS process, and decimation filter is implemented with software on a PIC.

4.1.1 Fabricated MEMS Accelerometers

Two MEMS accelerometers (named as “DWP-1” and “DWP-2”) having different structures are fabricated within this study in order to verify the proposed model. The capacitive MEMS accelerometers are fabricated using Dissolved Wafer Process since it is the most used accelerometer fabrication process in our group. The accelerometers are fabricated using 3 masks and the fabrication process is given in Figure 33. Firstly, a glass substrate is etched to generate anchors as shown in Figure 33(a), then chromium and gold is sputtered on this glass substrate to generate electrical connections (Figure 33(b)). Then a silicon wafer is Boron doped as shown in Figure 33(c) about 15 μm which defines the structural thickness of the accelerometer and the Boron doped silicon is etched according to the structure of the accelerometer (Figure 33(d)). Then the silicon wafer and glass substrate are bonded anodically (Figure 33(e)) and the undoped silicon is etched (Figure 33(f)). This fabrication process is developed by Dr. Said Emre Alper at METU-MEMS Research and Application Center. The accelerometers used in the tests were fabricated by İlker Ender Ocak.

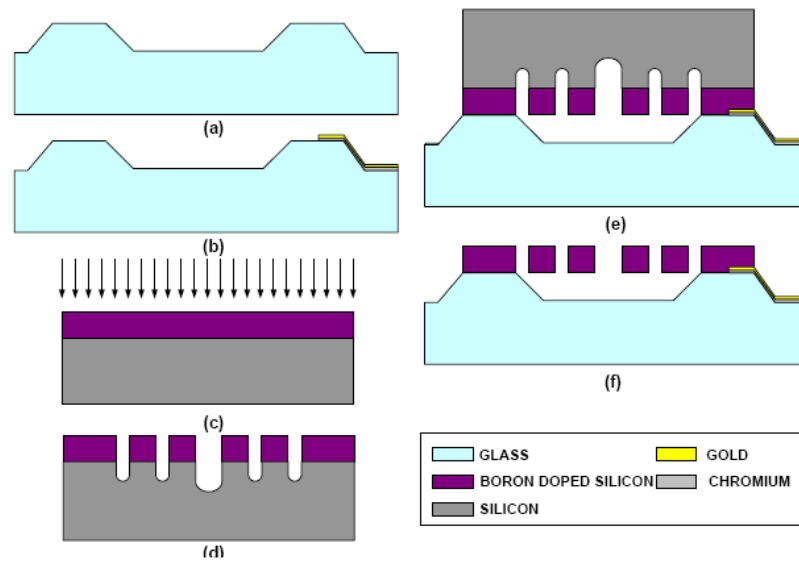


Figure 33: Fabrication process of DWP accelerometers [46].

The accelerometer masks are prepared depending on the designed accelerometers. The dimensions of the first accelerometer (DWP-1) which are used in fabrication process are given in Table 3.

DWP-1 accelerometer has the structure shown in Figure 34. It has 6 doubly folded springs, four of which are placed at the corners and the remaining two are at the center. Fingers are placed on both sides of the accelerometer. Three connections which are from the electrodes and the proof mass are taken out to read the capacitance change occurred due to acceleration. This structure looks like the conventional capacitive accelerometer except the springs located at the center of the proof mass used to avoid proof mass buckling due to small structural thickness. However, these springs will increase the spring constant and therefore will increase the overall noise of the system.

Table 3: DWP-1 accelerometer dimensions.

Proof mass width	1620 μm
Proof mass length	3200 μm
Structural thickness	15 μm
Number of fingers per side	168
Finger width	7 μm
Finger length	450 μm
Small distance between fingers	1 μm
Large distance between fingers	4 μm
Spring width	7 μm
Spring length	548 μm
$K_{\text{topological}}$ (Topological spring constant)	6
$L_{\text{finoverlap}}$ (Finger overlap length)	440 μm

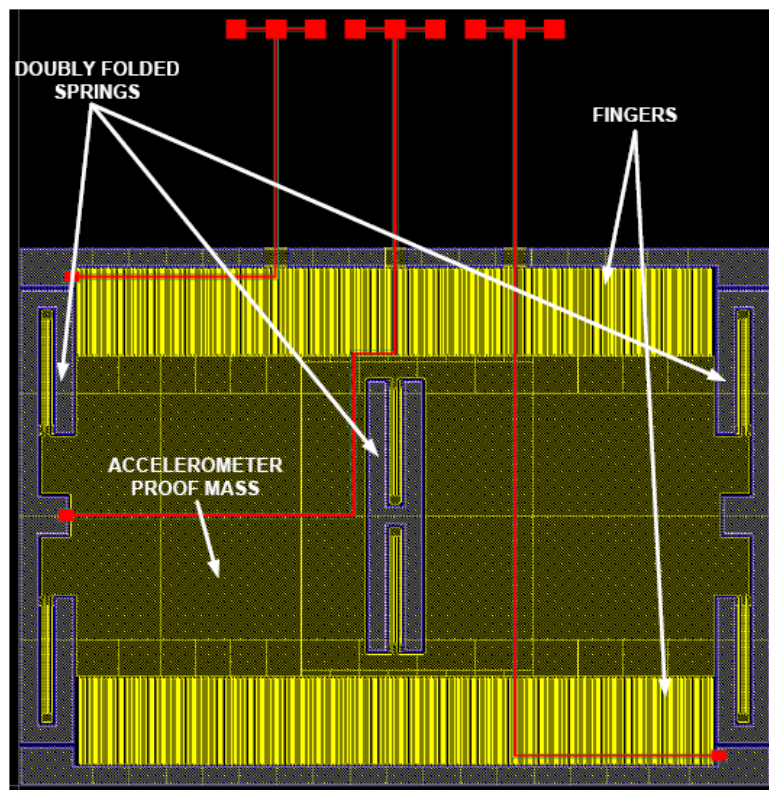


Figure 34: Layout of DWP-1 accelerometer.

The second accelerometer (DWP-2) fabricated for this study has a different structure from the DWP-1 accelerometer. DWP-1 accelerometer suffers from its very long and very thin fingers which buckle after fabrication that affects the system performance. Therefore, a new design trying to solve this problem is necessary. DWP-2 accelerometer has shorter fingers than DWP-1 accelerometer to avoid fingers buckling. Here, shorter fingers cause loss of resolution; to overcome this problem number of fingers should be increased. In order to increase finger numbers, new finger pairs are placed at the center of the proof mass as shown in Figure 35. The DWP-2 accelerometer has 6 doubly folded springs, four of which are placed at the corners and the remaining two are at the center like DWP-1 accelerometer. DWP-2 accelerometer has the structure shown in Figure 35.

The dimensions of the second accelerometer (DWP-2) which are used in fabrication process are given in Table 4. The masks needed to fabricate this accelerometer are prepared according to these dimensions.

Table 4: DWP-2 accelerometer dimensions.

Proof mass	$1.45 \cdot 10^{-7}$ kg
Structural thickness	13.5 μm
Number of fingers per side	424
Finger width	7 μm
Finger length	150 μm
Small distance between fingers	1 μm
Large distance between fingers	4 μm
Spring width	7 μm
Spring length	550 μm
$K_{\text{topological}}$ (Topological spring constant)	6
$L_{\text{finoverlap}}$ (Finger overlap length)	140 μm

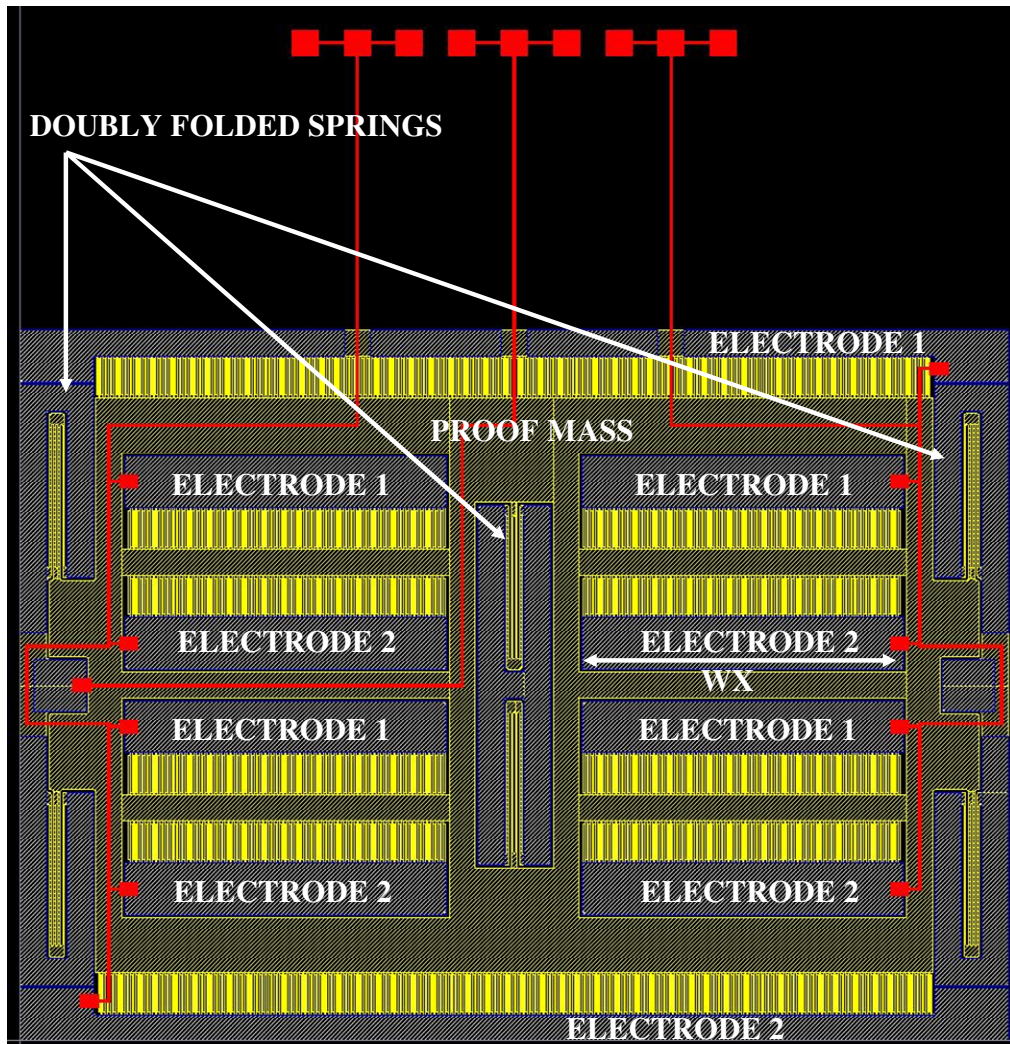


Figure 35: Layout of DWP-2 accelerometer.

4.1.2 Implemented Readout Electronics

Accelerometer part provides differential capacitance change which is usually in the range of tens of atto-farads, and this change should be sensed by a special electronic circuitry. Among various techniques for sensing such small capacitance difference,

Σ - Δ modulation is generally preferred because of its force feedback structure and inherent analog-to-digital conversion providing linearity and large operating range. The readout circuit used in this study is explained in Section 3.2 in detail.

The readout electronics is implemented using XFab 0.6 μm CMOS process. The design of the readout circuit is originally done by Reha Kepenek. The designed readout electronics is composed of switch capacitor network, charge integrator, comparator, and clock generator as described in Section 3.2. The implemented readout electronics is shown in Figure 36. The sigma-delta readout circuit is specially designed such that it can work both with internal or external clock, it can work at different sampling frequencies in external clock operation, its integration capacitance (C_{int}) can be changed between 0 pF to 15pF values, and it can work both in open loop and closed loop modes. These changeable parameters are changed with the related pads connection to either HIGH or LOW.

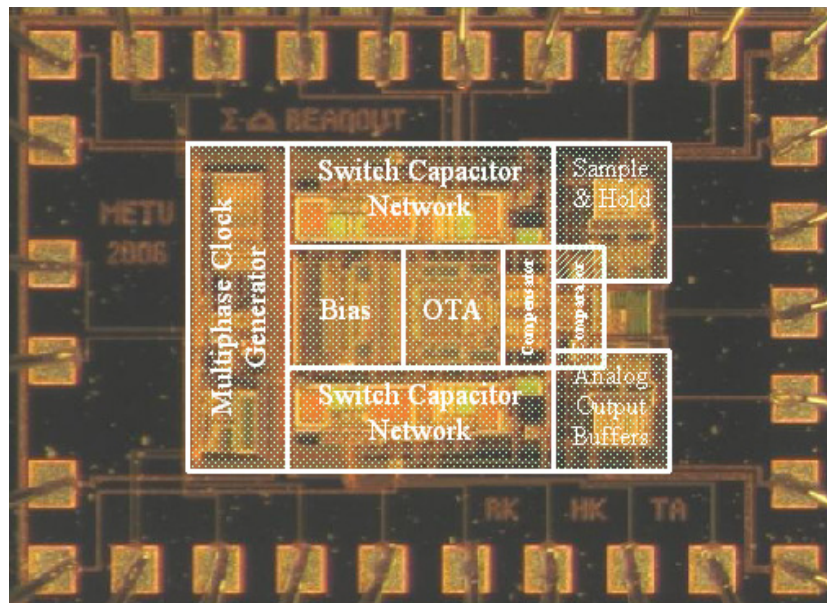


Figure 36: CMOS readout electronics.

The readout circuit used in DWP-1 accelerometer system can operate upto 750 kHz clock frequency and further increase in clock frequency generates problems in switching. Also it has a temperature dependent output. The problems in this readout circuit are solved with some minor changes in the readout circuit which allows clock frequencies upto 1MHz and provides temperature independent operation. This new version of the readout circuit is also designed by Reha Kepenek.

The fabricated MEMS accelerometer and CMOS readout circuit are bonded together as shown in Figure 37 to be able to make system level tests. The output is then processed by the decimation filter described in the next section.

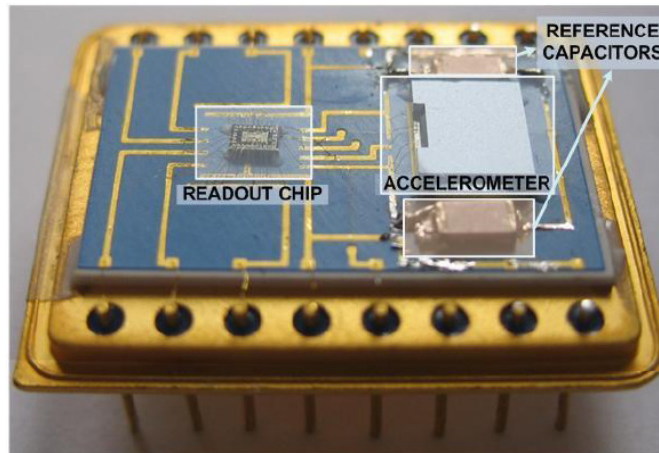


Figure 37: Fabricated MEMS accelerometer and readout circuit bonded together.

4.1.3 Implemented Decimation Filter

The structure of the decimation filter used in this study to process the oversampled bitstream output of the readout electronics is described in Section 3.3 in detail. Decimation filter is software implemented on a signal processing card. The filter

cascaded Sinc³ and Sinc² filter is realized software on a FPGA placed on the signal processing card. The filter takes bitstream output of the readout circuit passes it through the addition and subtraction blocks implemented on FPGA. The output of the filter is saved to a compact flash placed on the signal processing card and then calibrated to obtain the accelerometer output in terms of acceleration. In order to see the effect of decimation order on the system performance, the decimation order of the Sinc³ filter is set as a variable that can be changed.

In sections 4.1.1, 4.1.2, and 4.1.3, the fabricated accelerometer systems are described in detail. In the next section, the tests and simulations of these accelerometer systems will be described and comparison of simulations and test results will be given. Also, these accelerometer systems are analyzed in terms of noise parameters.

4.2 Accelerometer Systems Simulation and Test Results

This section gives detailed simulations and test results of the fabricated accelerometer systems described in Section 4.1. These results are compared with each other in terms of noise parameters to see how the model estimates the designed accelerometer performance parameters.

The simulations of DWP-1 and DWP-2 accelerometers are performed using the parameters exactly same with the implemented accelerometer systems. All of the parameters used in the simulations (same with the implemented accelerometer system) of DWP-1 and DWP-2 accelerometers are given in Table 5 and Table 6 respectively. The parameter values with ‘changeable’ statement can be changed and set to different values with related pads of the readout circuit.

Table 5: Accelerometer system parameters used for simulations of DWP-1.

Accelerometer	
Proof mass width	1620 μm
Proof mass length	3200 μm
Structural thickness	15 μm
Number of fingers per side	168
Finger width	7 μm
Finger length	450 μm
Small distance between fingers	1 μm
Large distance between fingers	4 μm
Spring width	7 μm
Spring length	548 μm
$K_{\text{topological}}$ (Topological spring constant)	6
$L_{\text{finoverlap}}$ (Finger overlap length)	440 μm
Readout Circuit	
Clock frequency (Sampling frequency)	500 kHz (changeable)
Integration capacitance	2 pF (changeable)
Temperature	300 Kelvin (room temperature)
Decimation Filter	
Decimation order for Sinc ³ filter	40 (changeable)
Decimation order for Sinc ² filter	16

Table 6: Accelerometer system parameters used for simulations of DWP-2
(continues on next page).

Accelerometer	
Proof mass	$1.45 \cdot 10^{-7}$ kg
Structural thickness	13.5 μm
Number of fingers per side	424
Finger width	7 μm
Finger length	150 μm
Small distance between fingers	1 μm
Large distance between fingers	4 μm
Spring width	7 μm
Spring length	550 μm
$K_{\text{topological}}$ (Topological spring constant)	6
$L_{\text{finoverlap}}$ (Finger overlap length)	140 μm
Readout Circuit	

Clock frequency (Sampling frequency)	500 kHz (changeable)
Integration capacitance	2 pF (changeable)
Temperature	300 Kelvin (room temperature)
Decimation Filter	
Decimation order for Sinc ³ filter	40 (changeable)
Decimation order for Sinc ² filter	16

In the first part of this section, 12 position acceleration simulations and test results of these accelerometers are compared. Then, the effect of clock frequency at the output noise is analyzed with both simulation and tests. The effect of integration capacitance at the output noise is also observed which gives information about the sensor charging reference noise. Then, the effect of decimation order on output noise is presented which gives information about the quantization noise of the system. Lastly, the operational range of these accelerometer systems is found with both simulations and tests.

4.2.1 12-Position Acceleration

12-position acceleration tests are performed to observe the functionality of an accelerometer system between -1g and +1g acceleration. The accelerometer is placed on a dividing head (index table) that rotates around the gravitational acceleration resulting in different acceleration application on the accelerometer as shown in Figure 38. The accelerometer is rotated and fixed at different angles and its output is saved at each angle to see the change at the output. At 12 different angles of index table, 12 different acceleration values are applied to the accelerometer. Figure 39 gives the illustration of these positions and corresponding acceleration values.

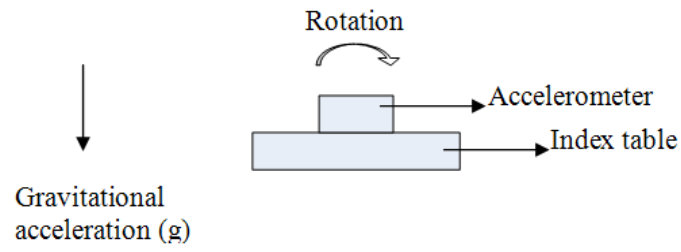


Figure 38: Accelerometer 12-position acceleration test placement.

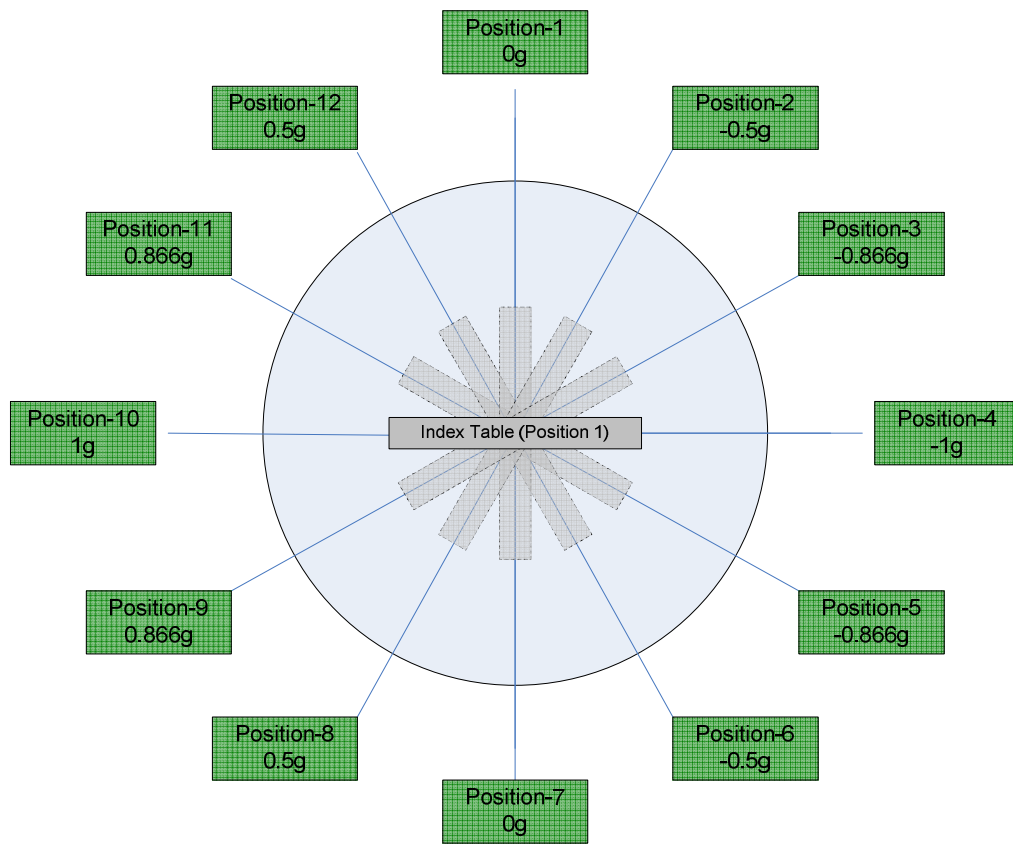


Figure 39: Illustration of 12-position acceleration.

The 12-position acceleration tests of the fabricated accelerometer systems are performed on an index table. The accelerometer and readout circuit is supplied with +15V from a power supply and the signal processing card (decimation filter) is supplied with +5V from a power supply. In normal working conditions of the accelerometer system, accelerometer and readout extracts totally 9mA current from the supply and the signal processing card extracts 187mA current from the supply. The accelerometer, readout and decimation filter parameters used in the tests of DWP-1 and DWP-2 accelerometers are given in Table 5 and Table 6 respectively. The test setup for 12-position acceleration tests is given in Figure 40. At each position, the accelerometer bitstream output is filtered with signal processing card and collected for 10 seconds at 800 Hz data rate to a memory. Within this test, the accelerometer works with the external clock generated in the signal processing card. The collected raw output data of the accelerometers are calibrated with a Matlab program to obtain output in terms of acceleration [47]. The calibrated peak-to-peak output noise is observed and then converted to $g/\sqrt{\text{Hz}}$ with Equation (26).

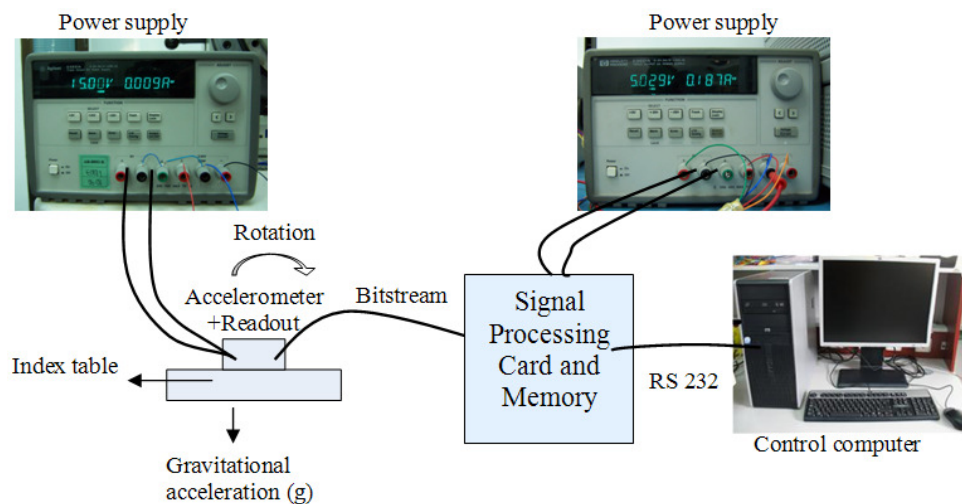


Figure 40: 12-position acceleration test set-up.

$$\frac{\text{Noise } g/\sqrt{\text{Hz}}}{\sqrt{\text{Hz}}} = \frac{\text{Noise } p-p}{6\sqrt{\text{Bandwidth}}} \quad (26)$$

where $\text{Noise}_{g/\sqrt{\text{Hz}}}$ is the noise in terms of ‘g/√Hz’, Noise_{p-p} is the accelerometer peak-to-peak noise in terms of ‘g’, and Bandwidth is accelerometer bandwidth [49-51].

12-position acceleration tests of DWP-1 and DWP-2 accelerometers are performed and test results are observed and compared with simulation results. The calibrated 12-position acceleration test result of DWP-1 accelerometer is given in Figure 41. From 12-position test, about 11 mg peak-to-peak noise is observed at the DWP-1 accelerometer output at 800 Hz data rate which corresponds to 58.7 μg/√Hz [49, 51]. The scale factor of the accelerometer system obtained from 12-position acceleration is 1.17×10^{-6} g/(Output units) which is used to convert raw data into acceleration in terms of ‘g’. The raw data is multiplied with this scale factor value to obtain output in terms of ‘g’ units.

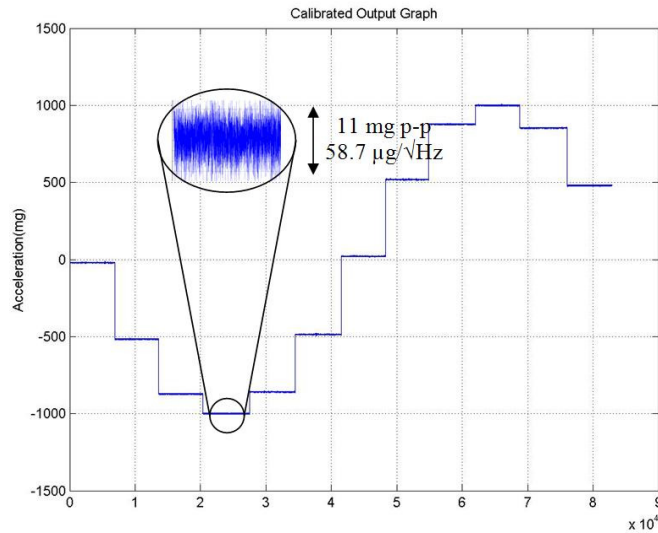


Figure 41: 12-position acceleration test result of DWP-1 accelerometer.

The DWP-1 accelerometer system model is proposed in MATLAB-SIMULINK as described in CHAPTER 3. The model is used to perform the simulations of the DWP-1 accelerometer system. 12-position acceleration simulations of the DWP-1 accelerometer system is done by applying step input for each position with corresponding acceleration magnitude to the model. Then the raw data obtained at the output of the decimation filter model is saved to a text file and again like in the case of 12-position test, the raw data is send to a calibration algorithm written in Matlab to obtain output of the model in terms of ‘g’ [48]. The calibrated output obtained from simulations is given in Figure 42. The peak to peak noise obtained from simulations is around 10 mg at 800 Hz data rate which corresponds to $53.3 \mu\text{g}/\sqrt{\text{Hz}}$. The scale factor of the accelerometer system obtained from 12-position acceleration simulation is $0.97 \times 10^{-6} \text{ g}/(\text{Output units})$ which is used to convert raw data into acceleration in terms of ‘g’. The raw data is multiplied with this scale factor value to obtain output in terms of ‘g’ units. As it can be seen from the noise values, simulations and test results are consistent in terms of noise parameters for 12-position acceleration.

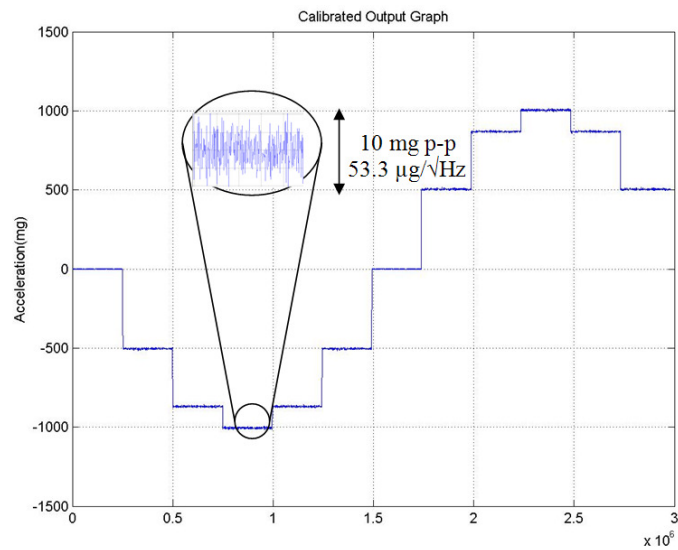


Figure 42: 12-position acceleration simulation result of DWP-1 accelerometer.

With the same approach, 12-position acceleration simulations and tests of the DWP-2 accelerometer are performed. 12-position acceleration test and simulation results are given in Figure 43 and Figure 44 respectively. From the test, 70 mg peak-to-peak noise corresponding to $373.3 \mu\text{g}/\sqrt{\text{Hz}}$ is obtained at 800 Hz data rate. Figure 43 shows the 12-position acceleration test of DWP-2 accelerometer. The scale factor of the DWP-2 accelerometer system obtained from 12-position acceleration test is $2.933 \times 10^{-6} \text{ g}/(\text{Output units})$ which is used to convert raw data into acceleration in terms of ‘g’. From the simulation, 60 mg peak-to-peak noise corresponding to $320.05 \mu\text{g}/\sqrt{\text{Hz}}$ is obtained at 800 Hz data rate. Figure 44 shows the 12-position acceleration simulation of DWP-2 accelerometer. The scale factor for DWP-2 accelerometer obtained from the simulations is $2.627 \times 10^{-6} \text{ g}/(\text{Output units})$.

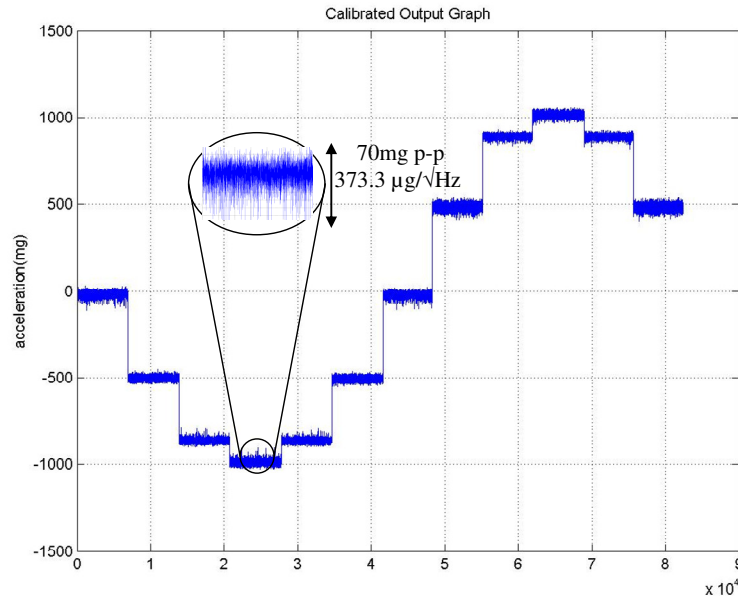


Figure 43: 12-position acceleration test result of DWP-2 accelerometer.

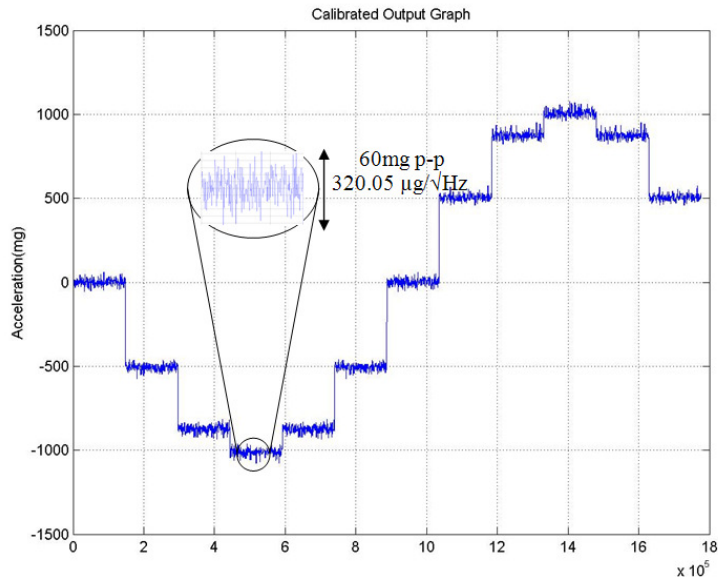


Figure 44: 12-position acceleration simulation result of DWP-2 accelerometer.

4.2.2 Clock Frequency Effect on the Output Noise

The accelerometer system has electrical and mechanical noise sources as described in Section 3.4. The most dominant noise sources among them are mass residual motion noise and quantization noise for the accelerometers analyzed within this thesis. The fabricated accelerometers have relatively small proof mass and large operational range which causes mass residual motion to be the most dominant noise source of the systems. This claim can be proved by observing the decrease at the output noise as clock frequency (sampling frequency) increases because if we look at the mass residual motion noise expression, we can see that it is inversely proportional to the square of the sampling frequency.

In this section, the fabricated accelerometer systems output noise dependency on clock frequency is observed with both simulations and tests. The simulations and tests are done using the same parameters, except the clock frequency, given in Table 5 and Table 6 for DWP-1 and DWP-2 accelerometers respectively. The clock frequency of DWP-1 is increased from 500 kHz to 750 kHz with 50 kHz increments and at each clock frequency value 12-position acceleration tests are performed as described in Section 4.2.1. The noise values obtained from 12-position acceleration test at each clock frequency is recorded and the change at the output noise is observed. Then simulations of the DWP-1 accelerometer system model are done for changing clock frequency. Again sampling frequency is increased from 500 kHz to 750 kHz with 50 kHz increments and at each clock frequency value, 12-position acceleration simulations are performed by applying step input having the corresponding position acceleration magnitude. The noise levels obtained with these simulations are observed to see the effect of clock frequency on the output noise. The output noise with respect to clock frequency obtained from simulation and test results are given in Table 7 and Figure 45 for DWP-1 accelerometer. As it can be seen from Figure 45, output noise decreases significantly with increasing clock frequency. The accelerometer output noise nearly halves as the clock frequency is increased which proves that the mass residual motion noise is the dominant noise source of the system because it is inversely proportional to the square of the sampling frequency. When the sampling frequency is increased further, mass residual motion becomes insignificant compared to other noise sources. The change in output noise gives us information about the mass residual motion noise. According to this approach mass residual motion noise is calculated using Equation (27) [49, 51] and found $46.4 \mu\text{g}/\sqrt{\text{Hz}}$ from simulation and $50.1 \mu\text{g}/\sqrt{\text{Hz}}$ from test results. The values of mass residual motion noise from simulation and test are close.

$$E^2_{total,rms} = E^2_{rms,mass_residual} + E^2_{rms,other_noises} \quad (27)$$

where $E_{total,rms}$ is the rms value of the total noise corresponding to the noise value obtained at clock frequency of 500 kHz, $E_{rms,mass_residual}$ is the rms value of the mass residual motion noise, and $E_{rms,other_noises}$ is the rms value of the other noises corresponding to the noise value obtained at clock frequency of 700 kHz.

Table 7: Effect of clock frequency on DWP-1 accelerometer output noise.

Clock Frequency	Noise Obtained From Simulation Results	Noise Obtained From Test Results
500 kHz	53.3 $\mu\text{g}/\sqrt{\text{Hz}}$	58.7 $\mu\text{g}/\sqrt{\text{Hz}}$
550 kHz	40.7 $\mu\text{g}/\sqrt{\text{Hz}}$	40.7 $\mu\text{g}/\sqrt{\text{Hz}}$
600 kHz	34.1 $\mu\text{g}/\sqrt{\text{Hz}}$	34.1 $\mu\text{g}/\sqrt{\text{Hz}}$
650 kHz	28.1 $\mu\text{g}/\sqrt{\text{Hz}}$	32.8 $\mu\text{g}/\sqrt{\text{Hz}}$
700 kHz	27.1 $\mu\text{g}/\sqrt{\text{Hz}}$	31.6 $\mu\text{g}/\sqrt{\text{Hz}}$
750 kHz	26.1 $\mu\text{g}/\sqrt{\text{Hz}}$	30.5 $\mu\text{g}/\sqrt{\text{Hz}}$

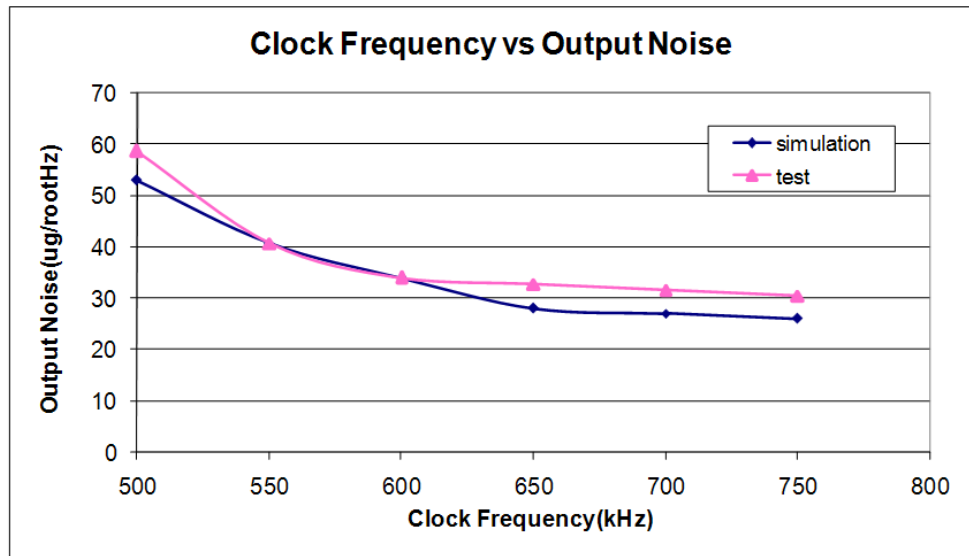


Figure 45: Clock frequency versus output noise graph obtained from simulation and test of DWP-1 accelerometer.

With the same approach, the output noise dependency on clock frequency for DWP-2 accelerometer is also observed to see the effect of mass residual motion noise at the total noise. Clock frequency of DWP-2 accelerometer is increased from 500kHz to 1MHz with 50kHz increments. Simulations and tests are performed for each clock frequency and the decrease at the output noise is analysed. Table 8 gives the obtained noise values; Figure 46 shows the clock frequency versus output noise obtained from simulation and test results for DWP-2 accelerometer. The change in output noise gives us information about the mass residual motion noise. According to this approach mass residual motion noise is calculated again using Equation (27) and found 302.12 $\mu\text{g}/\sqrt{\text{Hz}}$ from simulation and 338.02 $\mu\text{g}/\sqrt{\text{Hz}}$ from test results. The values of mass residual motion noise for DWP-2 accelerometer from simulation and test are close.

Table 8: Effect of clock frequency on DWP-2 accelerometer output noise.

Clock Frequency	Noise Obtained From Simulation Results	Noise Obtained From Test Results
500 kHz	320.05 $\mu\text{g}/\sqrt{\text{Hz}}$	373.3 $\mu\text{g}/\sqrt{\text{Hz}}$
550 kHz	254.3 $\mu\text{g}/\sqrt{\text{Hz}}$	305.17 $\mu\text{g}/\sqrt{\text{Hz}}$
600 kHz	219.14 $\mu\text{g}/\sqrt{\text{Hz}}$	243.4 $\mu\text{g}/\sqrt{\text{Hz}}$
650 kHz	187.16 $\mu\text{g}/\sqrt{\text{Hz}}$	210.55 $\mu\text{g}/\sqrt{\text{Hz}}$
700 kHz	157.81 $\mu\text{g}/\sqrt{\text{Hz}}$	180.3 $\mu\text{g}/\sqrt{\text{Hz}}$
750 kHz	130.68 $\mu\text{g}/\sqrt{\text{Hz}}$	209.1 $\mu\text{g}/\sqrt{\text{Hz}}$
800 kHz	126.49 $\mu\text{g}/\sqrt{\text{Hz}}$	189.7 $\mu\text{g}/\sqrt{\text{Hz}}$
850 kHz	122.72 $\mu\text{g}/\sqrt{\text{Hz}}$	163.62 $\mu\text{g}/\sqrt{\text{Hz}}$
900 kHz	111.31 $\mu\text{g}/\sqrt{\text{Hz}}$	159.02 $\mu\text{g}/\sqrt{\text{Hz}}$
950 kHz	108.35 $\mu\text{g}/\sqrt{\text{Hz}}$	162.52 $\mu\text{g}/\sqrt{\text{Hz}}$
1 MHz	105.6 $\mu\text{g}/\sqrt{\text{Hz}}$	158.4 $\mu\text{g}/\sqrt{\text{Hz}}$

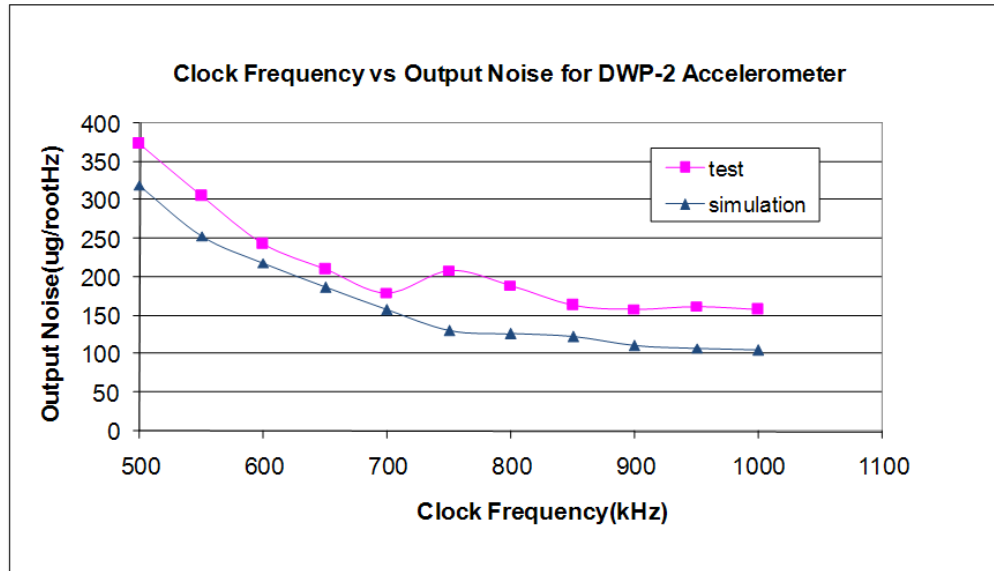


Figure 46: Clock frequency versus output noise graph obtained from simulation and test of DWP-2 accelerometer.

It is clear from Figure 45 and Figure 46 that the output noise of the accelerometers studied in this thesis can be significantly decreased by increasing clock frequency. The output noise of DWP-1 and DWP-2 accelerometers nearly halves with increasing clock frequency which shows the dominance of the mass residual motion noise since it is inversely proportional to the square of the sampling frequency.

4.2.3 Decimation Order Effect on the Output Noise

There are different noise sources of accelerometer system and mass residual motion noise is the most dominant noise source as described in Section 4.2.2. After mass residual motion noise, quantization noise comes as the second most effective noise source of the accelerometer systems studied in this thesis. As described in Section 2.2.1.1, quantization noise is shifted to high frequencies with sigma-delta readout

circuit and low-pass filtered with the decimation filter. As the cut-off frequency of this filter decreases, the effect of quantization noise at the output minimizes.

As the second dominant noise source of the accelerometer system, the quantization noise can be observed and calculated with changing decimation order because the decimation order value specifies the cut-off frequency of the decimation filter. As the decimation order increases, the cut-off frequency decreases and quantization noise effect at the output decreases.

This section presents the change in the output noise of the DWP-1 and DWP-2 accelerometers with changing decimation order. For the 16, 32, 40, 50, and 64 values of the decimation order of the Sinc^3 filter while the decimation order of the Sinc^2 filter is kept at 16; 12-position acceleration tests of the DWP-1 and DWP-2 accelerometers are done at each decimation order value. Then these test results are analyzed in terms of output noise and the scale factor value for each decimation order.

The effect of decimation order at the output noise is also investigated by performing simulations with different decimation orders. The 12-position acceleration simulations of the fabricated DWP-1 and DWP-2 accelerometer systems are done and output noise and scale factor values are observed at each decimation order value.

Decimation order effect on the output noise of DWP-1 accelerometer is analyzed both with simulations and test results for 500 kHz clock frequency. Table 9 shows the noise values and scale factor values obtained at each decimation order for DWP-1 accelerometer. As it can be seen from the table, scale factor values and noise values obtained from simulations and test results are very close and decreases with increase in decimation order.

Table 9: Effect of decimation order on DWP-1 accelerometer output noise and comparison of scale factor values of simulation and test results.

Decimation Order	Simulation Results		Test Results	
	16X16	Noise	84.9 $\mu\text{g}/\sqrt{\text{Hz}}$	Noise
Scale Factor		$1.2556 \cdot 10^{-5}$	Scale Factor	$1.2619 \cdot 10^{-5}$
32X16	Noise	56 $\mu\text{g}/\sqrt{\text{Hz}}$	Noise	72 $\mu\text{g}/\sqrt{\text{Hz}}$
	Scale Factor	$1.5821 \cdot 10^{-6}$	Scale Factor	$1.8748 \cdot 10^{-6}$
40X16	Noise	49.2 $\mu\text{g}/\sqrt{\text{Hz}}$	Noise	53.7 $\mu\text{g}/\sqrt{\text{Hz}}$
	Scale Factor	$0.97 \cdot 10^{-6}$	Scale Factor	$1.17 \cdot 10^{-6}$
50X16	Noise	42.1 $\mu\text{g}/\sqrt{\text{Hz}}$	Noise	50 $\mu\text{g}/\sqrt{\text{Hz}}$
	Scale Factor	$4.1852 \cdot 10^{-7}$	Scale Factor	$5.2252 \cdot 10^{-7}$
64X14	Noise	39.6 $\mu\text{g}/\sqrt{\text{Hz}}$	Noise	49.5 $\mu\text{g}/\sqrt{\text{Hz}}$
	Scale Factor	$2.0101 \cdot 10^{-7}$	Scale Factor	$2.5592 \cdot 10^{-7}$

Besides the scale factor and noise consistency between simulation and test results, these simulation and test results give us information about the quantization noise of the DWP-1 accelerometer. After 50X16 (800) decimation order value, the effect of quantization noise can be assumed negligible because output noise settles to a value even though there is a further increase in decimation order. Figure 47 shows the output noise change of DWP-1 accelerometer with increasing decimation order. In 12-position acceleration tests and simulations given in section 4.2.1 decimation order of 40X16 (640) was used which corresponds to 53.7 $\mu\text{g}/\sqrt{\text{Hz}}$ noise and 49.2 $\mu\text{g}/\sqrt{\text{Hz}}$ from test and simulation respectively. This noise includes quantization noise, the value of quantization noise inside this total accelerometer noise can be calculated by using the change of output noise occurred from 40X16 (640) decimation order to 50X16 (800) decimation order because the output noise for decimation order greater than 800, quantization noise effect is negligibly small and the effect of other noise sources is seen at the output. The quantization noise of DWP-1 accelerometer is calculated using Equation (28) and found as 24.7 $\mu\text{g}/\sqrt{\text{Hz}}$ and 25.62 $\mu\text{g}/\sqrt{\text{Hz}}$ from the test and simulation results respectively.

$$E^2_{total,rms} = E^2_{rms,quantization_noise} + E^2_{rms,other_noises} \quad (28)$$

where, $E_{total,rms}$ is the rms value of the total noise corresponding to the noise value obtained at decimation order of 640, $E_{rms,quantization_noise}$ is the rms value of the quantization noise, and $E_{rms,other_noises}$ is the rms value of the other noises corresponding to the noise value obtained at decimation order of 800.

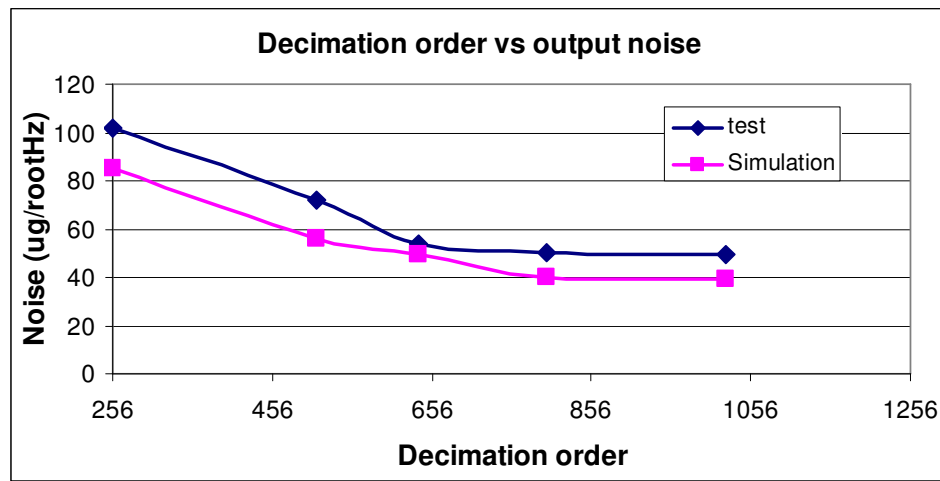


Figure 47: DWP-1 accelerometer noise change with increasing decimation order.

Decimation order effect on the output noise of DWP-2 accelerometer is also analyzed for 500 kHz and 1MHz clock frequencies to see both the effect of decimation order and clock frequency at the total noise. The simulations, tests, noise calculations and scale factor values are found using the same method described for DWP-1 accelerometer. Table 10 and Table 11 shows the noise values and scale factor values obtained at each decimation order for DWP-2 accelerometer

at 500kHz and 1MHz clock frequencies respectively. The simulations and tests are close in terms of noise and scale factor.

Table 10: DWP-2 accelerometer output noise and scale factor values of simulation and test results at 500kHz clock frequency.

Decimation Order	Simulation Results		Test Results	
	16X16	Noise	539.7 $\mu\text{g}/\sqrt{\text{Hz}}$	Noise
Scale Factor		2.97×10^{-5}	Scale Factor	3.609×10^{-5}
32X16	Noise	357.8 $\mu\text{g}/\sqrt{\text{Hz}}$	Noise	381.7 $\mu\text{g}/\sqrt{\text{Hz}}$
	Scale Factor	4.875×10^{-6}	Scale Factor	5.346×10^{-6}
40X16	Noise	320.05 $\mu\text{g}/\sqrt{\text{Hz}}$	Noise	373.3 $\mu\text{g}/\sqrt{\text{Hz}}$
	Scale Factor	2.627×10^{-6}	Scale Factor	2.933×10^{-6}
50X16	Noise	310.06 $\mu\text{g}/\sqrt{\text{Hz}}$	Noise	357.7 $\mu\text{g}/\sqrt{\text{Hz}}$
	Scale Factor	7.12×10^{-7}	Scale Factor	7.79×10^{-7}
64X14	Noise	303.66 $\mu\text{g}/\sqrt{\text{Hz}}$	Noise	341.5 $\mu\text{g}/\sqrt{\text{Hz}}$
	Scale Factor	6.789×10^{-7}	Scale Factor	7.307×10^{-7}

Table 11: DWP-2 accelerometer output noise and scale factor values of simulation and test results at 1MHz clock frequency.

Decimation Order	Simulation Results		Test Results	
	16X16	Noise	310.07 $\mu\text{g}/\sqrt{\text{Hz}}$	Noise
Scale Factor		8.972×10^{-6}	Scale Factor	9.651×10^{-6}
32X16	Noise	168.66 $\mu\text{g}/\sqrt{\text{Hz}}$	Noise	269.8 $\mu\text{g}/\sqrt{\text{Hz}}$
	Scale Factor	1.371×10^{-6}	Scale Factor	1.458×10^{-6}
40X16	Noise	105.6 $\mu\text{g}/\sqrt{\text{Hz}}$	Noise	150.87 $\mu\text{g}/\sqrt{\text{Hz}}$
	Scale Factor	6.953×10^{-7}	Scale Factor	7.481×10^{-7}
50X16	Noise	63.2 $\mu\text{g}/\sqrt{\text{Hz}}$	Noise	84.32 $\mu\text{g}/\sqrt{\text{Hz}}$
	Scale Factor	3.524×10^{-7}	Scale Factor	3.912×10^{-7}
64X14	Noise	57.2 $\mu\text{g}/\sqrt{\text{Hz}}$	Noise	76.34 $\mu\text{g}/\sqrt{\text{Hz}}$
	Scale Factor	1.792×10^{-7}	Scale Factor	1.9×10^{-7}

Figure 48 shows the output noise change of DWP-2 accelerometer with increasing decimation order at 500kHz and 1MHz clock frequency. The decrease in the output noise with increasing decimation order can be seen from Figure 48. The quantization noise of DWP-2 accelerometer is calculated using Equation (28) and found as $150.73 \mu\text{g}/\sqrt{\text{Hz}}$ and $102.91 \mu\text{g}/\sqrt{\text{Hz}}$ from the test and simulation results respectively for 500kHz clock frequency.

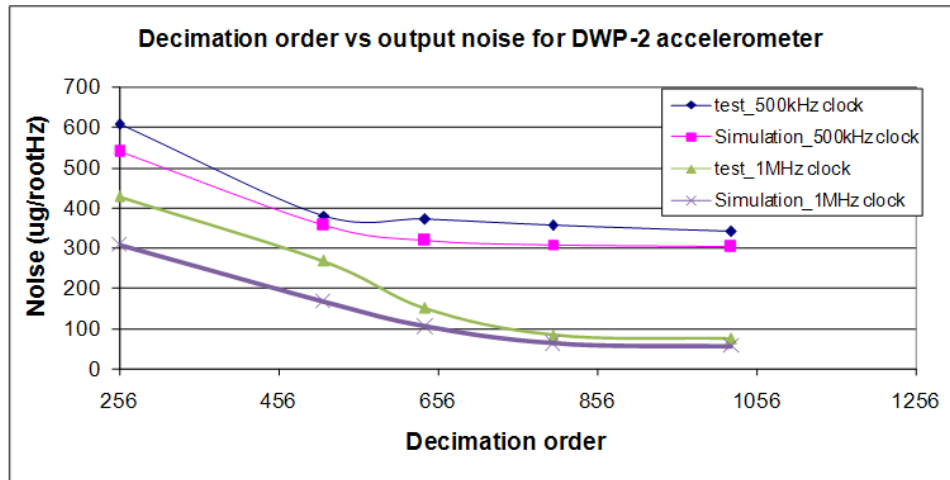


Figure 48: DWP-2 accelerometer noise change with increasing decimation order.

Here, it can be said that the accelerometer output noise can be lowered by increasing decimation order; however increase in decimation order will decrease the bandwidth of the accelerometer. There is a tradeoff between quantization noise and accelerometer bandwidth.

4.2.4 Integration Capacitance Effect on the Output Noise

The integration capacitance of the charge integrator of the readout circuit can be changed between 0pF-15pF by connecting related pads to either HIGH or LOW.

The integration capacitance change affects the amplifier noise, kT/C noise, and noises coming from the supply noise. As the integration capacitance increases, the amplifier, kT/C noise, and noises coming from the supply decrease. In this section, the effect of integration capacitance change at the output noise is presented in order to see the effect of amplifier and kT/c noise to the accelerometer total noise.

The 12-position acceleration test and simulation results and total noise obtained are given in section 4.2.1. In sections 4.2.2 and 4.2.3, the mass residual motion noise and quantization noise values in this total noise are calculated. The last portion of the total noise is the electrical noises coming from readout electronics which are amplifier and kT/C noise. This portion can be evaluated by observing the output noise change with changing integration capacitance value because these noises are inversely proportional to the integration capacitance value.

The 12-position acceleration tests and simulations are done with the DWP-1 accelerometer parameters given in Table 5. The accelerometer system output noise is obtained as 11 mg and 10 mg peak-to-peak from test and simulation results respectively at 800 Hz data rate. Using the same parameters given in Table 5 except changing the integration capacitance value from 2pF to 10 pF value, the 12-position acceleration test and simulations are repeated. With 10 pF integration capacitance, the accelerometer output noise is found 11 mg and 10 mg peak-to-peak from test and simulation respectively which are equal to the values obtained with 2 pF integration capacitance value. Therefore, the change in the integration capacitance value does not affect the output noise which means the amplifier noise, kT/C noise, and supply noise have negligible effect at the output total noise which cannot be observed.

4.2.5 Operational Range

The accelerometer model constructed in MATLAB-SIMULINK environment also gives operational range of the designed accelerometer as its output. In order to see the exact operational range of the fabricated accelerometer systems centrifuge tests of the accelerometers are performed and the results are compared with the simulation results. The test set-up constructed to do the centrifuge tests is given in Figure 49. With the rotation of the centrifuge arm (rotating arm), the accelerometer system is subjected to a centripetal acceleration with magnitude which can be calculated using Equation (29). Centrifuge tests of DWP-1 and DWP-2 accelerometers are performed and compared with the simulations.

$$a_{centripetal} = w^2 R \quad (29)$$

where, w is the angular speed of the rotating arm and R is the length between the center of the rotating arm and accelerometer.

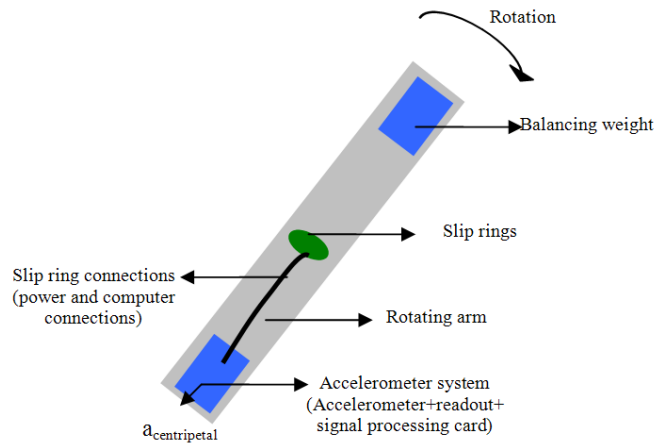


Figure 49: Centrifuge test set-up.

First, centrifuge test and simulation of DWP-1 accelerometer is performed. The centrifuge rotating arm is rotated such that the centripetal acceleration is increased from 0 m/s^2 (corresponds to 0g) to 147.15 m/s^2 (corresponds to 15g) with 2 m/s^2 acceleration ramp and the output of the accelerometer system is collected. This output is then calibrated with the scale factor found from 12-position acceleration tests and its graph is plotted as shown in Figure 50. As it can be seen from Figure 50, the accelerometer can sense up to 12.5 g acceleration which means the operational range of the DWP-1 accelerometer is found experimentally as $\pm 12.5\text{g}$.

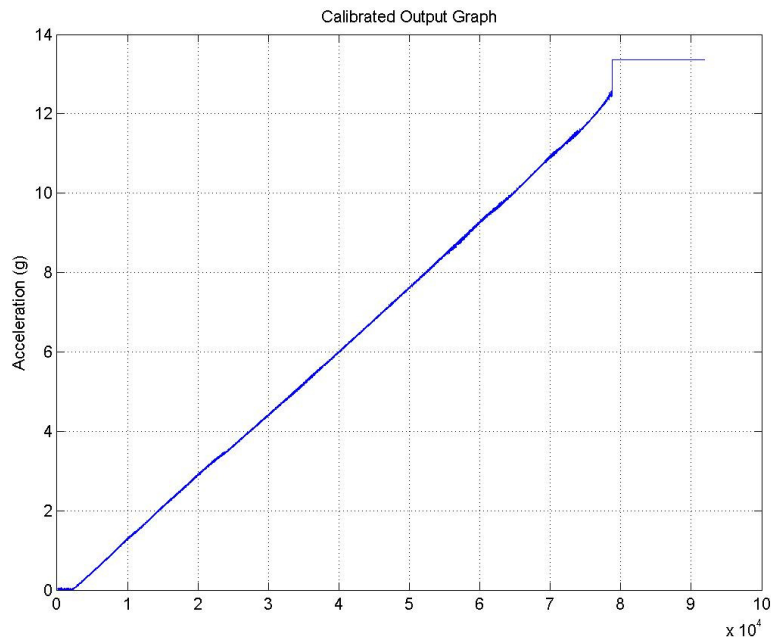


Figure 50: Centrifuge test result of DWP-1 accelerometer.

DWP-1 accelerometer SIMULINK model simulations are done to find the operational range of the fabricated accelerometer system theoretically. In order to find the operational range, step input accelerations are applied to the system

Simulink model. The magnitude of the applied step input accelerations start from '0g' to '20g' with '1g' steps and accelerometer model output is saved at each simulation. Figure 51 shows the calibrated accelerometer output versus applied acceleration graph obtained from these simulations. From the simulations, the operational range of the DWP-1 accelerometer is obtained as $\pm 19g$ as shown in Figure 51. Therefore, DWP-1 accelerometer operational range is obtained $\pm 12.5g$ and $\pm 19g$ from test and simulation results respectively. Here, simulation and test results are inconsistent. The reason of this inconsistency is the problems in the fabrication process which results in buckling of DWP-1 accelerometer and so fingers touching to each other. Since the model does not include accelerometer fabrication problems, there is an inconsistency between simulation and test results.

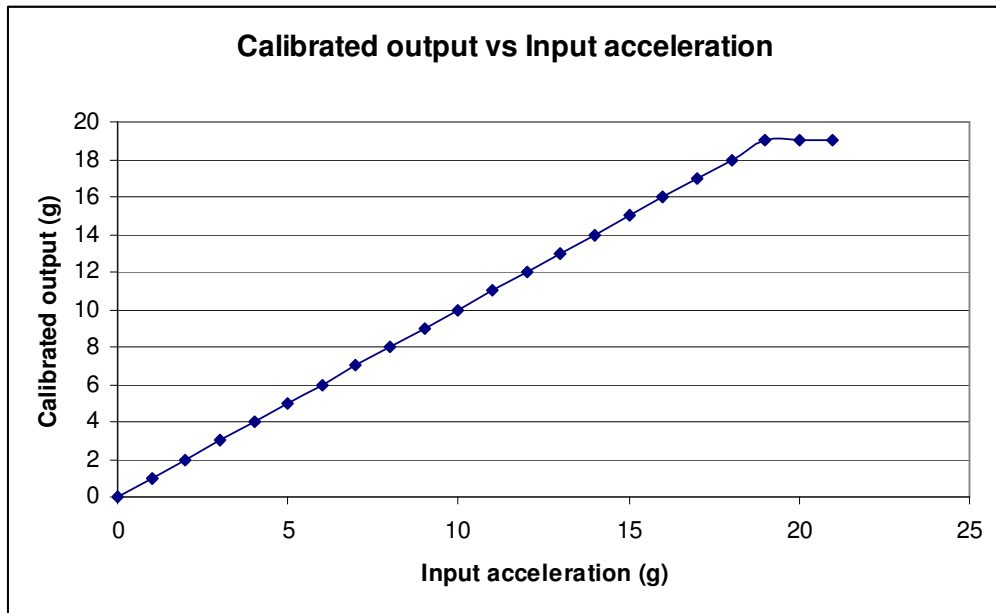


Figure 51: Operational range simulation of DWP-1 accelerometer.

DWP-2 accelerometer centrifuge test is also performed with the same set-up. The centrifuge rotating arm is rotated such that the centripetal acceleration is increased from 0 m/s^2 (corresponds to 0g) to 294.3 m/s^2 (corresponds to 30g) with 2 m/s^2 acceleration ramp and the output of the DWP-2 accelerometer is collected. Figure 52 shows the calibrated output of DWP-2 accelerometer. The calibrated output shows us that the DWP-2 accelerometer operational range is $\pm 31\text{g}$ experimentally. Operational range simulations of DWP-2 accelerometer is also performed and the operational range found is compared with the one found from the centrifuge test. Figure 53 shows the result of the operational range simulations of DWP-2 accelerometer and the operational range is found to be $\pm 34\text{g}$ theoretically. Hence, the operational range of DWP-2 accelerometer is found to be $\pm 31\text{g}$ and $\pm 34\text{g}$ from test and simulations respectively. Therefore the simulation and test results are consistent for DWP-2 accelerometer in terms of operational range.

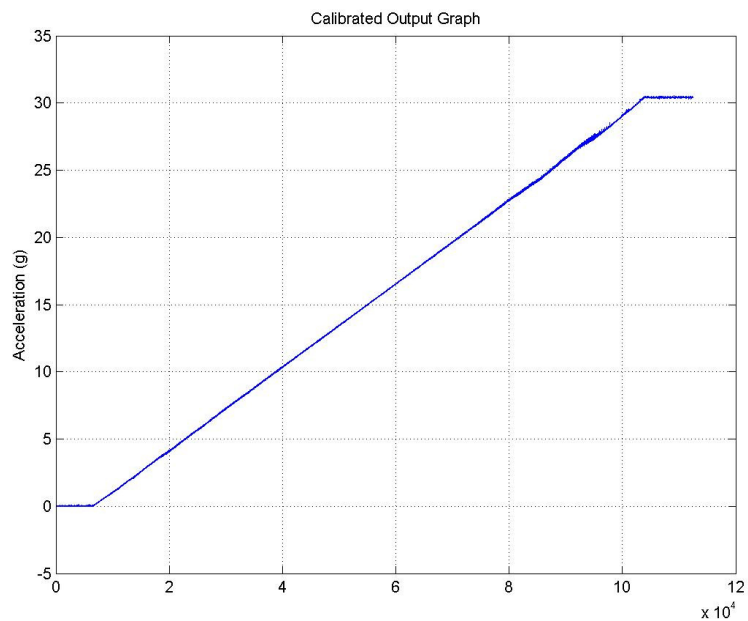


Figure 52: Centrifuge test result of DWP-2 accelerometer.

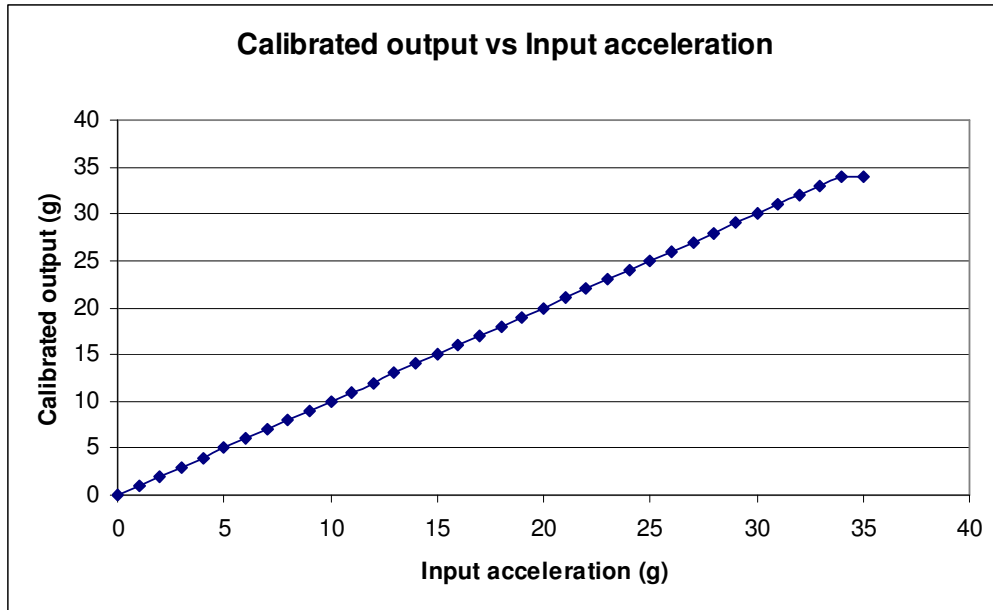


Figure 53: Operational range simulation of DWP-2 accelerometer.

To conclude, the DWP-1 and DWP-2 accelerometers operational range simulations and tests are performed. For DWP-1 accelerometer, simulations and test results are inconsistent due to some fabrication problems; whereas for DWP-2 accelerometer, simulations and test results are consistent in terms of operational range.

4.2.6 Conclusion

DWP-1 and DWP-2 accelerometers' simulations and tests are performed, analyzed and compared in terms of overall system performance in this study. Table 12 and Table 13 summarize the overall performance obtained from simulations and tests of DWP-1 and DWP-2 accelerometers respectively.

Table 12: Comparison of simulation and test results of DWP-1 accelerometer.

Compared Parameter	Simulation	Test
Mass Residual Motion Noise	46.4 $\mu\text{g}/\sqrt{\text{Hz}}$	50.1 $\mu\text{g}/\sqrt{\text{Hz}}$
Quantization Noise	25.62 $\mu\text{g}/\sqrt{\text{Hz}}$	24.7 $\mu\text{g}/\sqrt{\text{Hz}}$
Other Noises	5.6 $\mu\text{g}/\sqrt{\text{Hz}}$	1.8 $\mu\text{g}/\sqrt{\text{Hz}}$
Total Noise	53.3 $\mu\text{g}/\sqrt{\text{Hz}}$	58.7 $\mu\text{g}/\sqrt{\text{Hz}}$
Scale Factor	$0.97 \cdot 10^{-6}$ g/ output units	$1.17 \cdot 10^{-6}$ g/ output units
Open Loop Sensitivity	0.35 V/g	0.48 V/g
Operational Range	$\pm 19\text{g}$	$\pm 12.5\text{g}$

Table 13: Comparison of simulation and test results of DWP-2 accelerometer.

Compared Parameter	Simulation	Test
Mass Residual Motion Noise	302.28 $\mu\text{g}/\sqrt{\text{Hz}}$	338.02 $\mu\text{g}/\sqrt{\text{Hz}}$
Quantization Noise	102.91 $\mu\text{g}/\sqrt{\text{Hz}}$	150.73 $\mu\text{g}/\sqrt{\text{Hz}}$
Other Noises	26.17 $\mu\text{g}/\sqrt{\text{Hz}}$	48.8 $\mu\text{g}/\sqrt{\text{Hz}}$
Total Noise	320.05 $\mu\text{g}/\sqrt{\text{Hz}}$	373.3 $\mu\text{g}/\sqrt{\text{Hz}}$
Scale Factor	$2.627 \cdot 10^{-6}$ g/ output units	$2.933 \cdot 10^{-6}$ g/output units
Open Loop Sensitivity	0.375 V/g	0.45 V/g
Operational Range	$\pm 34\text{g}$	$\pm 31\text{g}$

For DWP-1 accelerometer; mass residual motion noise, quantization noise, total noise, and scale factor values obtained from tests are in close agreement with simulation results. However, there is a significant inconsistency between the simulation and test result for DWP-1 accelerometer operational range due to some fabrication problems which causes buckling and pull-in of the accelerometer. For DWP-2 accelerometer mass residual motion noise, quantization noise, total noise, operational range, and scale factor values obtained from tests are consistent with simulation results. Although the simulation and test results are close to each other for both DWP-1 and DWP-2 accelerometers, they are not exactly equal due to some fabrication problems, environmental effects, and effects coming from the test set-up which cannot be modeled.

This chapter presented the simulations performed with the accelerometer model proposed in MATLAB-SIMULINK and their comparison with the real test results of the modeled accelerometers. The comparisons show that the simulation and test results are close to each other, so the model can be used to estimate the performance of an accelerometer before designing it. Next chapter will give the accelerometer design algorithm generated using the theory behind this model for three different accelerometer structures.

CHAPTER 5

ACCELEROMETER SENSING ELEMENT DESIGN ALGORITHM

This chapter presents an accelerometer design algorithm based on the proposed model in MATLAB-SIMULINK. This design algorithm is generated to find the dimensions of the accelerometer satisfying the required performance parameters. The first section of this chapter gives an overview of the accelerometer design algorithm which is adapted to three different accelerometer structures. Then the following sections present algorithms and design constraints of each of these accelerometer structures.

5.1 Overview of the Accelerometer Design Algorithm

Within the thesis study, an accelerometer design algorithm is implemented in MATLAB which uses the theory of the model described in CHAPTER 3. The design algorithm gets some specifications as input that the design should satisfy and outputs the dimensions of the designed accelerometer. In this algorithm, the structure of the readout electronics and decimation filter are taken as described in Sections 3.2 and 3.3 for every design; the aim is to obtain the best accelerometer design which satisfies the input specifications. In order to obtain the best accelerometer design, algorithm plays with the accelerometer dimensions within the specified dimension limitations.

The design parameters are accelerometer finger length, finger width, antigap distance between fingers, spring length, spring width, proof mass density factor, and clock frequency which are swept in between minimum and maximum values in a

‘for’ loop to obtain the desired accelerometer design. In most of the cases, the algorithm finds more than one accelerometer designs which satisfy the defined specifications. In such cases, the algorithm gives the accelerometer which introduces minimum noise out of all designs as the solution.

The specifications that the designed accelerometer should meet are defined by the user. The accelerometer range and noise value are the most important specifications entered by the user. The die size that the accelerometer should fit is also entered as a specification. Then the algorithm takes these specifications and tries to design accelerometer according to these specifications and outputs the all the obtained parameters and dimensions of the designed accelerometer. The constraints used by the design algorithm are described below in detail.

- **Range Constraint:** The closed loop range of the designed accelerometer is calculated at each iteration of the ‘for’ loop with the formula given in Equation (30) [53] and compared with the required range. If the designed accelerometer’s range is greater than or equal to the required range then it means that the accelerometer satisfies the range constraint.

$$Range = \frac{1}{2} \frac{V^2}{m} \frac{T_f}{T} \frac{\partial c}{\partial x} = \frac{1}{2} \frac{V^2}{m} \frac{T_f}{T} \epsilon L_{finoverlap} h \left(\frac{N}{d_1^2} - \frac{N-1}{d_2^2} \right) \quad (30)$$

where, V is supply voltage, m is the mass, T_f/T is the fraction of the period that the feedback is applied, $L_{finoverlap}$ is the fingers overlapping length, h is the structural thickness, N is the number of fingers per side, and d_1 and d_2 are the gap and antigap spacings between fingers.

- **Noise Constraint:** The total noise of the designed accelerometer obtained from all noise sources described in Section 2.4 should be smaller than or

equal to the required noise value. At each iteration of the ‘for’ loop total noise is compared with the required noise value entered by the user and if the noise value is smaller than or equal to the required value then the designed accelerometer satisfies the noise constraint.

- **Die Width Control Constraint:** While the algorithm sweeps the design parameters, it should control whether the designed accelerometer width fits the specified die width or not. If the accelerometer width is smaller than or equal to the specified die width, then the die width control constraint is satisfied.
- **Die Length Control Constraint:** Like the die width control constraint; while the algorithm sweeps the design parameters, it should control whether the designed accelerometer length fits the specified die length or not. If the accelerometer length is smaller than or equal to the specified die length, then the die length control constraint is satisfied.
- **Pull-in Voltage Constraint:** Accelerometer pull-in voltage means fingers touching to each other at a voltage level applied between fingers and proof mass. At pull-in voltage value, the electrostatic force between fingers and proof mass causes fingers touching each other. As a rule of thumb, when the accelerometer proof mass displacement is greater than $1/3$ of the spacing between fingers, then pull-in can occur. This constraint is used to control the pull-in voltage when displacement of the proof mass is $1/3$ of the spacing between fingers. The algorithm controls whether the pull-in voltage value is greater than 5V (accelerometer supply voltage). If pull-in voltage value is greater than the specified pull-in voltage, pull-in voltage constraint is satisfied. Pull-in voltage value is found using Equation (31).

$$V_{pull-in} = \sqrt{\frac{2\left(k \frac{d_1}{3}\right)}{\left.\frac{\partial c}{\partial x}\right|_{x=\frac{d_1}{3}}} } \quad (31)$$

where k is spring constant and d_1 is the small gap between fingers.

The requirements of the accelerometer which will be designed by the algorithm are specified by the user and entered to a user interface shown in Figure 54. This interface allows the user to select the accelerometer structure that will be designed, to enter the required performance parameters, and to specify the dimensional limits.

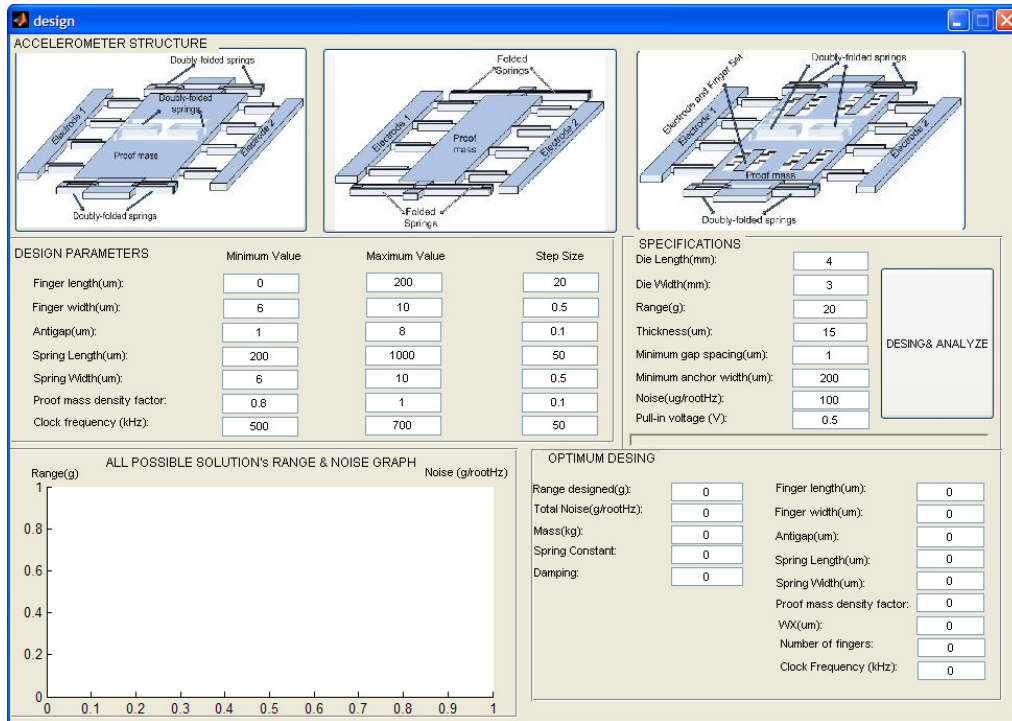


Figure 54: Accelerometer sensing element design algorithm user interface.

According to the described constraints, the algorithm is adapted to three different accelerometer structures which are the most generally fabricated accelerometer structure in METU-MEMS group. These structures are described in the following sections. One of these structures must be selected by the user before running the algorithm, so the algorithm will design accelerometer in that structure. In the following sections, these three accelerometer structures, their design parameters and how the algorithm is constructed for each structure are described.

5.2 1st Accelerometer Structure Design Algorithm

5.2.1 1st Accelerometer Structure

Design algorithm is proposed for three different accelerometer structures. The first accelerometer structure is described in this section. This accelerometer structure has two electrodes at both sides of the proof mass, fingers placed at the proof mass and electrodes and has 6 doubly folded springs which are placed at the center, the top and bottom of the proof mass. This 1st accelerometer structure is shown in Figure 55. In this structure 6 doubly folded beams are used, therefore the topological spring constant coefficient is 6. This structure has springs inside the proof mass to avoid the proof mass from buckling even for small structural thickness.

Here, the aim is to find the dimensions of the accelerometer with the given structure (finger length, finger width, antigap spacing between fingers, spring length, spring width and proof mass density factor) which fit the specified die dimensions and satisfies the required specifications. Generally the algorithm finds more than one design and among these results, the accelerometer which has the minimum noise value is given as the solution of the algorithm.

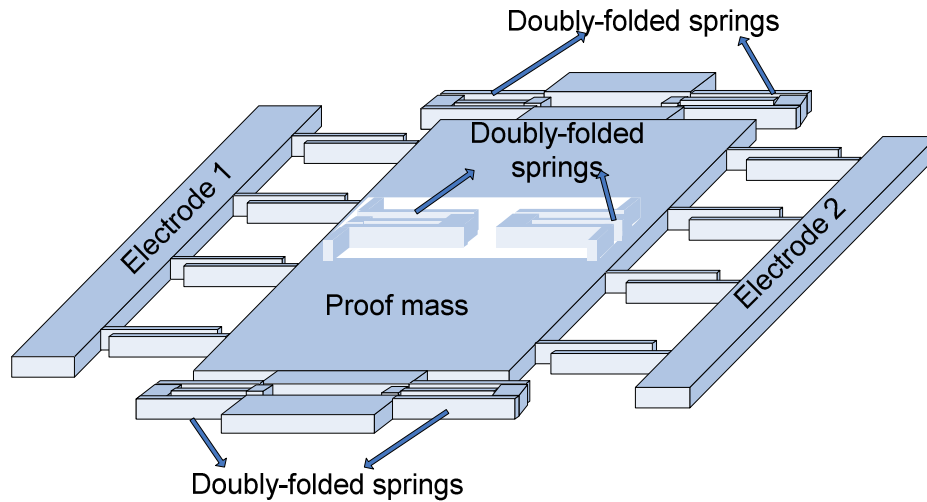


Figure 55: 1st accelerometer structure used in design algorithm.

5.2.2 Design Parameters and Constraints for the 1st Structure

The design parameters that the algorithm tries to find their values are finger length, finger width, antgap spacing between fingers, spring length, spring width and proof mass density factor. The maximum and minimum values can be entered from the user interface shown in Figure 54 by the user. The user also enters the required performance parameters of the accelerometer such as range, noise, die width, die length, pull-in voltage. There are also some process parameters that should be defined by the user which can be listed as thickness, minimum gap spacing, and minimum anchor width. The algorithm takes these values as input for its design and searches for a minimum noise accelerometer for this structure using the constraints given in Table 14. Here, die width and die length constraints are specific for this structure. In die width calculation; the spring length, finger length, minimum anchor width (electrode width), non-overlapping length of fingers (10 μm), and spacing necessary for the inner spring (250 μm) are taken into account. In die length

calculation; proof mass length, width of the two anchors of the accelerometer, and spacing necessary for fabrication issues (20 μm) are taken into account.

The algorithm sweeps the design parameters in between the defined minimum and maximum values with defined step size in a ‘for’ loop. At each iteration, the program controls the constraints given in Table 14. For the iterations which satisfy these constraints, the found dimensions and performance parameters are saved to an array and among these iterations, the accelerometer having minimum noise is given as the solution of the algorithm.

Table 14: Constraints used to design 1st accelerometer structure.

Constraints		
1	Range	$\frac{1}{2} \frac{\partial c}{\partial x} \frac{V^2 T_f}{m T} \geq \text{Specified_Range}$
2	Noise	$\text{Total Noise} \leq \text{Specified_Noise}$
3	Die width control	$\text{Spring length} + \text{finger length} + \text{minimum anchor width} + 260\mu\text{m} < \text{specified die width}/2$
4	Die length control	$\text{Proof mass length} + 2 * \text{minimum anchor width} + 20 \mu\text{m} = \text{Die length}$
5	Pull-in control	$V_{\text{pull-in}} = \sqrt{\frac{2 \left(k \frac{d_1}{3} \right)}{\left. \frac{\partial c}{\partial x} \right _{x=\frac{d_1}{3}}} } > \text{Specified_pull-in_voltage}$

5.3 2nd Accelerometer Structure Design Algorithm

5.3.1 2nd Accelerometer Structure

The second accelerometer structure used in design algorithm is described in this section. This accelerometer structure has two electrodes at both sides of the proof mass, fingers placed at the proof mass and electrodes, and has 4 folded springs which are placed at the four corners of the accelerometer. The 2nd accelerometer structure is shown in Figure 56.

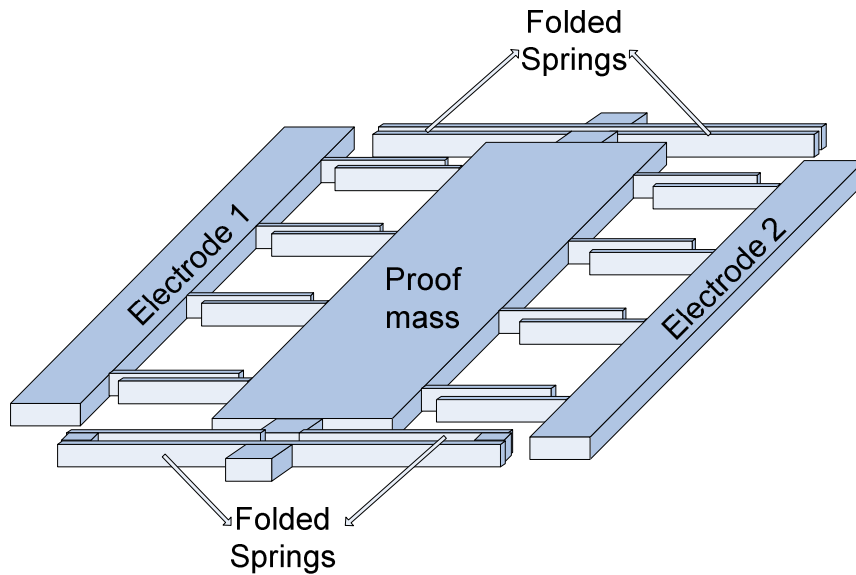


Figure 56: 2nd accelerometer structure used in design algorithm.

Here, as it can be seen from, 4 folded beam springs are used and hence the topological spring constant coefficient is 2 for this structure. Like the first

structure, design of this structure is done considering some constraints described below.

5.3.2 Design Parameters and Constraints for the 2nd Structure

The design parameters that the algorithm tries to find their values are finger length, finger width, antigap spacing between fingers, spring length, spring width and proof mass density factor which are same with the first accelerometer structure. With the same approach, the algorithm takes maximum and minimum values of the design parameters, gets the required specifications of the accelerometer such as range, noise, die width, die length and the process parameters like thickness, minimum gap spacing and minimum anchor width. The algorithm takes these values as input for its design and searches for a minimum noise accelerometer for this structure using the constraints given in Table 15. Here, die width and die length constraints are specific for this structure. In die width calculation; the finger length, minimum anchor width (electrode width), and non-overlapping length of fingers (10 μ m) are taken into account. In die length calculation; proof mass length, width of the two anchors of the accelerometer, and spacing necessary for fabrication issues (32 μ m) are taken into account.

The algorithm sweeps the design parameters in between the defined minimum and maximum values with defined step size in a 'for' loop. At each iteration, the program controls the constraints given in Table 14. For the iterations which satisfy these constraints, the found dimensions and performance parameters are saved to an array and among these iterations, the accelerometer having minimum noise is given as the solution of the algorithm.

Table 15: Constraints used to design 2nd accelerometer structure.

Constraints		
1	Range	$\frac{1}{2} \frac{\partial c}{\partial x} \frac{V^2}{m} \frac{T_f}{T} \geq \text{Specified_Range}$
2	Noise	$\text{Total Noise} \leq \text{Specified_Noise}$
3	Die width control	$\text{Finger length} + \text{minimum anchor width} + 10\mu\text{m} < \text{specified die width}/2$
4	Die length control	$\text{Proof mass length} + 2 * \text{minimum anchor width} + 32\mu\text{m} = \text{Die length}$
5	Pull-in control	$V_{\text{pull-in}} = \sqrt{\frac{2 \left(k \frac{d_1}{3} \right)}{\frac{\partial c}{\partial x} \Big _{x=\frac{d_1}{3}}} > \text{Specified_pull-in_voltage}$

5.4 3rd Accelerometer Structure Design Algorithm

5.4.1 3rd Accelerometer Structure

The last accelerometer structure used in design algorithm is described in this section. This 3rd structure has a different finger placing from the other two structures. This accelerometer structure has fingers and electrodes at two sides of the proof mass and also inside the proof mass which decreases the proof mass. This structure having fingers all around the proof mass is used to be able to decrease the finger length while keeping the operational range same. Decreasing the finger length provides better accelerometers in terms of mechanical properties because for long fingers there may be mechanical deformations because of internal stress. To summarize, this structure has 6 doubly folded springs at the corners and center of the proof mass, fingers and electrodes at both sides and center of the proof mass as

shown in Figure 57. The topological spring constant coefficient is 6 for this structure because it has 6 doubly folded springs. Like the other structures, design of this structure is done considering some constraints described in the following section.

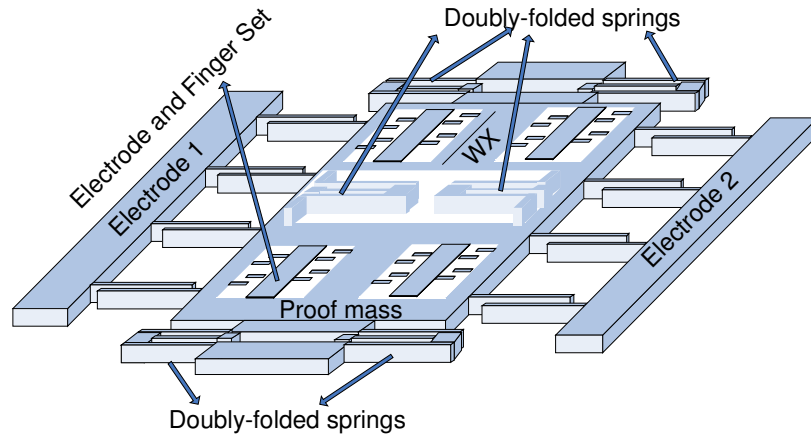


Figure 57: 3rd accelerometer structure used in design algorithm.

5.4.2 Design Parameters and Constraints for the 3rd Structure

This structure is rather complicated than the other two structures, so the design parameters that the algorithm tries to find their values are finger length, antgap spacing between fingers, width of the finger region inside the proof mass (WX) which is shown in Figure 57, spring width, and clock frequency. Finger width and proof mass density factor are kept constant and taken as $7\ \mu\text{m}$ and 1 respectively. With the same approach, the algorithm takes maximum and minimum values of the design parameters, gets the required specifications of the accelerometer such as range, noise, die width, and die length and the process parameters like thickness, minimum gap spacing, and minimum anchor width. The algorithm takes these

values as input for its design and searches for a minimum noise accelerometer for this structure using the constraints given in Table 16. Here, die width and die length constraints are specific for this structure. It is necessary to have two die width control constraints according to inner fingers and inner springs. For first die width control; finger lengths (side and inside of the proof mass), minimum anchor width (inner and outside electrodes), and non-overlapping length of fingers (30 μm) are taken into account. For the second die width control; spring length, finger length, minimum anchor width (electrode width), and fabrication necessary spacing are considered. In die length calculation; proof mass length, width of the two anchors of the accelerometer, and spacing necessary for fabrication issues (20 μm) are taken into account.

Table 16: Constraints used to design 2nd accelerometer structure.

Constraints		
1	Range	$\frac{1}{2} \frac{\partial c}{\partial x} \frac{V^2}{m} \frac{T_f}{T} \geq \text{Specified_Range}$
2	Noise	$\text{Total Noise} \leq \text{Specified_Noise}$
3	Die width control_1	$3 * \text{Finger length} + 3 * \text{minimum anchor width} + 30\mu\text{m} < \text{specified die width}/2$
4	Die width control_2	$\text{Spring length} + \text{finger length} + \text{minimum anchor width} + 260\mu\text{m} < \text{specified die width}/2$
5	Die length control	$\text{Proof mass length} + 2 * \text{minimum anchor width} + 20 \mu\text{m} = \text{Die length}$
6	Pull-in control	$V_{\text{pull-in}} = \sqrt{\frac{2 \left(k \frac{d_1}{3} \right)}{\left. \frac{\partial c}{\partial x} \right _{x=\frac{d_1}{3}}} } > \text{Specified_pull-in_voltage}$

The algorithm sweeps the design parameters in between the defined minimum and maximum values with defined step size in a ‘for’ loop. At each iteration, the program controls the constraints given in Table 16. For the iterations which satisfy these constraints, the found dimensions and performance parameters are plotted on the interface program and also saved to an array and among these iterations, the accelerometer having minimum noise is given as the solution of the algorithm.

This algorithm aims to find the dimensions of the accelerometer within the specified performance parameters. In order to verify the algorithm, an accelerometer is designed with this algorithm and it is tested to see whether it matches the performance found by the algorithm or not. The following section gives the designed accelerometer, along with its test results and performance comparison.

5.5 Accelerometer Design Algorithm Performance Matching

The accelerometer design algorithm is used to find the dimensions of the minimum noise accelerometer within specified performance parameters as described in previous sections. This part of the thesis will present a trial design for the 3rd accelerometer structure, the tests performed with the designed accelerometer and performance matching will be given.

The trial design is done for the 3rd accelerometer structure with range specification of ‘33g’ and noise specification of ‘125 μ g/ $\sqrt{\text{Hz}}$ ’. The other specifications and sweep parameter values are given in Figure 58. The algorithm is run and 6 different accelerometer designs are found whose range and noise values are given on ‘All Possible Solution’s Range & Noise Graph’ as shown in Figure 58. The accelerometer with minimum noise is given as the optimum design of the algorithm. Table 17 gives the dimensions and performance parameters of the optimum design. The operational range and noise tests of the optimum design accelerometer are done and results are compared with the ones found from the design algorithm.

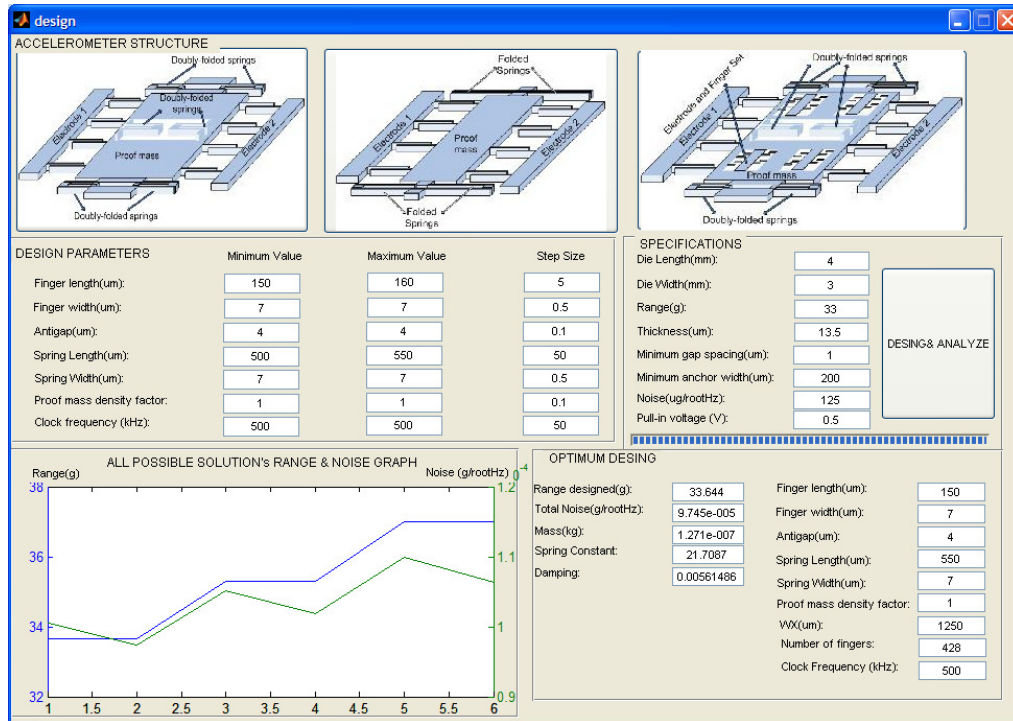


Figure 58: Accelerometer design algorithm trial design for 3rd structure.

Table 17: Designed accelerometer dimensions and performance parameters.

Accelerometer Dimensions	
Finger Length	150 μm
Finger Width	7 μm
Large distance between fingers	4 μm
Spring length	550 μm
Structural thickness	13.5 μm
WX (width of the finger region inside the proof mass)	1250 μm
Number of Fingers	428
Clock Frequency	500 kHz
Performance Parameters	
Operational Range	$\pm 33.64\text{g}$
Noise	97.4 $\mu\text{g}/\sqrt{\text{Hz}}$
Mass	$1.27 \times 10^{-7}\text{kg}$
Spring constant	21.7
Damping	0.0056

The designed accelerometer operational range test is performed on centrifuge rate table as described in Section 4.2.5. The operational range of the designed accelerometer is obtained $\pm 33.02g$ as shown in Figure 59. The experimentally found operational range matches the value found from the design algorithm which was $\pm 33.6g$.

The designed accelerometer resolution value is also found from tests and compared with the noise value derived from the algorithm. As it is mentioned in Section 1.1, resolution of an accelerometer can be found by plotting its Allan variance graph. Hence the accelerometer's output is saved for 1 hour duration and Allan variance graph is plotted with Alavar 5.2 software program using this collected data. The stability of the region having '-1/2' slope, i.e. random walk, is the resolution of the accelerometer which corresponds to the accelerometer noise [54]. For the designed accelerometer, the region having '-1/2' slope is selected as shown in Figure 60 and the stability of this region is found $155\mu g/\sqrt{Hz}$ with Alavar 5.2 program. The noise value estimated by the algorithm is $97.4\mu g/\sqrt{Hz}$ which is close to the noise value found from test ($155\mu g/\sqrt{Hz}$). The difference between test and estimated value by the algorithm comes from the environmental effects and test set-up noise that cannot be modelled.

To conclude, the accelerometer designed by the design algorithm approaches the requirements entered to the algorithm. The test results matches the values found by the algorithm in terms of operational range and resolution. Hence, this algorithm can be used as a tool to find the dimensions of the minimum noise accelerometer satisfying the requirements.

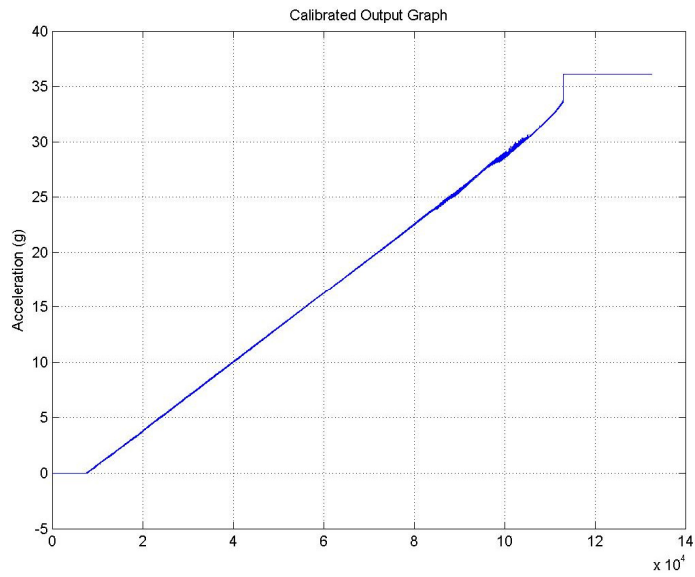


Figure 59: Operational range test of the designed accelerometer.

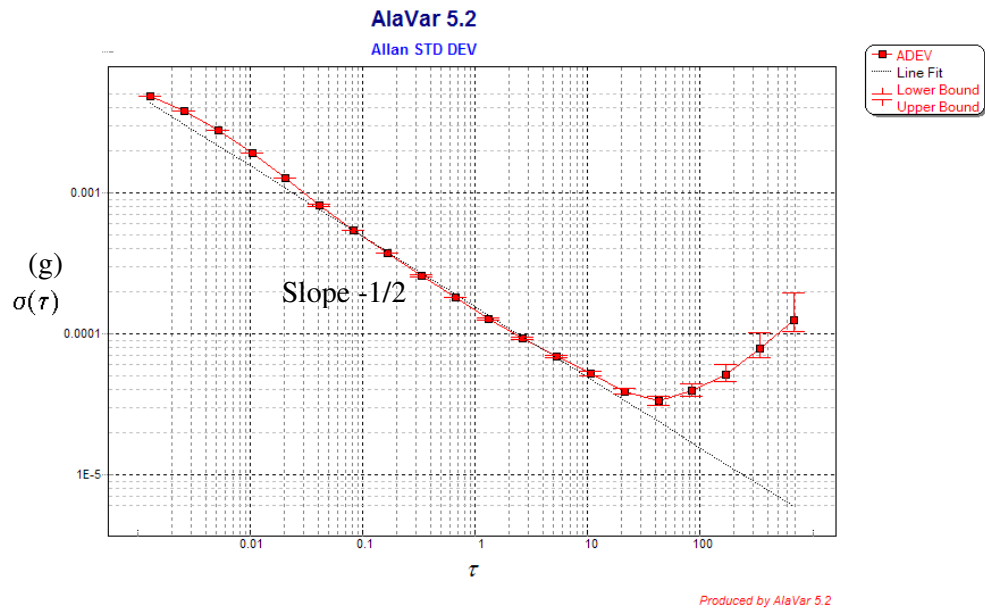


Figure 60: Designed accelerometer Allan variance plot and $-1/2$ slope region.

CHAPTER 6

CONCLUSION AND FUTURE WORK

This thesis presented a detailed MATLAB-SIMULINK model of a capacitive sigma-delta MEMS accelerometer and its verification through test results. The summary of the studies done within this thesis are given below:

- *MATLAB-SIMULINK model of a capacitive Σ - Δ accelerometer system.*

A detailed Matlab-Simulink model of a capacitive sigma-delta MEMS accelerometer system was proposed in this study. This model included MEMS accelerometer, closed-loop readout electronics, signal processing units, and noise sources and it was used to estimate the performance of an accelerometer system.

- *Implementation of two accelerometer systems*

Two accelerometer systems (DWP-1 and DWP-2) were implemented and tested within this thesis to verify the reliability of the model. METU-MEMS group has already been implementing capacitive MEMS accelerometers and CMOS readout circuits; in this study system level integration of the accelerometer and system level tests of the accelerometer were done.

- *Verification of the proposed model through test results*

The implemented accelerometer systems tests were performed and the simulations of the same accelerometer systems were done with the proposed model. The simulation and test results were compared in terms of noise

parameters and overall system performance. The total noise at the accelerometer output of DWP-1 accelerometer was obtained 53.3 $\mu\text{g}/\sqrt{\text{Hz}}$ and 58.7 $\mu\text{g}/\sqrt{\text{Hz}}$ from simulation and test results respectively. And the total noise at the accelerometer output of DWP-2 accelerometer was obtained 320.05 $\mu\text{g}/\sqrt{\text{Hz}}$ and 373.3 $\mu\text{g}/\sqrt{\text{Hz}}$ from simulation and test results respectively. It was observed from both simulations and tests that the most dominant noise sources of the accelerometer system are mass residual motion noise and quantization noise. In terms of overall system performance; open loop sensitivity, scale factor, and operational range values obtained from simulations and tests were compared for both accelerometer systems. For DWP-1 accelerometer; scale factor value of $0.97 \cdot 10^{-6}$ g/ output units and $1.17 \cdot 10^{-6}$ g/ output units, open loop sensitivity of 0.35 V/g and 0.48 V/g, and operational range of $\pm 19\text{g}$ and $\pm 12\text{g}$ were obtained from simulations and tests respectively. For DWP-2 accelerometer; scale factor value of $2.627 \cdot 10^{-6}$ g/ output units and $2.933 \cdot 10^{-6}$ g/ output units, open loop sensitivity of 0.375 V/g and 0.45 V/g, and operational range of $\pm 34\text{g}$ and $\pm 31\text{g}$ were obtained from simulations and tests respectively.

- *Accelerometer sensing element design algorithm written for three different accelerometer structures.*

After verification of the model, an accelerometer sensing element design algorithm was written using the theory behind the proposed model. This algorithm was written to find the dimensions of the sensing element satisfying the performance parameters specified by the user. Algorithm was adapted for three different accelerometer structures. A graphical user interface was generated for the user to enter the required performance parameters and select the required accelerometer structure.

- *An accelerometer sensing element is designed with the design algorithm to see the performance matching.*

An accelerometer sensing element was designed using the proposed design algorithm in order to see the reliability of the design algorithm. This accelerometer tests were performed and compared with the estimated performance parameters. The estimated operational range of the designed accelerometer was $\pm 33.6g$ where it was found $\pm 33.02g$ experimentally. The estimated noise of the designed accelerometer was $97.4 \mu g/\sqrt{Hz}$ where it was found $155 \mu g/\sqrt{Hz}$ experimentally.

6.1 Future Directions

An accurate accelerometer model is a need to estimate the system level performance of an accelerometer system before its implementation. The proposed MATLAB-SIMULINK model can be made more detailed to obtain a more realistic model. A further detailed model can be obtained by adding the effect of mechanical stress under applied acceleration growing out of the MEMS accelerometer. Also, the effect of temperature change of the accelerometer under test generated by the warm up of the readout electronics can be modeled and added to the system model. With these improvements, the system level estimates of the accelerometer model can be more realistic.

The capacitive accelerometer system MATLAB-SIMULINK model can be extended to different types of accelerometers such as piezoresistive, piezoelectric, thermal etc. This extension will make this model a more general tool for all types of accelerometers.

The sensing element design algorithm can be improved by adding new constraints to the algorithm such as mechanical properties of the materials used in the

fabrication process and limitations coming from these mechanical properties. Also the design algorithm can include the design of the readout electronics and decimation filter. However this improvement will make the algorithm more complicated, difficult to handle and increase the time processing time of the algorithm.

The design algorithm is written for three different accelerometer structures and it can be extended to more accelerometer structures, however this will introduce new constraints which will result in complexity of the algorithm. Here the basic idea is to choose the safe accelerometer structures according to fabrication process among various structures.

REFERENCES

1. N. Yazdi, F. Ayazi, and K. Najafi, "Micromachined Inertial Sensors," *Proceedings of the IEEE*, vol. 86, pp. 1640-1659, August 1998.
2. A. S. Salián, "Design, Fabrication and Test of High-Performance Capacitive Microaccelerometers," Ph.D. dissertation, University of Michigan, Ann Arbor, USA, 2001.
3. M. Kraft, "Micromachined Inertial Sensors: The State of the Art and a Look into Future," *IMC Measurement and Control*, vol. 33, pp. 164-168, 2000.
4. P. F. Man and C. H. Mastrangelo, "Surface Micromachined Shock Sensor for Impact Detection," *IEEE Solid-State Sensors and Actuator Workshop (Hilton Head'94)*, pp. 156-159, 1994.
5. J. Stauffer and P. Salomon, "Advanced MEMS Accelerometers," *OnBoard Technology*, pp. 48-51, September 2005.
6. IEEE Std. 1293-1998, *IEEE Standard Specification Format Guide and Test Procedure for Linear, Single-Axis, Nongyroscopic Accelerometers*, IEEE, 1998.
7. Freescale Semiconductor, Accelerometer Terminology Guide May, 2007. [Online]. Available: http://www.freescale.com/files/sensors/doc/support_info/SENSORTERMSPG.pdf. [Accessed: May 1, 2009]
8. A. Partidge, J. K. Reynolds, B. W. Chui, E. M. Chow, A. M. Fitzgerald, L. Zhang, and N.I. Maluf, "A High-Performance Planar Piezoresistive

Accelerometer,” *Journal of Microelectromechanical Systems*, vol. 9, pp. 58-66, March 2000.

9. Honeywell International Inc., 2008. [Online]. Available: http://content.honeywell.com/sensing/sensotec/accelerometer_faq.asp?category=All. [Accessed: May 3, 2009].
10. R. F. Yazıcıoğlu, “Surface Micromachined Capacitive Accelerometers Using MEMS Technology,” M.S. Thesis, Middle East Technical University, Ankara, TURKEY, 2003.
11. U. A. Dauderstadt, P. M. Sarro, and P. J. French, “Temperature Dependence and Drift of a Thermal Accelerometer,” *Sensors and Actuators*, vol. 66, pp. 244-249, 1998.
12. J. Kalanik and R. Pajak, “A Cantilever Optical-Fiber Accelerometer,” *Sensors and Actuators*, vol. 68, pp. 350-355, 1998.
13. B. Guldemann, P. Dubois, P. A. Clere, and D. Rooji, “Fiber Optic-MEMS Accelerometer with High Mass Displacement Resolution,” *11th Int. Conf. Solid-State Sensors and Actuators (Transducers’01)*, 2001, pp. 438-441.
14. D. Chen, Z. Wu, L. Lui, X. Shi, and J. Wang, “An Electromagnetically Excited Silicon Nitride Beam Resonant Accelerometer,” *IEEE Sensors Journal*, vol. 9, pp. 1330-1338, February 2009.
15. N. Barbour and G. Schmidt, “Inertial Sensor Technology Trends,” *IEEE Sensors Journal*, vol. 1, pp. 332-339, December 2001.

16. M. A. Erişmiş, "MEMS Accelerometers and Gyroscopes for Inertial Measurement Units," M. S. Thesis, Middle East Technical University, Ankara, TURKEY, 2004.
17. M. Kraft and C. P. Lewis, "System Level Simulation of a Digital Accelerometer," in *International Conference on Modelling and Simulation of Microsystems*, pp. 267-272, 1998.
18. Z. Yufeng, L. Xiaowei, and C. Weiping, "System-Level Modeling of Force-Balance MEMS Accelerometers," *Journal of Semiconductors*, vol. 29, pp. 917-922, May 2008.
19. D. P. Kumar and K. Pal, "System Level Simulation of Servo Accelerometer in Simulink," *Journal of Physical Sciences*, vol. 10, pp. 143-150, December 2006.
20. T. L. Grigorei, "The Matlab/Simulink Modeling and Numerical Simulation of an Analogue Capacitive Micro-Accelerometer. Part 2: closed loop," in *Perspective Technologies and Methods in MEMS Design, MEMSTECH 2008*, 2008, pp. 115-121.
21. N. Yazdi, H. Kulah, and K. Najafi, "Precision Readout Circuits for Capacitive Microaccelerometers," in *IEEE Sensors*, 2004, pp. 28-31.
22. J. Wu, G.K. Fedder, L.R. Carley, "A low-noise low-offset capacitive sensing amplifier for a 50- $\mu\text{g}/\sqrt{\text{Hz}}$ monolithic CMOS MEMS accelerometer," *IEEE Journal of Solid-State Circuits*, vol. 39, pp. 722-730, May 2004.

23. J. A. Geen, S. J. Sherman, J. F. Chang, S. R. Lewis, "Singlechip surface micromachined integrated gyroscope with 50°/h Allan deviation," *IEEE Journal of Solid-State Circuits*, vol. 37, pp.1860-1866, December 2002.
24. N. Yazdi, A. Mason, K. Najafi, and K.D. Wise," A generic interface chip for capacitive sensors in low-power multiparameter microsystems," *Sensors & Actuators Part A*, vol. 84, pp. 351-361, September 2000.
25. V. P. Petkov and B. E. Boser, "High-Order Electromechanical $\Sigma\Delta$ Modulation in Micromachined Inertial Sensors," *Circuits and Systems I: Regular Papers*, vol. 53, pp. 1016-1022, May 2006.
26. S. Park, "Motorola Digital Signal Processors, Principles of Sigma-Delta Modulation for Analog-to-Digital Converters," Motorola APR8/D Rev.1.
27. Intersil, Appl. Note 9504, pp. 1-7.
28. W. Henrion, L. DiSanza, and M. Ip, "Wide Dynamic Range Direct Digital Accelerometer," *IEEE Solid State Sensors and Actuators*, 1990, pp. 153-157.
29. S. R. Norsworthy, R. Schreier, and G. C. Temes, *Delta-Sigma Data Converters Theory, Design, and Simulation*. IEEE Press, 1996.
30. CRYSTAL, "Delta-Sigma Techniques," Appl. Note AN10, 1997, pp. 1-10.
31. C. Zhao, L. Wang, and T. J. Kazmierski, "An Efficient and Accurate MEMS Accelerometer Model With Sense Finger Dynamics for Applications in Mixed-Technology Control Loops," in *IEEE Behavioral Modeling and Simulation Conference*, 2007, pp. 143-147.

32. B. Boğa, I.E. Ocak, H. Kùlah, and T. Akin, "Modelling of a Capacitive Σ - Δ MEMS Accelerometer System Including the Noise Components and Verification With Test Results," in *IEEE MEMS Conference*, 2009, pp. 821-824.
33. B. V. Amini and F. Ayazi, "A 2.5-V 14-bit $\Sigma\Delta$ CMOS SOI Capacitive Accelerometer," *IEEE Journal of Solid-State Circuits*, vol. 39, pp. 2467-2475, December 2004.
34. B. V. Amini and F. Ayazi, "Micro-Gravity Capacitive Silicon-on-Insulator Accelerometers," *Journal of Micromechanics and Microengineering*, vol. 15, pp. 2113-2120, 2005.
35. R. Kepenek, "Capacitive CMOS Readout Circuits for High Performance MEMS Accelerometers," M. S. Thesis, Middle East Technical University, Ankara, TURKEY, 2008.
36. H. Kùlah, J. Chae, and K. Najafi, "Noise Analysis and Characterization of A Sigma-Delta Capacitive Silicon Microaccelerometer," in *International Conference on Solid State Sensors*, 2003, pp. 95-98.
37. Y. Zhou, "Layout Synthesis of Accelerometers," M. S. Thesis, Carnegie Mellon University, Pittsburg, USA, 1998.
38. H. Hosaka, K. Itao, and S. Kuroda, "Evaluation of Energy Dissipation Mechanisms in Vibrational Microactuators," in *IEEE Micro Electro Mechanical Systems*, 1994, pp. 193-198.

39. T. B. Gabrielson, "Mechanical-Thermal Noise in Micromachined Acoustic and Vibration Sensors," *IEEE Transactions on Electron Devices*, vol. 40, pp. 903-909, May 1993.
40. O. Oliaei, "Noise Analysis of Correlated Double Sampling SC Integrators With a Hold Capacitor," *IEEE Transactions on Circuits and Systems*, vol. 50, pp. 1198-1202, September 2003.
41. T. Kajita, U. Moon, and G. C. Themes, "A Noise-Shaping Accelerometer Interface Circuit for Two-Chip Implementation," *VLSI Design*, vol. 14, pp. 355-361, 2002.
42. H. Klah, "Closed-loop Electromechanical Sigma-Delta Microgravity Accelerometers," Ph. D. dissertation, University of Michigan, Ann Arbor, USA, 2003.
43. N. Yazdi and K. Najafi, "Performance Limits of a Closed-Loop Micro-G Silicon Accelerometer with Deposited Rigid Electrodes," in *International Conference on Microelectronics*, 2000, pp. 313-316.
44. N. Yazdi and K. Najafi, "An All-Silicon Single-Wafer Micro-g accelerometer With a Combined Surface and Bulk Micromachining Process," *Journal of Microelectromechanical Systems*, vol. 9, pp. 544-550, 2000.
45. J. B. Starr, "Squeeze-Film Damping in Solid-State Accelerometers," in *Solid-State Sensor and Actuator Workshop*, 1990, pp. 44-47.

46. R. Kepenek, İ. E. Ocak, H. Kùlah, and T. Akin, "A μg Resolution Microaccelerometer System with A Second-Order Σ - Δ Readout Circuitry," in *IEEE Prime*, 2008, pp. 41-44.
47. W. T. Ang, S. Y. Khoo, P. K. Khosla, and C. N. Riviere, "Physical Model of a MEMS Accelerometer for Low-g Motion Tracking Applications," in *International Conference on Robotics & Automation*, 2004, pp. 1345-1351.
48. IEEE Std. 337-1972, *IEEE Standard Specification Format Guide and Test Procedure for Linear, Single-Axis, Pendulous, Analog Torque Balance Accelerometer*, IEEE, 1971.
49. Texas Instruments, Appl. Note SLOA082, pp. (10-1)-(10-24).
50. Vaughan Wesson, "TN200410A-Dynamic Range," October 2004. [Online]. Available: http://www.seis.com.au/TechNotes/TN200410A_SNR.html. [Accessed: April 20, 2009].
51. J. Doscher, "Accelerometer Design and Applications," Analog Devices.
52. IEEE Std. 836-1991, *IEEE Recommended Practice for Precision Centrifuge Testing of Linear Accelerometers*, IEEE, 1991.
53. M. Lemkin and B. E. Boser, "A Three-Axis Micromachined Accelerometer with a CMOS Position-Sense Interface and Digital Offset-Trim Electronics," *IEEE Journal of Solid-State Circuits*, vol. 34, pp. 456-468, April 1999.
54. IEEE Std. 952-1997, *IEEE Standard Specification Format Guide and Test Procedure for Single-Axis Interferometric Fiber Optic Gyros*, IEEE, 1997.